DETECTING LAND-COVER CHANGE USING MODIS TIME-SERIES DATA

By

Waldo Kleynhans

Submitted in partial fulfillment of the requirements for the degree

Philosophiae Doctor (Electronic)

in the

Faculty of Engineering, Built Environment and Information Technology

Department of Electrical, Electronic and Computer Engineering

UNIVERSITY OF PRETORIA

August 2011

SUMMARY

DETECTING LAND-COVER CHANGE USING MODIS TIME-SERIES DATA

by

Waldo Kleynhans

Anthropogenic changes to forests, agriculture and hydrology are being driven by a need to provide water, food and shelter to more than six billion people. Unfortunately, these changes have a major impact on hydrology, biodiversity, climate, socio-economic stability and food security. The most pervasive form of land-cover change in South Africa is human settlement expansion. In many cases, new human settlements and settlement expansion are informal and occur in areas that are typically covered by natural vegetation. Settlements are infrequently mapped on an ad-hoc basis in South Africa which makes information on when and where new settlements form very difficult. Determining where and when new informal settlements occur is beneficial from not only an ecological but also a social development standpoint. The objective of this thesis is to make use of coarse resolution satellite data to infer the location of new settlement developments in an automated manner by making use of machine learning methods. The specific sensor that is considered in this thesis is the MODIS sensor on-board the Terra and Aqua satellites. By using samples taken at regular intervals (8 days), a hyper-temporal time-series is constructed and consequently used to detect new human settlement formations in South Africa. Two change detection methods are proposed in this thesis to achieve the goal of automated new settlement development detection using this high-temporal coarse resolution satellite time-series data.

OPSOMMING

BEPALING VAN LANDELIKE VERANDERING DEUR GEBRUIK TE MAAK VAN MODIS TYDREEKSDATA

deur

Waldo Kleynhans

Promotor:	Prof J.C. Olivier
Departement:	Elektriese, Elektroniese en Rekenaar Ingenieurswese
Universiteit:	Universiteit van Pretoria
Graad:	Philosophiae Doctor (Elektronies)
Sleutelwoorde:	autokorrelasie funksie, verandering deteksie, extended Kalman filter, menslike nedersettings, hiper-temporaal, landelike verandering, MODIS, tyds-reeks

Menslike verandering wat 'n invloed het op die natuurlike toestand van woude, landbou en hidrologie word gedryf deur die noodsaakliheid om water, kos en behuising aan meer as 6 biljoen mense te verskaf. Hierdie verandering het 'n geweldige impak op hidrologie, biodiversiteid, klimaat, sosio-ekonomiese stabiliteit en voedselsekuriteit. Die mees algemene landelike verandering in Suid-Afrika is die uitbreiding van menslike nedersettings. Nuwe menslike nedersettings en die uitbreiding hiervan is dikwels informeel en kom voor in areas wat tipies bedek is met natuurlike plantegroei. In Suid-Afrika is dit baie moeilik om informasie te bekom oor waar en waneer nuwe nedersettings voorkom aangesien hierdie informasie nie gereeld opgedateer word nie. Die bepaling van waar en waneer nuwe nedersettings voorkom is voordelig vanuit beide 'n ekologiese sowel as 'n sosiale-ontwikkelings standpunt. Die doel van hierdie proefskrif is om te bepaal waar nuwe nedersettings ontwikkel deur gebruik te maak van medium resolusie sateliet data. Hierdie inligiting kan op 'n outomatiese manier bekom word deur gebruik te maak van masjien-leer metodes. Die data wat gebruik word om die navorsing vir hierdie proefskrif uit te voer is verkry van die MODIS sensor op die Terra en Aqua sateliete. Deur gebruik te maak van observasies wat elke 8 dae beskikbaar is, is 'n hiper-temporale tydreeks saamgestel. Hierdie tydreeks is gebruik om te bepaal waar nuwe menslike nedersettings in Suid-Afrika gevorm het. Twee metodes word voorgestel in hierdie proefskrif om te bepaal waar nuwe nedersettings vorm.

ACKNOWLEDGEMENT

LIST OF ABBREVIATIONS

Autocorrelation Function	ACF
Atmospheric Infrared Sounder	AIRS
Advanced Microwave Scanning Radiometer-EOS	AMSR-E
Advanced Microwave Sounding Unit	AMSU-A
Advanced Space borne Thermal Emission and Reflection Radiometer	ASTER
Algorithm Theoretical Basis Document	ATBD
Bidirectional Reflection Distribution Function	BRDF
Change Vector Analysis	CVA
Clouds and the Earth's Radiant Energy System	CERES
Discrete Fourier Transform	DFT
Disturbance Index	DI
Extended Kalman Filter	EKF
Earth Resource Satellite	ERTS
European Remote Sensing	ERS
Enhanced Thematic Mapper Plus	ETM+
Enhanced Vegetation Index	EVI
Fast Fourier Transform	FFT
Fraction of Absorbed Photosynthetically Active Radiation	FAPAR
Geographical Information System	GIS
Global Earth Observation System of Systems	GEOSS
Group on Earth Observations	GEO
High-Resolution Visible	HRV
Humidity Sounder for Brazil	HSB
Indian Remote Sensing	IRS
Infrared	IR
Instantaneous Field of View	IFOV

Japanese Earth Resource Satellite	JERS
Low earth orbit	LEO
Multi-angle Imaging SpectroRadiometer	MISR
Measurements of Pollution in the Troposphere	MOPITT
National Land-Cover	NLC
Net Primary Productivity	NPP
Neural Network	NN
Normalized Difference Vegetation Index	NDVI
Photosynthetically Active Radiation	PAR
Point Spread Function	PSF
Principal Component Analysis	PCA
Probability Density Function	PDF
Radiative Transfer Model	RTM
Signal-to-noise Ratio	SNR
Satellite Pour l'Observation de la Terre	SPOT
Support Vector Machine	SVM
Synthetic Aperture Radar	SAR
Television and Infrared Observation Satellite	TIROS
Univariate Image Differencing	UID
United Nations	UN
Ultra Violet	UV
Vegetative Cover Conversion	VCC
Vegetation Index	VI

CONTENTS

Contents

Department of Electrical, Electronic and Computer Engineering   II

University of Pretoria

CHAPTER ONE

INTRODUCTION

1.1 PROBLEM STATEMENT

Anthropogenic changes to natural land cover are being driven by a need to provide water, food and shelter to more than six billion people [1]. Unfortunately, these changes have a major impact on hydrology, biodiversity, climate, socio-economic stability and food security [1,2]. Changes in land-use contribute to human impact on the climate as we are changing the natural rate of exchange of carbon dioxide between the atmosphere and the terrestrial biosphere, for example huge stocks of carbon are released as a result of deforestation [2,3].

The most pervasive form of land-cover change in South Africa is human settlement expansion [4]. In many cases, new human settlements and settlement expansion are informal and occur in areas that were previously covered by natural vegetation. Informal or unplanned settlements usually evolve as people move closer to employment opportunities [4]. These settlements can occur in various locations and are normally without basic services, which includes electricity, running-water, water-borne sewage and refuse removal. The spatial layout is often not planned but informally developed by the inhabitants of the settlements themselves [5]. Figure 1.1 shows an informal settlement in the Limpopo province of South Africa which developed between 2003 and 2009 in an area that was initially mostly covered by natural vegetation.

A report from the nineteenth special session of the general assembly of the United Nations (UN) identified sustainable human settlements as a matter requiring urgent attention and states that local government needs to be empowered to plan, implement, develop and manage human settlements [6]. It further states that local government needs to be enabled to manage existing informal settlements, and prevent the establishment of new ones. The occurrence of new small rural villages and scattered

FIGURE 1.1: QuickBird image of a new settlement development (courtesy of Google™Earth)

settlements is difficult to monitor by local government as the majority are informal and erected rapidly without the prior consent of the relevant government or municipal authorities. This leads to inadequate water, water-borne sewage and refuse removal provision [7]. Settlements are infrequently mapped on an ad-hoc basis in South Africa. It follows that determining where and when new informal settlements occur is beneficial not only from an environmental, but also from a socio-economic point of view.

1.2   OBJECTIVE OF THIS THESIS

As shown in the previous section, there exists a need to perform regular land cover change evaluations to identify change areas of interest. Change detection can be defined as the process of identifying differences in the state of an area by observing it at different times [8]. Human operator-dependent change mapping through visual interpretation of imagery is time consuming and resource intensive. Hence there is a need for automated change detection to reduce operator dependence and to enable large datasets to be processed frequently [9, 10].

Remote sensing is the science of obtaining information on an object or area without being in contact with the object or area under investigation [11]. Using various sensors, data are acquired remotely and analyzed to obtain information on the area that is measured by the sensor. Coarse resolution remotely sensed data provides an effective mechanism to monitor large areas on a frequent basis as the wide swath (2000 – 3000 km) of coarse resolution sensors (250 – 1000 m pixel size) enables the same area to be observed at a very high temporal sampling rate (near daily), thus resulting in a highly sampled (hyper-temporal) coarse spatial resolution time-series. This hyper-temporal time-series could

potentially be used as a first step as a change alarm leading to further investigation using higher resolution sensors such as Landsat 7, Ikonos, and QuickBird [12].

Automated land-cover change detection at regional or global scales, using hyper-temporal, coarse resolution satellite data has been a highly desired [13], but elusive goal of environmental remote sensing and has even been described by some as the "holy grail" of remote sensing [9].

Digital change detection encompasses the quantification of temporal phenomena from multi-date imagery that is usually acquired by satellite-based, multi-spectral sensors [14, 15]. Land-cover change can be categorized into two types. The first type is referred to as land-cover modification where subtle changes affect the character of the land-cover without changing its overall classification, such as drought and burned areas within natural vegetation [14]. Land-cover modification is often associated with natural climate variability. The second type of land-cover change is referred to as land-cover conversion where there is a complete replacement of one land-cover type by another such as the transformation of natural vegetation by agriculture.

Change detection methods have been extensively reviewed by Lu and Weng [15] as well as Coppin *et al.* [14]. The majority of the methods that were reviewed by the aforementioned authors are based on image differencing, post-classification comparison and change trajectories of multi-date high resolution data. In most cases, these methods only consider two images for change detection, effectively trying to detect areas of change from one image to the next. Coarse resolution satellite data provide frequent observations (daily or multi-day composites) of land surface conditions at regional to global scales and are thus an attractive option for regional-scale change detection. Many change detection methods based on high-frequency, coarse resolution satellite data do not rely on true time-series analysis. The data are mostly treated as hyper-dimensional or as derived metrics [16–19] but not as hyper-temporal, failing to exploit the valuable temporal components, for example, the phase or frequency modulation of the signal, which is driven by seasonal changes in land surface phenology [20]. In addition, many of these methods consider large-scale ecosystem disturbances, for example, wildfires, insect outbreaks and natural disasters [18, 19] as opposed to the relatively small spatial extent of a new settlement development which involves but a few contiguous MODIS pixels.

As stated in the previous section, the most pervasive form of land-cover change in South Africa is human settlement expansion. Consequently, developing a change detection framework for detecting the formation of new settlements using a remote sensing approach will be the point of departure towards

the greater objective of developing a global or regional automated land cover change detection method. It follows that the primary objective of this thesis is to develop and test an automated change detection framework that is able to detect the transformation of natural vegetation to human settlement which could then be adapted to consider many other types of land cover change. Two novel change detection methods were formulated to solve the aforementioned problem. Both of these methods utilize the hyper-temporal time-series data that are available from coarse resolution imagery. The novelty of these methods is underpinned by the fact that the temporal dimension of the time-series is considered as a highly sampled (relative to the natural phenological variation) data-stream, and change classification is done by combining standard signal processing based methods for feature extraction with machine learning methods for change classification.

1.3   PROPOSED SOLUTION

As stated previously, change detection methods are required to be sufficiently automated with minimal operator involvement. Machine learning enables computers to make decisions based on volumes of empirical data that are often impossible to analyze in a timeous manner by a single, or even multiple human operators. When considering the use of machine-learning methods for change detection based on remote sensing data, there are a few factors to consider. Firstly, a change metric needs to be calculated. This change metric should effectively quantify the level of change that is associated with each pixel. This change metric is then compared to a threshold value to determine whether a change or no-change decision should be made [21], [22], [23]. The threshold value can be calculated in a supervised or unsupervised manner. In supervised methods, training data are used to determine the distribution of the change metric for both the change and no-change case and an appropriate decision boundary is inferred. One of the main disadvantages of supervised change detection methods is the requirement of a statistically significant *a-priori* database of change and no-change examples [8]. Unsupervised methods, on the other hand, do not require any training data, but this generally comes at the cost of a loss in performance.

In many cases, Univariate Image Differencing (UID) is used [24] to determine the change metric by subtracting two spatially-registered high resolution images, acquired at two different instances, on a per-pixel basis. Each pixel is then classified as either belonging to the change or no-change class by comparing the difference of two co-located pixels (change metric) to a threshold value. The underlying idea is that no-change pixels would typically have a smaller difference than change pixels, and a simple thresholding approach can be used to distinguish between the two possible classes. The selection of this single threshold value is, however, not a trivial task [23, 25, 26], especially when

considering an unsupervised approach. In most cases, the change metric Probability Density Function (PDF) is assumed to be normally distributed [22, 23] (See section 5.4 for details).

The specific sensor that was considered in this thesis is the MODIS sensor on-board the Terra and Aqua satellites. In particular, the freely available and easily accessible MCD43A4 product was used [27]. This product utilizes MODIS data from both satellites and provides high quality 500-meter reflectance data. A bidirectional reflectance distribution function (BRDF) is used to model the values as if they were taken from nadir view [28] which ensures a high level of consistency when considering the hyper-temporal time-series (see section 2.5). Even though some MODIS products are produced at 250 m resolution for the first two bands [27], these products are unfortunately not BRDF corrected and also only use data from either the Terra or Aqua satellites, and do not capitalize on both. Eight day composites are produced from daily data in an attempt to create the most cloud free, high quality dataset. Using this 8-daily composited dataset, a seven-year hyper-temporal time-series of surface reflectance was constructed (Jan. 2001 – Jan. 2008) and consequently used to detect the formation of new human settlements in South Africa. The underlying idea is that one or more hyper-temporal time-series be used as input to a change detection algorithm. The output of the algorithm is a change alarm which produces a change or no-change decision on a per-pixel basis.

To achieve this goal, two change detection methods are proposed in this thesis. The first will be referred to as the Extended Kalman Filter (EKF) change detection method and the second the Temporal Autocorrelation Function (ACF) change detection method. These methods work on a change metric thresholding principle, i.e. a pixel's hyper-temporal time-series is used to calculate a change metric. This change metric is then compared to a threshold value which yields a change or no-change decision. As previously stated, determining a suitable threshold is not a trivial task. A logical approach in selecting this threshold would be to calculate the change metric for a hyper-temporal times-series dataset of change and no-change examples. A threshold value can then be chosen that best discriminates between these two datasets. The problem with this approach is that real change examples are very rare in a regional landscape [17], which makes the availability of a training dataset on change problematic. This requires a new approach to the problem. The fact that real change examples are very difficult to obtain implies that no-change examples are relatively easy to obtain. Land cover change was therefore simulated [29]. This was done by linearly blending a natural vegetation time-series with that of a settlement time-series (for details see section 5.2.2). This enabled the timing and rate of the change to be controlled in order to estimate the necessary threshold parameters without the need for real change examples.
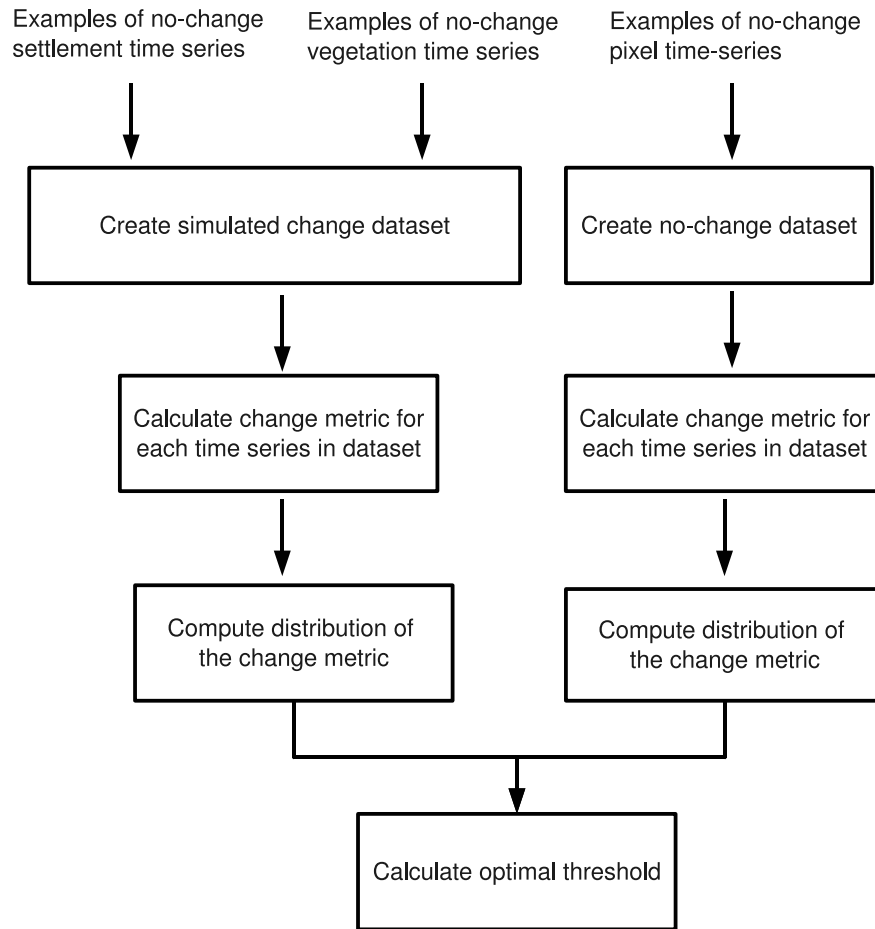
FIGURE 1.2: Off-line optimization phase.

Both the EKF and Temporal ACF change detection methods are supervised, however, the operator only needs to provide examples of "no-change" natural vegetation and settlement pixels. No real or actual change examples are required except for final performance evaluation. As previously stated, the training database requirement for both methods is limited to only no-change examples, which are numerous and can be obtained in large numbers. The no-change examples are then used to generate a simulated change dataset. Both the no-change and simulated change datasets are then used to determine a set of parameters in an off-line optimization phase after which the algorithm is run in an operational and unsupervised manner for the entire study area.

Figure 1.2 shows a general overview of the off-line optimization phase, which is similar for both methods. A set of settlement and natural vegetation time-series examples known not to have changed during the study period is used to create a simulated change dataset. The change metric for each time-series in the simulated change dataset, as well as the no-change dataset, is calculated. The change

Time-series of pixel(x,y)

```
┌─────────────────────────┐
│  Calculate change metric │
└─────────────────────────┘
```

```
┌─────────────────────────┐
│   Compare to threshold   │
└─────────────────────────┘
```

Change or no-change decision for pixel (x,y)
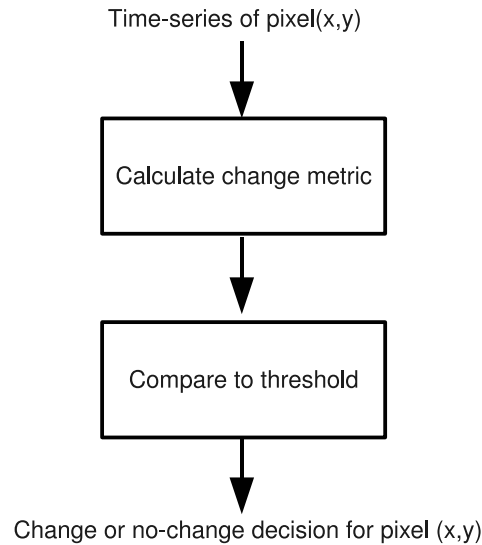
FIGURE 1.3: Operational phase.

metric is merely an index that indicates the amount of change that is associated with the time-series under consideration, i.e. the larger the change metric value, the higher the probability that the specific time-series had undergone a change. The distribution of the change metric, given that a change occurred together with the distribution of the change metric, given that no change occurred, is then used to calculate the optimal threshold.

Figure 1.3 shows a general overview of the operational phase, which is also similar for both methods. The time-series for any arbitrary pixel is used as an input to the algorithm. The change metric is then calculated and compared to the threshold that was calculated in the off-line optimization phase. After thresholding, a change or no-change decision is made. Even though the change detection methodology for both of the proposed change detection methods is similar, the change metric calculation is considerably different; this will become more apparent in the chapters to follow (Sections 5.2 and 5.3)

1.4   OUTLINE OF THIS THESIS

The outline of the thesis is as follows: Chapter 2 gives an overview of some basic remote sensing principles and describes the remotely sensed data that were used, together with an overview of some of the most common change detection methods found in current literature. Chapter 3 gives an introduction to non-linear filtering and in particular the Extended Kalman Filter (EKF), which is a crucial component of one of the proposed change detection methods. Chapter 4 shows that land-cover

class separation can be improved by modeling a normalized difference vegetation index (NDVI) time-series using a triply modulated cosine function and EKF framework to track the model parameters. Chapter 5 follows on the methodology discussed in chapter 2 and extends the EKF framework to the change detection case. The temporal Autocorrelation Function (ACF) change detection method is also introduced in chapter 5. The results obtained by using the EKF and temporal ACF methods are shown in chapter 6. Chapter 7 gives concluding remarks as well as possible future research that could expand on some of the concepts introduced in this thesis.

CHAPTER TWO

REMOTE SENSING DATA FOR LAND-COVER CHANGE DETECTION

Remote sensing is the science of obtaining information about an object or area without being in contact with the object or area under investigation [11]. Using various sensors, data are acquired remotely and analyzed to obtain information about the object that is measured by the sensor. In this thesis, a sensor on board a satellite platform measures the reflection and emission of electromagnetic radiation by the Earth's surface at regular time intervals and these data are then used to infer changes in surface reflectance caused by land cover change.

The objective of this chapter is to give the reader insight into some of the basic principles of satellite remote sensing. A brief history of remote sensing is given in section 2.1 after which the fundamental principles of electromagnetic radiation as well as the interaction of electromagnetic radiation with the atmosphere and Earth's surface is discussed in section 2.2. The concept of resolution in the spectral, temporal, radiometric and spatial context is introduced in section 2.3. The factors considered in choosing a remote sensing system is given in section 2.4 where-after the MODIS sensor is described in section 2.5. Two vegetation indices are discussed in section 2.6 where-after a review of some of the popular change detection methods is presented in section 2.7. Concluding remarks are given in section 2.8.

FIGURE 2.1: The oldest surviving aerial photograph taken by James Wallace Black in 1860 over the city of Boston [11].

2.1   EARLY HISTORY OF REMOTE SENSING

The invention of photography in 1839 was an important first step towards space-borne remote sensing as we know it today. The first known aerial photograph was taken in France by Gaspard Felix Tournament over Bievre, France, but unfortunately those photographs no longer exist [11]. The oldest surviving aerial photograph is one of Boston, taken by James Wallace Black in 1860 (Figure 2.1). The first platforms used for aerial photography were tethered balloons. It was only during the First World War that aircraft were used as platforms for aerial photography to obtain information regarding troop movements, supplies and the effects of bombardments [30]. The use of remote sensing for environmental purposes only became more popular after the Second World War. The technological advances made on airborne camera design during the war were put to civilian use for terrain mapping and assessment. The use of aircraft for remote sensing purposes proved to be expensive and provided data for relatively small areas. The space programs of the 1960s ushered in a new age of remote sensing, using a satellite platform. Satellite technology advanced greatly during the 1960s mainly because of the space race between the USA and former USSR [30]. This new phase of remote sensing can be considered in four broad categories, namely military reconnaissance, manned space flight, meteorological satellites and earth resource satellites. Each of these categories will be explained in more detail in the following sections.

2.1.1 Military reconnaissance satellites

Prior to 1960, aerial photography was mainly used by the United States and the former USSR to monitor each other's military capabilities. In 1958, the possibility of using satellite for military reconnaissance was proposed at the Surprise Attack Conference in Geneva [30]. The first US space observation satellites, which were used for military reconnaissance, were within the CORONA, ARGON and LYNARD programs of the 1960s [30]. These missions were typically very short with any one mission not being more than one or two weeks. These early systems were limited because of the finite amount of film that could be carried. The film canister was ejected and intercepted as it descended to Earth [30]. Later systems stored images in digital format and used telemetry to relay the data to the Earth.

2.1.2 Manned space flight

The first person to orbit the Earth was Yuri Gagarin on 12 April 1961. Even though no photos were taken during this flight, the potential for space-based earth observation became apparent. The USA also commenced its manned space programs in the early 1960s which culminated in the first lunar landing in 1969 [30]. The Mercury program (1961–1963) produced some of the first photographs from a manned capsule and was obtained by the astronauts through the capsule window. The Gemini program in later years (1965–1966) had a more systematic photograph acquisition strategy which captured more than 2 500 photos of the Earth. The Skylab missions (1973–1974) obtained over 44 000 images of the Earth at a spatial resolution of 60–140 m. The space shuttle missions that began in 1981 employed even more sophisticated remote sensing systems. The Russian space missions paralleled those of the American missions, with the Vostok and Voskhod programs being analogous to the Mercury and Gemini missions [30].

Using manned spacecraft as a remote sensing platform has both advantages as well as disadvantages. One of the main advantages is that the manned mission can be used as a test bed for new systems. By using feedback from the ground station, the on-board equipment setup can be modified and optimized by the astronauts. This information can then be used when designing an unmanned satellite. The astronauts could also rectify certain malfunctions with the sensors if and when required. The disadvantage, however, is that manned space missions are more often than not of short duration, which makes continuous and systematic coverage impossible. Another disadvantage is that the ramifications of malfunctions during a manned space mission far outweigh that of an unmanned satellite mission due to possible risk to human life.

2.1.3 Meteorological satellites

Weather forecasting relies heavily on remote sensing satellites to provide readings on temperature, wind speed and the location and movements of storms to name but a few. The movement of major hurricanes can be tracked and predicted accurately by using remote sensing images and can be relayed to the community effectively by means of radio and television broadcasting. Before the advent of remote sensing for weather prediction purposes, major storms could strike unexpectedly, causing massive damage to property and, quite possibly, loss of life. The Television and Infrared Observation Satellite (TIROS-1) meteorological satellite was the first that was used for earth observation and was launched by the United States on 1 April 1960 [30].

Since the initial TIROS-1 satellite, weather satellites have become increasing more advanced. Infrared (IR) data are used to determine information on the temperature at the surface and cloud tops and estimating wind direction and strength by monitoring individual clouds over time. Both polar orbiting and geostationary satellites are utilized for weather prediction [30].

2.1.4 Earth resources satellites

The first earth observation satellite was the Earth Resource Technology Satellite (ERTS-1) launched in July 1972. The ERTS-1 (commonly referred to as Landsat) was designed to acquire multi-spectral medium resolution imagery of the Earth on a systematic and repetitive basis [30]. The data acquired during this mission were made available globally. The underlying idea was that the global remote sensing community would take part in evaluating the subsequent data. The mission was regarded as being very successful and paved the way for continuation of the Landsat series of satellites. The first radar satellite used for remote sensing purposes was the SEASAT satellite, which was launched in 1978 but only provided data for three months. Prior to 1980, the majority of satellites were deployed by the USA and USSR. During the 1980s and onwards, remote sensing systems were developed and commissioned from various agencies around the world, including the French Satellite Pour l'Observation de la Terre (SPOT) series of satellites, the range of Indian Remote Sensing (IRS) satellites, the Japanese Earth Resource Satellite (JERS) and the European Remote Sensing (ERS) satellites to name but a few.

Typically, these space agencies operate independently of one another but in in February 2005 the Group on Earth Observations (GEO) was formally created by resolution of 60 national governments and 40 international organizations. The nations and international organizations involved in GEO resolved that it would implement the Global Earth Observation System of Systems (GEOSS). The primary objective
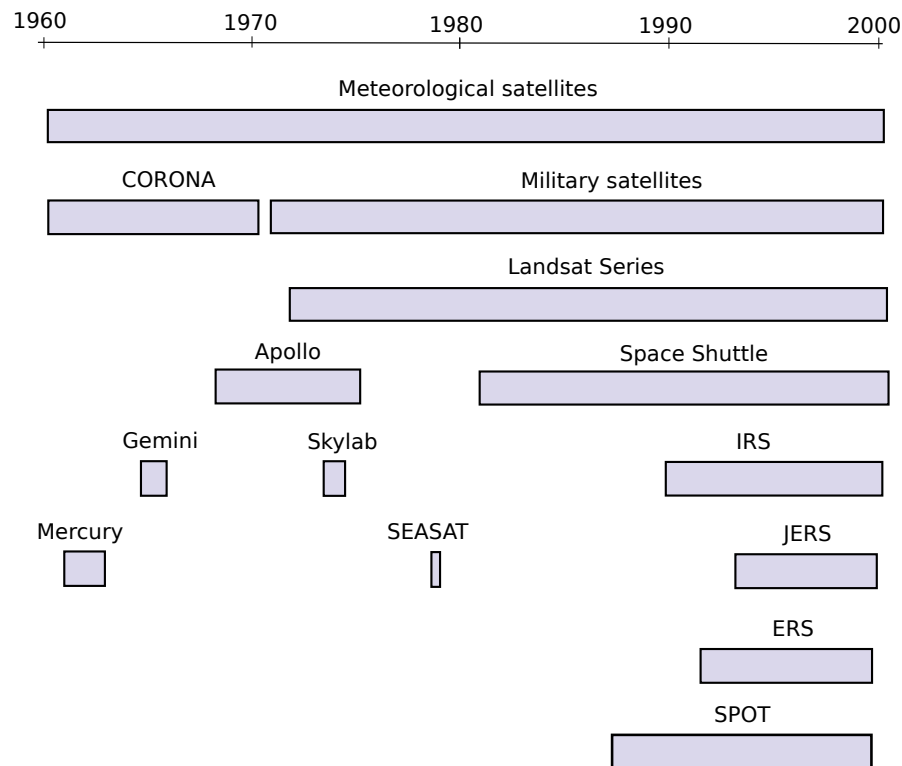
FIGURE 2.2: Time-line spanning from 1960 until 2000 for some of the satellite missions described in the previous sections. Since the first artificial satellite, Sputnik 1, in 1957, a host of nations have successfully launched more than 2 000 satellites into orbit. (Adapted form [30])

of GEOSS is that that timely, quality, long-term, global observations are exchanged in a full and open manner with minimum time delay and minimum cost. They also intend to coordinate efforts to address capacity-building needs related to earth observations [31].
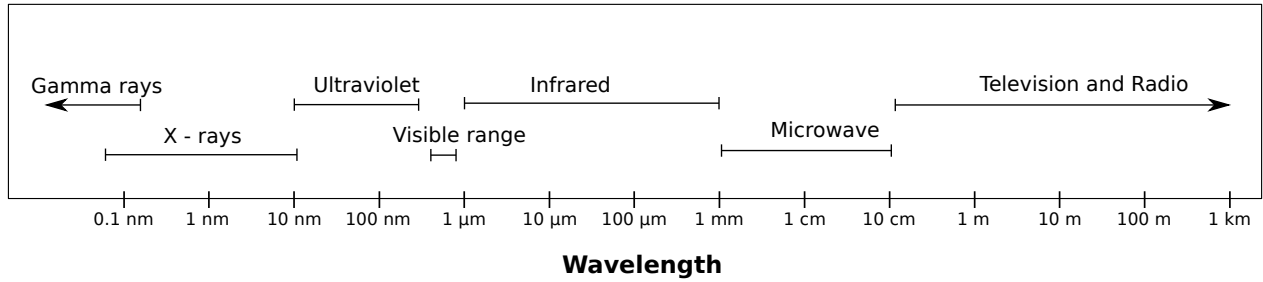
FIGURE 2.3: The electromagnetic spectrum [30].

2.2 ELECTROMAGNETIC RADIATION

Visible light is probably the most familiar form of electromagnetic radiation, but only occupies a very small portion of the entire electromagnetic spectrum. Radio waves, X-rays and Ultra Violet (UV) rays, to mention a few, all form part of the electromagnetic spectrum. In essence, all forms of electromagnetic radiation radiates according to the same wave theory. These waves are characterized by their wavelength and amplitude, all traveling at the speed of light in a vacuum. The electromagnetic spectrum is depicted in Figure 2.3.

The two main approaches to remote sensing are active and passive systems. An active remote sensing system uses its own electromagnetic radiation source. The amount of energy that is reflected back to the sensor is used to infer information about the surface towards which the sensor is directed. A typical example of an active remote sensing system is Synthetic Aperture Radar (SAR). These systems operate in the wavelength range of between 2.4 and 107 cm.

A passive remote sensing system uses the Sun as the source of electromagnetic radiation and measures the reflection from the Earth's surface. The focus of this thesis will be on passive remote sensing systems. The part of the spectrum that is particularly useful for passive remote sensing systems are the visible and infrared (IR) ranges. Table 2.1 gives a further breakdown of these ranges. Multi-spectral scanners often range between 0.4 and 12.0 μm range [11], which ranges from the visible blue range to the long-wave IR range (Table 2.1).

As previously stated, the Sun is the primary source of electromagnetic radiation in passive remote sensing systems. It follows that the properties of the Sun's electromagnetic radiation are of particular importance. Although the Sun produces energy in a wide range of wavelengths, the energy across all the wavelengths is not evenly distributed. Wien's displacement law dictates that the wavelength at which a black body radiates maximum energy is a function of the temperature of the object given

TABLE 2.1: Breakdown of the visible and infrared spectrum.

	Range	Wavelength (μm)
Visible	Blue	0.4 – 0.5
	Green	0.5 – 0.6
	Red	0.6 – 0.7
Infrared	Near IR	0.7 – 1.0
	Short-wave IR	1.0 – 3.0
	Mid-wave IR	3.0 – 5.0
	Long-wave IR	7.0 – 14.0
	Far IR	15.0 – 1000

as [30]:

$$\lambda_m = \frac{A}{T}, \tag{2.1}$$

where λ_m is the wavelength at which the maximum energy is radiated, A is a constant (2898 μm K) and T is the temperature in Kelvin. The Sun's temperature is between 5750 and 6000 K [30]. This implies that the wavelength at which the Sun radiates maximum energy is roughly 0.5 μm. The spectral radiance of electromagnetic radiation as a function of the temperature and wavelength is described by Planck's law [32]:

$$I(\lambda, T) = \frac{2hc^2}{\lambda^5 \left(e^{\frac{hc}{\lambda k T}} - 1 \right)}, \tag{2.2}$$

where λ is the wavelength, T is the temperature, h is the Planck constant, k is the Boltzmann constant and c is the speed of light. Figure 2.4 shows the spectral radiance of the electromagnetic radiation of the Sun for wavelengths between 1 and 2000 nm. It can be seen that the Sun's maximum energy is radiated in the visible spectrum between 400 and 700 nm.

Because of the distance between the Earth and Sun, there is a considerable decrease in intensity across all wavelengths when the electromagnetic radiation reaches the Earth's atmosphere. This can be attributed to the inverse-square law that states that flux density is inversely proportional to the square of the distance from the flux source [32]. However, the spectral distribution across the wavelengths remains nearly unchanged [30]. The atmosphere, on the other hand, has a dramatic effect on the solar radiance that eventually reaches the surface of the Earth. This effect will be discussed in the following
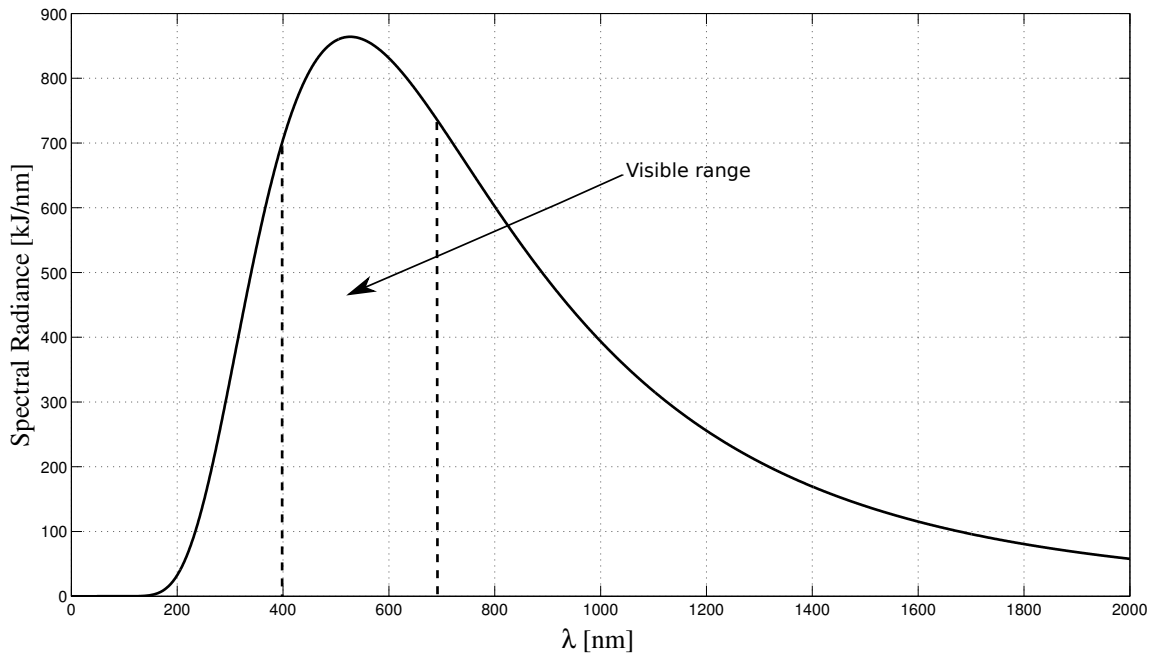
FIGURE 2.4: Solar spectral radiance of the Sun as a function of wavelength.

section.

2.2.1 Interaction of electromagnetic radiation with the atmosphere

The atmosphere has a significant effect on the intensity and spectral composition of electromagnetic radiation that is available to remote sensing systems. The influence of the atmosphere can be partitioned into scattering effects and absorption effects.

Scattering can either be selective or non-selective. Selective scattering depends on the specific wavelength of the radiation. If the wavelength of the electromagnetic radiation is larger than the dimensions of the scatterers (more than 10 times the size), the amount of scattering is inversely proportional to the fourth power of the wavelength [30]. This is commonly referred to as Rayleigh scattering. When the dimensions of the scatterers are approximately the same as the wavelength of the electromagnetic radiation, scattering also occurs. This is commonly referred to as Mie scattering. Non-selective scattering is not wavelength dependent and occurs in aerosols that are approximately 10 times the size of the wavelength. For the visible wavelengths, pollen grains, raindrops and cloud droplets are typical sources of non-selective scattering [30].

Absorption in the atmosphere occurs because gaseous components in the atmosphere act as selective

Table 2.2: Order of magnitude of atmospheric effects for Advanced Very High Resolution Radiometer (AVHRR) band 1 and 2 as well as NDVI. The proportional effect is given as percentage (%) of increase (+) or decrease (-) of the signal. All the other effects as well as effect on NDVI are given in absolute units [33].

	Ozone	**Water vapor**	**Rayleigh**	**Aerosol**
Band 1	4.24% to 12% (-)	0.7% to 4.4% (-)	0.02 to 0.06 (+)	0.005 to 0.12 (+)
Band 2	–	7.7% to 25% (-)	0.006 to 0.02 (+)	0.003 to 0.083 (+)
NDVI (Bare Soil)	0.02 to 0.06 (+)	0.011 to 0.12 (-)	0.036 to 0.094 (-)	0.006 to 0.085 (-)
NDVI (Forest)	0.006 to 0.017 (+)	0.036 to 0.038 (-)	0.086 to 0.23 (-)	0.022 to 0.35 (-)

absorbers [30]. Molecules selectively absorb energy at different wavelengths. The most efficient absorbers in the atmosphere are water vapor, carbon dioxide and ozone [11]. Figure 2.5 shows the atmospheric electromagnetic opacity for different wavelengths. Table 2.2 shows the effect for AVHRR band one and two as well as NDVI as a result of Ozone, water Vapor, Rayleigh scattering and stratospheric aerosol effects. Both AVHRR band one and two are affected by these atmospheric effects and in particular, water vapor and aerosol has a detrimental affect on band 2 and 1 respectively which causes an artificial decrease in NDVI [33] (Table 2.2).

From the aforementioned it can be concluded that, because of the effects of atmospheric absorption and scattering, the observation radiance recorded at the satellite is not a true reflection (NPI) of the radiance from the ground but rather "Top-of-Atmosphere". It follows that atmospheric correction for Rayleigh scattering, gaseous absorption, and aerosol scattering should be a critical pre-processing step when considering land surface studies [34, 35]. For three cases in particular, the omission of atmospheric correction could prove to be detrimental [36]. Firstly, if one were to compute the ratio between two bands of a multispectral image. This is because scattering increases inversely with wavelength which implies that shorter-wavelength measurements are more susceptible than longer-wavelengths and could possibly distort the true ratio. Second, when relating the radiance of a surface in terms of a physically based model, the atmospheric component must be estimated and removed as failure to do so could adversely affect the physically based model if the physically based model does not assume an atmospheric component. Thirdly, when comparing the radiance made at one time (time 1) with the radiance at a different time (time 2), atmospheric correction is crucial as the radiance values recorded by the sensor will most likely vary from time 1 to time 2 because of atmospheric variability [36]. Atmospheric correction is also applicable to time-series analysis
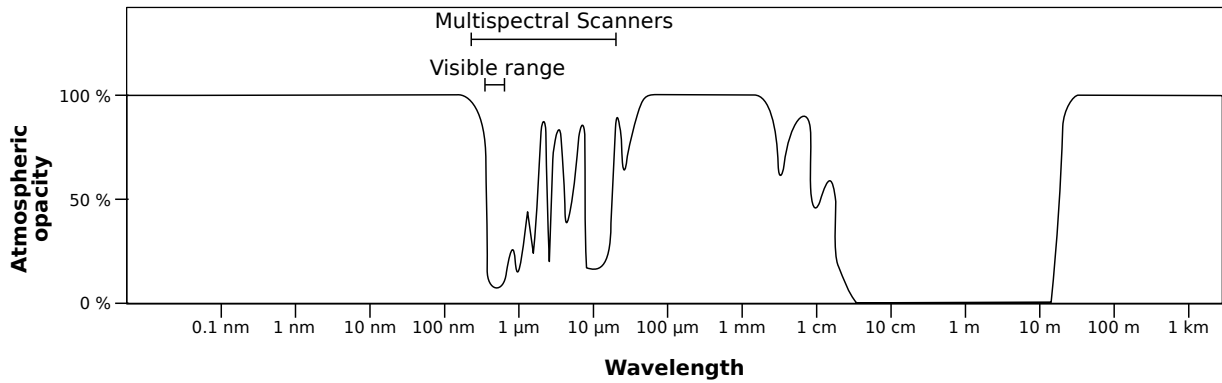
FIGURE 2.5: Atmospheric electromagnetic opacity (modified from [37]).

(considering multiple observations of the same area) as changes in the time-series should only be affected by changes in the surface radiance as opposed to changes in atmospheric conditions.

Atmospheric correction can either be relative or absolute. Relative atmospheric correction uses histogram matching to reference images. This approach requires good reference images for the same or adjoining areas. Absolute correction on the other hand can either be empirical or physical. Empirical methods have the danger of over simplification and are often of limited use. Physical models model the effect of various gas concentrations and compensates for these accordingly. These physical modes are called Radiative Transfer Models (RTM's). Radiative transfer models rely on information from the image itself in order to estimate the path radiance for each spectral band and are limited by the need for data relating to the condition of the atmosphere at the time of imaging. A popular RTM is the 6S code developed by E Vermote *et al.* [38] and is freely available (ftp://loa.univ-lille1.fr/6S/).

2.2.2   Interaction of electromagnetic radiation with a surface

When electromagnetic energy strikes a surface, a certain measure of absorption, reflection and/or transmission can occur. The amount of energy reflected, absorbed and transmitted is a function of the Earth feature (material composition, surface roughness, etc.) and the wavelength of the electromagnetic energy concerned. In remote sensing, the energy that is reflected from the surface is of particular importance as this is the energy that is detected by the sensor. Reflection is primarily a function of the surface roughness. If the surface is very flat, and the angle of reflection (θ_r) equals the angle of incidence (θ_i), most of the energy will be reflected in the direction of the reflection angle. This type of reflection is referred to as *specular* reflection. If the surface is rough compared to the wavelength of the incident electromagnetic radiation, i.e. the ratio between the roughness of the surface and the wavelength is greater than one, the energy is scattered and effectively reflected in all
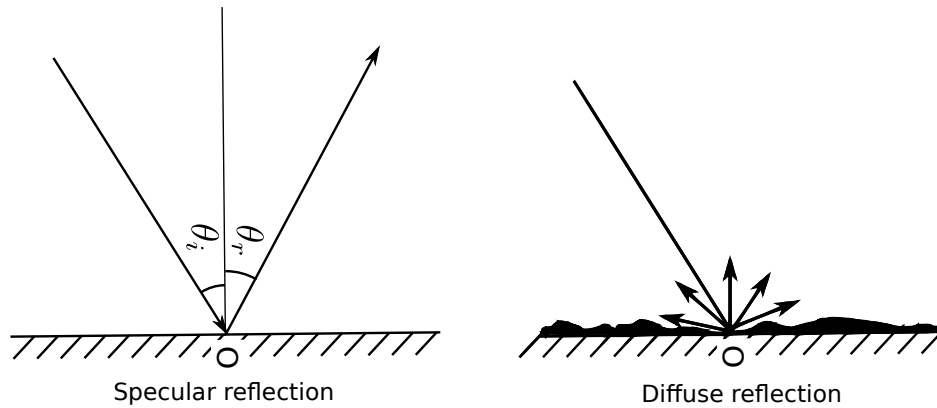
FIGURE 2.6: Specular and diffuse reflection [30].

directions. This type of reflection is referred to as *diffuse* reflection [11]. The broad range of surface types on Earth implies that perfect specular or diffuse reflection would not occur in nature and would lie somewhere between these two extremes [11]. Figure 2.6 illustrated the principle of specular and diffuse reflection.

For remote sensing purposes, diffuse reflection is considered to be more favorable as the reflection is coherent for all viewing angles. Specular reflection, on the other hand, would have a bright reflectance for a specific viewing angle, and relatively little reflection for all other viewing angles. The reflection for most surfaces in nature tend to be more diffuse than specular for the visible and infrared wavelengths with the exception of water [30]. Because surfaces cannot be assumed to be perfectly Lambertian (diffuse reflection), the viewing and solar angles should be considered. All the reflected energy from a ground target over an entire hemisphere is not detected by the satellite sensor, but rather, only the reflected energy returned at a particular angle is recorded [36]. In addition, the reflected energy also depends on the the orientation of the Sun (Figure 2.7 and 2.8). These effects are particularly detrimental for wide-swath sensors [39] as the viewing angle of these sensors can vary considerably between days. The MODIS sensor, for example, has a swath width of approximately 2300 km, which yields a maximum viewing zenith angle of up to $65°$ [28]. It follows that the distribution of radiance as a function of the observation and illumination angles must be taken into consideration. The Bidirectional Reflection Distribution Function (BRDF) is a mathematical function that describes the variability in surface reflection based on the illumination and viewing angles for a specific wavelength. Using the BRDF function to correct for Sun and viewing angle effects is discussed in further detail in section 2.5 when considering the BRDF corrected MODIS product that was used in this study.
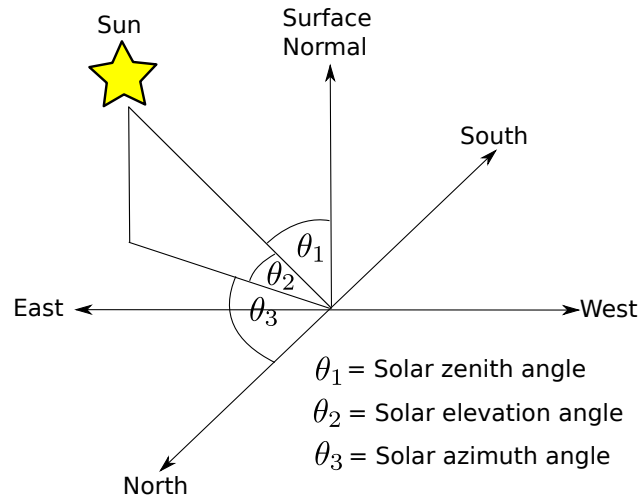
FIGURE 2.7: Solar orientation [36].

The spectral reflection is the ratio between the energy reflected from a surface and the total electromagnetic energy incident on the surface. The spectral reflectance (ρ_λ) is a function of the wavelength and can be written as

$$\rho_\lambda = \frac{E_R(\lambda)}{E_I(\lambda)} \times 100, \tag{2.3}$$

where E_R is the reflected electromagnetic energy and E_I is the electromagnetic energy incident on the surface [11].

The spectral reflectance curve of an object is a graph that shows the spectral reflection for a range of wavelengths. This is sometimes also referred to as the spectral signature of an object. Figure 2.9 shows an example of the spectral reflectance curve for vegetation. The typical valleys in the visible spectrum are due to the absorption characteristics at different wavelengths by the pigments in plant leaves. The strong absorption of chlorophyll in the blue and red band gives rise to the typical green color that is usually associated with healthy vegetation. Water absorption in the 1400, 1800 and 2700 nm band gives rise to the characteristic valleys in the short-wave IR region. As explained in section 2.2.1, water vapor in the atmosphere is an important consideration for atmospheric correction and has also been a limitation of previous land remote sensing instruments, in more recent sensors (for example MODIS), bands are chosen to minimize the impact of absorption by atmospheric gases and in particular water vapor [41].

FIGURE 2.8: Effect of Solar illumination angle variation on reflection [40]. Both photographs taken from the same field but from different directions.
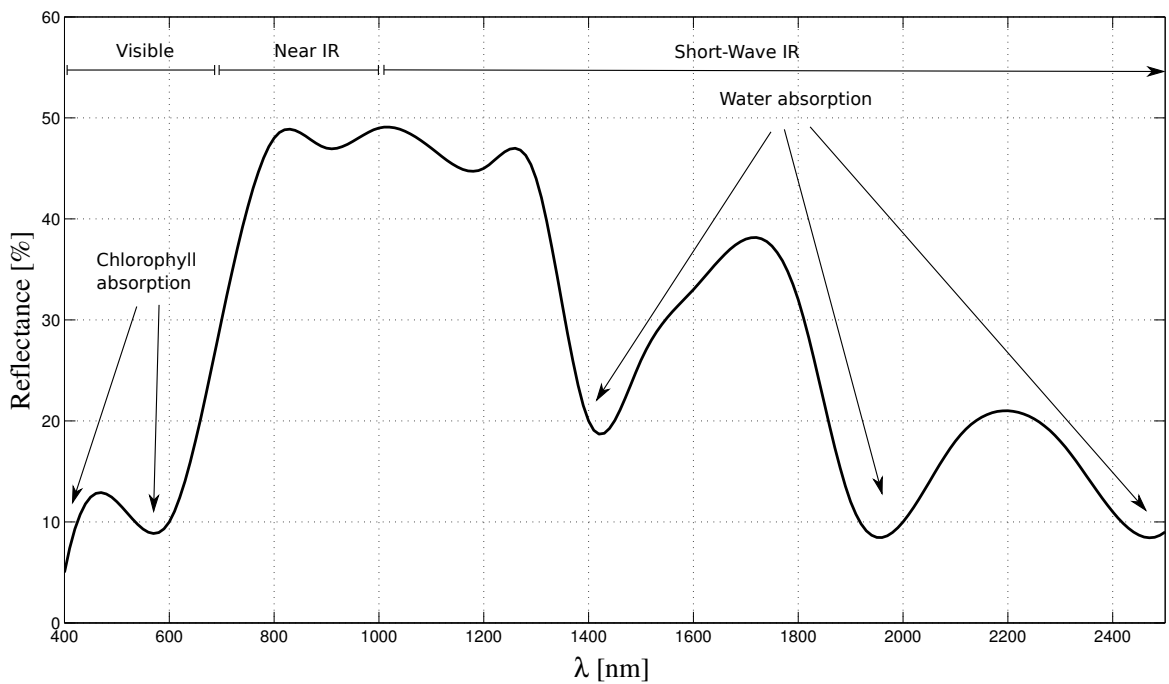
FIGURE 2.9: Typical spectral reflectance curve for vegetation [11].

2.2.2.1 Phenology reflection variation

Even though the spectral reflection curve is broadly similar for specific land-cover types, it is by no means unique. In nature, the spectral signature of similar land-cover types could be highly variable [11, 30]. Even the same land cover type can appear significantly different during certain periods of
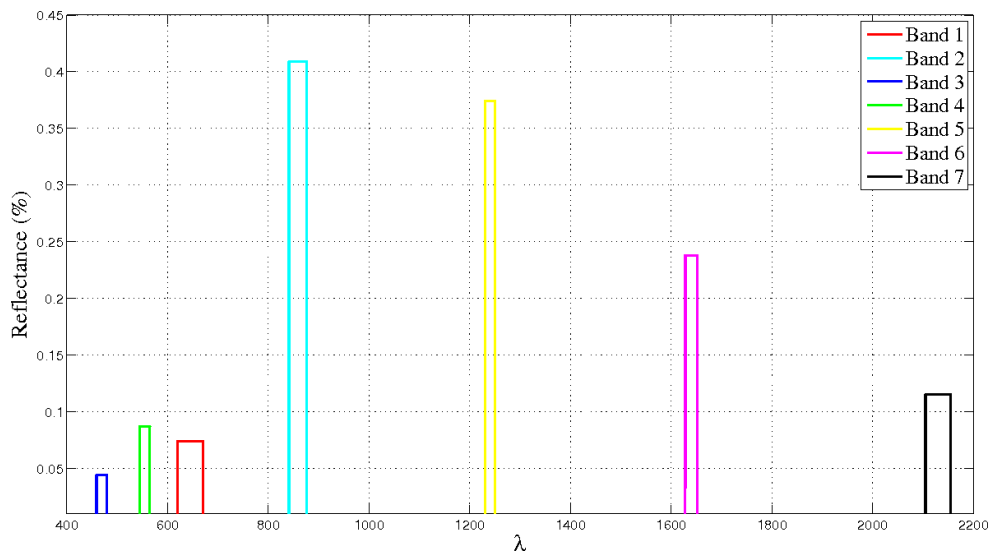
FIGURE 2.10: QuickBird image showing a vegetation area taken in February (courtesy of Google™Earth). The area corresponding to a 500 m MODIS pixel together with the the spectral reflection for all seven MODIS land bands is also shown.

the natural growth cycle. An example of this is shown in the Limpopo province of South Africa. A natural vegetation area corresponding to a 500 m MODIS pixel is shown together with the the spectral reflection of all seven land-bands for February and September respectively (Figures 2.10 and 2.11). It is clear that the spectral signature of a pixel having an unchanged land cover type could vary considerably over time due to seasonal variations. The Near IR band (band 2) in February is high and the red band (band 1) is low due to green vegetation whereas the opposite is true for September.
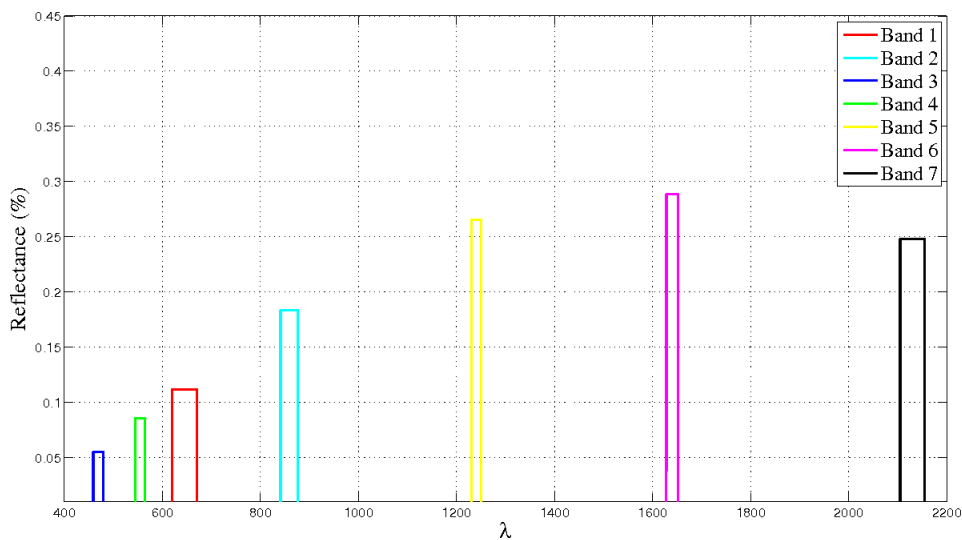
FIGURE 2.11: QuickBird image showing a vegetation area taken in September (courtesy of Google^TM Earth). The area corresponding to a 500 m MODIS pixel together with the the spectral reflection for all seven MODIS land bands is also shown.

2.3 RESOLUTION

In remote sensing, there are four types of resolution that are of interest. These are spectral, temporal, radiometric and spatial resolution. Each of these will be discussed in more detail in the sections that follow.

2.3.1 Spatial

The spatial resolution of an imaging system can be measured in a number of different ways, depending on the user's goals. The pixel size is determined by the altitude, viewing angle and sensor characteristics of the remote sensing system. The most commonly used measure, based on the
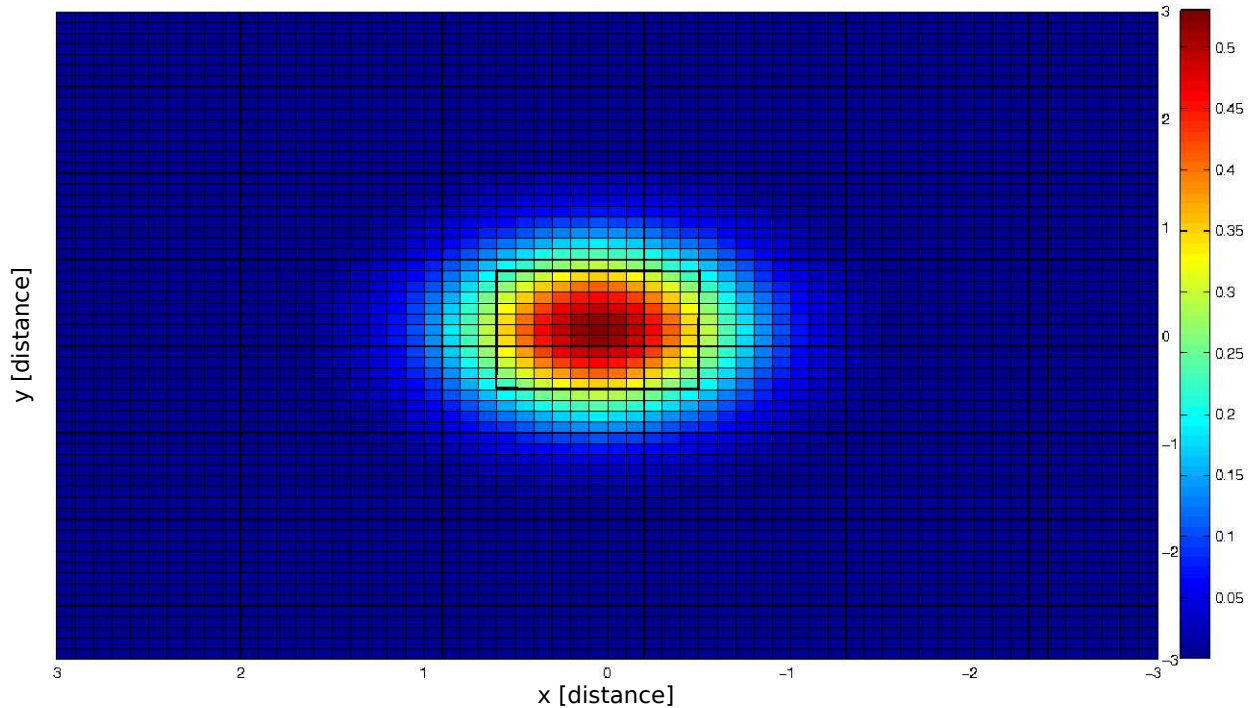
FIGURE 2.12: Illustration of the point spread function, the pixel that is imaged is centered at (0,0) and stretches from -0.5 and 0.5 in both the x and y direction [36].

geometric properties of the imaging system, is the instantaneous field of view (IFOV) which is defined as the area on the ground that is viewed by the instrument at a given altitude and time instance [36]. It should however be noted that no satellite has a perfectly stable orbit and the satellite's height above the Earth could vary by tens of kilometers which in turn influences the IFOV. Another factor to consider is that due to the properties of the optics involved in imaging, a reflective point on the ground does not produce a single bright point on the image but rather a diffused circular region. This phenomenon is characterized by the point spread function (PSF). Figure 2.12 illustrates the concept of the PSF, here, the area of the pixel being imaged is centered around (0,0) and stretches 0.5 in both the x and y direction. It is clear that the signal energy is non-zero outside this range. The ideal point spread function would be a square box centred at (0,0) with a side length of 1.0 [36]. When relatively bright or dark objects are within the IFOV of the sensor, the PSF has the effect of blending or spreading the areas having significantly higher or lower reflectance. This leads to the phenomenon where high-contrast features such as narrow rivers and roads are discernible on some satellite images, even though their width is less than the sensor's spatial resolution. It also has the effect that often, targets with dimensions larger than the satellites IFOV may not be discernible if they do not contrast with their surroundings. The value recorded at the sensor which corresponds with a particular pixel position on the ground is thus not just a average of the radiance from that pixel but there is a high probability that there is a contribution from areas outside the IFOV. A digital image is a set of values being related

LANDSAT-7 panchromatic image (15m resolution)

SPOT-2 panchromatic image (10m resolution)

FIGURE 2.13: Landsat-7 and SPOT-2 panchromatic resolution comparison.

to the radiance from a ground area represented by a single cell or pixel. The IFOV is not the same as the pixel size as pixel values can be interpolated to represent any desired ground spacing [36].

When considering the same geographical area, a higher resolution image of the same area will have an increased data size when compared to a lower resolution image. An informal settlement in the Limpopo province of South Africa is shown in Figure 2.13, which was taken from the Landsat-7 and SPOT platforms respectively. The Enhanced Thematic Mapper (ETM+) sensor on board the Landsat-7 mission has a panchromatic channel with spatial resolution of 15 m, whereas the High-Resolution Visible (HRV) sensor on board the SPOT-2 mission has a panchromatic channel with a spatial resolution of 10 m. The distinct difference in clarity between the two images can be seen clearly when considering these two images of the same area.

2.3.2 Spectral

Remote sensing systems usually employ multi-spectral sensors. As the name suggests, multi-spectral sensors acquire data for multiple spectral bands. The effective bandwidth of the measured bands is directly related to the spectral resolution. For example, in the visible range between 400 and 700 nm, if only one band is used to sense the reflection for the entire band, a single reflectance value would be produced. If the one single band was divided into three sub-bands, namely 400–500, 500–600 and 600–700 nm respectively, three reflectance values corresponding to the blue, green and red band would be produced. One of the advantages of having a higher spectral resolution is that the variations in the spectral signatures of land surfaces can be identified much more easily as the spectral resolution increases. To identify particular targets on a remotely-sensed image, the spectral resolution of the sensor must be as closely matched as possible to the spectral reflectance curve of the intended target [36].

There are also a few drawbacks when increasing the spectral resolution. As the number of spectral channels increases, the data size increases linearly. Another disadvantage is that the Signal-to-Noise Ratio (SNR) is adversely affected when increasing the spectral resolution. The reason for this is that all signals contain some form of noise that is caused by electronic noise from the sensor. The effective signal radiance is less for narrow channels than for wider channels while the additive noise component remains the same, which in turn reduces the SNR. Some airborne sensors have more that 100 spectral bands. These sensors are referred to as hyper-spectral sensors. The sensors that were considered in this thesis typically had fewer than 10 land observation bands [36].

2.3.3 Temporal

Temporal resolution in remote sensing refers to the rate at which the same area is measured. The pre-determined orbit, altitude and swath-width of the satellite means that the rate at which an area is imaged can be determined. The orbital period of a satellite in a circular orbit increases with increasing altitude. Low earth orbit (LEO) satellites typically range between 160 and 2000 km above the Earth's surface and travel at a speed of nearly 8 km per second. Geostationary orbit ranges between 35488 to 36088 km, being centered on 35788 km and satellites in this orbit travel at speeds of around 3 km per second. The advantage of geostationary orbit is that the receiving antenna remains in a fixed position whereas the receiving antenna used to receive data from LEO satellites requires a tracking antenna. Many remote sensing satellites are in a sun-synchronous orbit (600 – 800 km) where the ground observation is always illuminated by the Sun at the same angle when viewed from the satellite [42]. The temporal resolution can vary from hours to weeks depending on the configuration of the remote
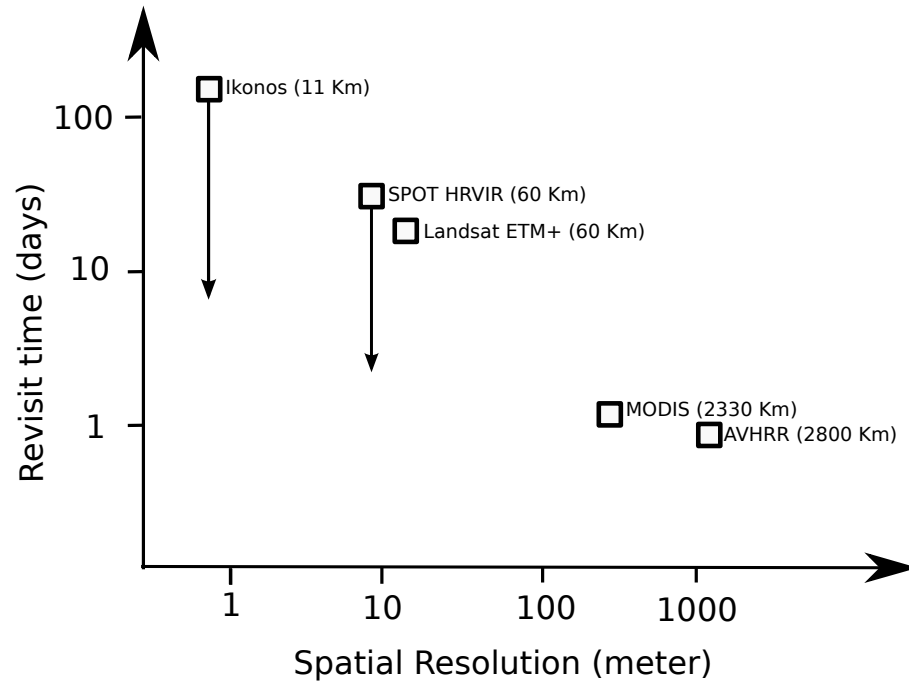
FIGURE 2.14: Relationship between image spatial resolution and satellite imaging revisit period. Instrument swath width is given in brackets and arrows show range of satellite imaging revisit period using sensor off-nadir pointing capability [43].

sensing system [30]. Fixed temporal resolution systems have a fixed viewing angle whereas the variable (off-nadir) viewing capabilities of later systems have the ability to alter the temporal resolution. The advantage of utilizing off-nadir viewing capability is that by changing the viewing angle slightly, the same area could be imaged on consecutive orbits. The disadvantage of this approach, however, is that while some areas can be imaged more frequently, other locations that may have been imaged from the same point are omitted which increases the revisit time for these areas [43]. In essence, fixed temporal acquisitions are not possible using variable viewing capabilities. The Ikonos sensor, for example, has a satellite repeat cycle of 140 days which can be increased to 3 – 4 days by making use of the pointing capability of the instrument. Crucially, imagery are thus only recorded based on user demand which implies that there is no regular repeated coverage for any part of the Earth's surface [43]. It should also be noted that there is a trade-off between spatial and temporal resolution of satellite data. The underlying idea is that the data from narrow swath instruments, having a finer spatial resolution, is less frequently available than wide swath sensors, having coarser spatial resolution data (Figure 2.14). The advantage of having equally spaced, frequently sampled acquisitions of the same area will become apparent in sections and chapters to follow.

2.3.4   Radiometric

Radiometric resolution refers to the number of digital quantization levels used to represent the data observed by the sensor. A higher quantization level usually implies a greater level of detail in the information that is collected by the sensor. If one were to consider a digital image composed of only two levels (black and white), each pixel could either be represented using a single bit with 0 representing black and 1 representing white. If we were to increase the number of bits to 6-bits, there would be 64 unique levels (000000_2 to 111111_2 in binary notation). It should be noted that the number associated with each quantization level is not a direct measurement of ground-leaving radiance but rather the steps into which a range of physical values is divided. Consider, for example, that the sensor is able to measure radiance in the range 0 to 10 $\text{Wm}^{-2}\text{sr}^{-1}$ μm^{-1} and each pixel could be represented as an 8-bit value (i.e. 2^8=256 unique levels). The entire radiance range could be quantized in 256 levels with the difference between each level being (10 – 0)/255=0.00392 $\text{Wm}^{-2}\text{sr}^{-1}$ μm^{-1}. In an effort to distribute the incoming radiance more evenly over radiance range, some sensors can dynamically change their gain to maximize the resolution by taking into account the expected brightness conditions without saturating the detectors. The idea is that the gain can be lowered when surface brightness is expected to be high and increased when surface brightness is expected to be low.

The step size from one level to the next has to be more than the noise level of the sensor to ensure that the change in a level was caused by a real change in the radiance rather than a fluctuation in radiance caused by the noise. It follows that the SNR directly influences the quantization level. Low quality sensors having a high noise level would thus have a lower radiometric resolution compared with low noise sensors [36]. The disadvantage of increased radiometric resolution is an increase in the data size. Most remote sensing systems have 6 or more bits of radiometric resolution [30].

2.4   CHOOSING A REMOTE SENSING SYSTEM

Since the beginning of the remote sensing era, remote sensing satellite data have provided researchers with an effective way to monitor and evaluate land-cover changes [8, 14, 44]. A wide spectrum of sensors can be utilized for change detection and the focus is typically on the application requirement when selecting the most appropriate sensor.

When selecting the right sensor for detecting land cover conversion, the most important consideration is the spatial and temporal resolution. High resolution sensors have the advantage of identifying much smaller objects than coarse resolution sensors, but at a much lower temporal resolution. Change

TABLE 2.3: Comparison of remote sensing satellite sensors.

Sensor	Revisit time	Swath Width	Spatial Resolution	Wavelength range	No. of bands
Advanced Space borne Thermal Emission and Reflection Radiometer (ASTER)	16 Days	60 km	15 – 90 m	0.52 – 11.65 μm	14
Enhanced Thematic Mapper Plus (ETM+)	16 days	185 km	15 – 60 m	0.45 – 12.5 μm	8
MODerate-Resolution Imaging Spectroradiometer (MODIS)	1–2 days	2330 km	250 – 1000 m	0.4 – 14.4 μm	36
Advanced Very High Resolution Radiometer (AVHRR)	Daily	3000 km	1100 m	0.58 – 12.5 μm	5

detection is possible by comparing two high resolution images taken at different dates, but this can, however, be problematic, because similar land cover types can appear significantly different at various stages of the natural growth seasonal cycle [17]. To mitigate this problem it was shown by R.S Lunetta *et al.* in [45] and [46] that the temporal frequency of the remote sensing data acquisitions should be high enough to distinguish change events from phenological cycles [45, 46]. The high temporal frequency makes the use of coarse spatial resolution imagery very attractive for change detection [16].

To illustrate this, two narrow-swath and two wide-swath sensors typically used in land-monitoring remote sensing applications are shown (Table 2.3). The first two examples, Advanced Space-borne Thermal Emission and Reflection Radiometer (ASTER) and ETM+ each have a maximum panchromatic spatial resolution of 15 m with a swath width of 60 and 185 km respectively. The pair of examples, MODerate-Resolution Imaging Spectroradiometer (MODIS) and Advanced Very High Resolution Radiometer (AVHRR) have a much lower spatial resolution (250 m–1100 m) but with a much wider swath width of 2330 and 3000 km respectively. The wide swath width enables the same pixels to be sampled nearly every day and as such provides a very high temporal resolution.

The MODIS sensor was chosen for this thesis because of its wide swath-width and medium spatial resolution capabilities. The following section describes the MODIS sensor in more detail.

2.5   MODERATE-RESOLUTION IMAGING SPECTRORADIOMETER

MODIS was developed by NASA for scientific purposes and is the principal sensor on board the Terra and Aqua satellites. Terra, also commonly referred to as EOS-AM-1, was launched on December 18, 1999 from the Vandenberg Air force base. Development of the Terra satellite was a joint mission between the USA, Canada and Japan [47]. Apart from MODIS, Terra carries the Advanced Space borne Thermal Emission and Reflection Radiometer (ASTER), Clouds and the Earth's Radiant Energy System (CERES), Multi-angle Imaging SpectroRadiometer (MISR) and Measurements of Pollution in the Troposphere (MOPITT) sensors. Aqua, also commonly referred to as EOS-PM-1, was launched from the Vandenberg Air Force Base on May 4, 2002. Apart from the MODIS instrument, Aqua carries the Advanced Microwave Scanning Radiometer-EOS (AMSR-E), Advanced Microwave Sounding Unit (AMSU-A), Atmospheric Infrared Sounder (AIRS), Humidity Sounder for Brazil (HSB) and Clouds and the Earth's Radiant Energy System (CERES) sensors.

The MODIS design team put particular emphasis on instrument calibration as this is critical in generating accurate long-term time-series data for global change studies [48]. The Terra and Aqua satellites orbit the globe in a sun-synchronous orbit at an altitude of 705 km. The MODIS sensor has 36 spectral bands between 0.405 and 14.385 μm with on-board calibration systems [48]. The first two bands have a spatial resolution of 250 m with bands three to seven having a spatial resolution of 500 m. Bands eight through 36 have a spatial resolution of 1 km. The MODIS instrument makes use of a cross-track scan mirror, collecting optics and individual detector elements [49]. The swath dimensions of MODIS are 2330 km (across track) by 10 km (along track at nadir) which, at a resolution of 500 m, produces 20 lines in a single scan [49]. It should be noted however that the 500 m resolution is at nadir and that the pixels size increases slightly in the scan direction which causes pixels to be partially overlapping at off-nadir angles [50]. This is commonly known as the bow-tie effect and is a source of variability over the revisit cycle.

The MODIS instrument data are converted systematically into terrestrial, atmospheric and oceanic products. The first seven bands are typically used for land applications and are often referred to as the MODIS land bands. The bands were chosen to minimize the impact of absorption by atmospheric gases and in particular water vapor, which has been a limitation of the previous instruments for land remote sensing [41] (see section 2.2.1). Table 2.4 gives a description of the specific wavelength and

bandwidth of each of the land bands [51].

TABLE 2.4: MODIS spectral band properties and characteristics.

Band	Wavelength [nm]	Resolution [m]	Primary Use	Spectral range
Band 1	620–670	250	Land/Cloud/Aerosols Boundaries	Visible (Red)
Band 2	841–876	250	Land/Cloud/Aerosols Boundaries	Near IR
Band 3	459–479	500	Land/Cloud/Aerosols Properties	Visible (Blue)
Band 4	545–565	500	Land/Cloud/Aerosols Properties	Visible (Green)
Band 5	1230–1250	500	Land/Cloud/Aerosols Properties	Short Wave IR
Band 6	1628–1652	500	Land/Cloud/Aerosols Properties	Short Wave IR
Band 7	2105–2155	500	Land/Cloud/Aerosols Properties	Short Wave IR
Band 8	405–420	1000	Ocean Color/Phytoplankton/Biogeochemistry	Visible (Blue)
Band 9	438–448	1000	Ocean Color/Phytoplankton/Biogeochemistry	Visible (Blue)
Band 10	483–493	1000	Ocean Color/Phytoplankton/Biogeochemistry	Visible (Blue)
Band 11	526–536	1000	Ocean Color/Phytoplankton/Biogeochemistry	Visible (Green)
Band 12	546–556	1000	Ocean Color/Phytoplankton/Biogeochemistry	Visible (Green)
Band 13	662–672	1000	Ocean Color/Phytoplankton/Biogeochemistry	Visible (Red)
Band 14	673–683	1000	Ocean Color/Phytoplankton/Biogeochemistry	Visible (Red)
Band 15	743–753	1000	Ocean Color/Phytoplankton/Biogeochemistry	Near IR
Band 16	862–877	1000	Ocean Color/Phytoplankton/Biogeochemistry	Near IR
Band 17	890–920	1000	Atmospheric Water Vapor	Near IR
Band 18	931–941	1000	Atmospheric Water Vapor	Near IR
Band 19	915–965	1000	Atmospheric Water Vapor	Near IR
Band 20	3660–3840	1000	Surface/Cloud Temperature	Mid Wave IR
Band 21	3929–3989	1000	Surface/Cloud Temperature	Mid Wave IR
Band 22	3929–3989	1000	Surface/Cloud Temperature	Mid Wave IR
Band 23	4020–4080	1000	Surface/Cloud Temperature	Mid Wave IR
Band 24	4433–4498	1000	Atmospheric Temperature	Mid Wave IR
Band 25	4482–4549	1000	Atmospheric Temperature	Mid Wave IR
Band 26	1360–1390	1000	Cirrus Clouds Water Vapor	Near IR
Band 27	6535–6895	1000	Cirrus Clouds Water Vapor	Mid Wave IR
Band 28	7175–7475	1000	Cirrus Clouds Water Vapor	Long Wave IR
Band 29	8400–8700	1000	Cloud Properties	Long Wave IR
Band 30	9580–9880	1000	Ozone	Long Wave IR
Band 31	10780–11280	1000	Surface/Cloud Temperature	Long Wave IR
Band 32	11770–12270	1000	Surface/Cloud Temperature	Long Wave IR
Band 33	13185–13485	1000	Cloud Top	Long Wave IR
Band 34	13485–13785	1000	Cloud Top	Long Wave IR
Band 35	13785–14085	1000	Cloud Top	Long Wave IR
Band 36	14085–14385	1000	Cloud Top	Long Wave IR
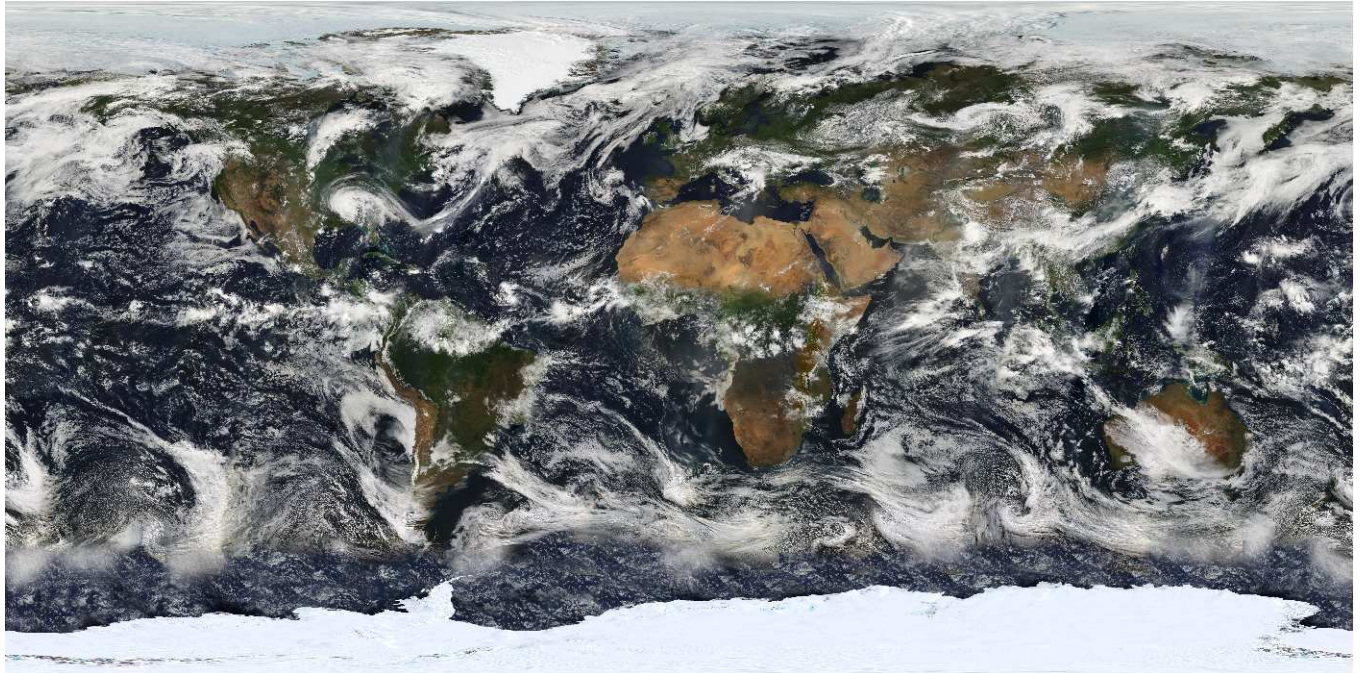
FIGURE 2.15: MODIS mosaic of the Earth [52].

TABLE 2.5: MODIS land products.

Code	Platform	Description
Radiation balance product suite		
MOD09 / MYD09	Aqua / Terra	Surface Reflectance
MOD11 / MYD11	Aqua / Terra	Surface Temperature and Emissivity
MOD43 / MYD43 / MCD43	Aqua / Terra / Combined	BRDF/Albedo
MOD43 / MYD43 / MCD43	Aqua / Terra / Combined	BRDF/Albedo
Vegetation Product Suite		
MOD13 / MYD13	Aqua / Terra	Vegetation Indices
MOD15 / MYD15 / MCD15	Aqua / Terra / Combined	Leaf Area Index - FPAR
MOD17 / MYD17	Aqua / Terra	Gross Primary Productivity
Land-Cover Product Suite		
MOD12 / MCD12	Aqua / Combined	Land-Cover Type
MOD14 / MYD14	Aqua / Terra	Thermal Anomalies and Fire
MOD44	Aqua	Vegetation Continuous Fields

Because of the large swath size, the same location can be observed every one to two days. It should be noted that that the viewing angle of these daily observations differ from one another in a repeating

FIGURE 2.16: MODIS sinusoidal projection [27].

pattern of 16 days. The reason for this is that the MODIS instrument repeat cycle of nadir overpasses is 16 days which implies that every 16 days the MODIS instrument will be traveling on nearly the exact same path [49]. The radiometric resolution of the sensor is 12 bits, which results in 4096 unique levels (2^{12}). A color composite image using the MODIS instrument is shown in Figure 2.15. Table 2.5 shows some of the most common MODIS products.
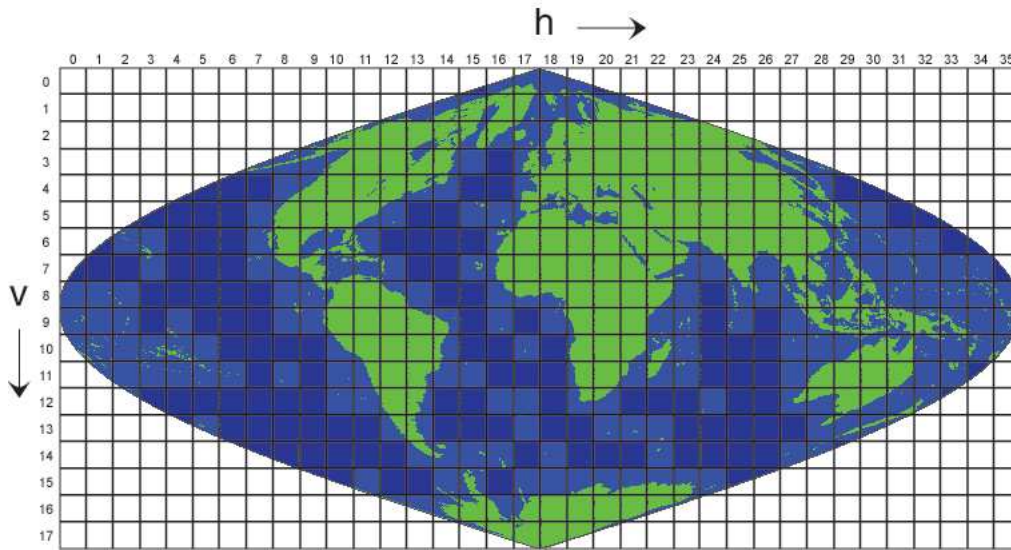
The data product that was chosen in this thesis was MCD43A4 For a complete list of MODIS products see [27]., which is based on the MCD43 BRDF/Albedo radiance product (Table 2.5). The prefix "MOD" and "MYD" of the product code refers to data acquired using the Aqua and Terra satellites respectively. The "MCD" prefix is used to indicate that data from both satellites were used. The MCD43A4 product is derived using a surface reflectance product which is defined as being the measured reflectance from the land surface in the absence of the atmosphere and performs corrections for the effect of gaseous absorption, molecules and aerosol scattering [33, 51]. The MCD43A4 product also takes into account the BRDF (See section 2.2.2) to adjust the reflectance values as if they were taken from nadir view. It does this by utilizing 16 days' worth of multi-date data of both the Terra and Aqua satellites together with a semi-empirical kernel-driven bidirectional reflectance model to determine a global set of parameters describing the BRDF of the land surface. This is then used to determine the hemispherical reflectance as well as the bi-hemispherical reflectance at the solar zenith angle corresponding to local solar noon to produce a coarse resolution (500 m for all bands) composite image every 8 days [28].

TABLE 2.6: Coefficients for equations 2.5 and 2.6.

Term	Isotropic (iso)	RossThick (vol)	LiSparseR (geo)
g0	1.0	-0.007574	-1.284909
g1	0.0	-0.070987	-0.166314
g2	0.0	0.307588	0.041840
g	1.0	0.189184	-1.377622

The algorithm used for BRDF correction uses a kernel-driven, linear BRDF model having a weighted sum of an isotropic parameter and two functions of viewing and illumination geometry used to determine reflectance [28]

$$R(\theta, v, \phi, \lambda) = f_{\text{iso}}(\lambda) + f_{\text{vol}}(\lambda)K_{\text{vol}}(\theta, v, \phi, \lambda) + f_{\text{geo}}(\lambda)K_{\text{geo}}(\theta, v, \phi, \lambda), \tag{2.4}$$

where θ is the solar zenith angle, v is the view zenith, ϕ is the relative azimuth angle and λ is the wavelength. $K_{\text{vol}}(\theta, v, \phi, \lambda)$ is derived from volume scattering radiative transfer models and $K_{\text{geo}}(\theta, v, \phi, \lambda)$ is derived from geometric shadow casting theory. The RossThick kernel expression for K_{vol} and the LiSparce kernel expression for K_{geo} have been identified as the best suited combination for the operational MODIS BRDF/Albedo algorithm [28].

BRDF model parameters are provided in the MOD43B1 product and can be used to compute the albedos with the solar illumination geometry by making use of the following polynomial used to model black-sky and white sky albedos respectively

$$\begin{aligned}
\alpha_{\text{bs}}(\theta, \lambda) = &f_{\text{iso}}(\lambda)(g_{0\text{iso}} + g_{1\text{iso}}\lambda^2 + g_{2\text{iso}}\lambda^3) + \\
&f_{\text{vol}}(\lambda)(g_{0\text{vol}} + g_{1\text{vol}}\lambda^2 + g_{2\text{vol}}\lambda^3) + \\
&f_{\text{geo}}(\lambda)(g_{0\text{geo}} + g_{1\text{geo}}\lambda^2 + g_{2\text{geo}}\lambda^3),
\end{aligned} \tag{2.5}$$

and

$$\alpha_{\text{ws}}(\theta, \lambda) = f_{\text{iso}}g_{\text{iso}} + f_{\text{vol}}g_{\text{vol}} + f_{\text{geo}}g_{\text{geo}}. \tag{2.6}$$

The coefficients used in equations 2.5 and 2.6 are given in table 2.5. In the MCD43A4 product, the solar zenith angle is transformed to the angle at local solar noon [49], which results in a high degree

of reflection consistency when using multiple images to construct a pixel time-series. The composite image is in the form of a sinusoidal projected tile. Figure 2.16 shows the sinusoidal projection tiles of $10° \times 10°$. Each tile is in the HDF-EOS file format having 2400×2400 pixels. This thesis focuses on the h20v11 tile (Figure 2.16). Figure 2.17 shows the outline of a $500\,\text{m} \times 500\,\text{m}$ MODIS pixel in the Gauteng province of South Africa, together with its corresponding seven-year time-series for all seven land bands spanning from 2001/01 to 2008/01.

When considering optical measures of vegetation canopy greenness, Vegetation Indices (VIs) are often considered [53]. VIs uses band combinations that provide consistent spatial and temporal comparisons for monitoring photosynthetic activities [48]. Two of the most common VIs will be discussed in the following section.

2.6 VEGETATION INDICES

The study of terrestrial vegetation in large-scale global processes is one of the primary interests in earth observation. This requires an understanding of the biophysical and structural properties as well as temporal variations of vegetation. Vegetation indices (VIs) are spectral transformations of two or more spectral bands designed to enhance the contribution of vegetation properties and allow comparison of terrestrial photosynthetic activity variations. VIs are widely used in the estimation of leaf area index, fraction of absorbed photosynthetically-active radiation, chlorophyll content, vegetation fraction, photosynthesis, transpiration and net primary production [54].

VI measurements combine the chlorophyll-absorbing visible red spectral region with the near-infrared (NIR) spectral region (which has a high reflection in the case of green vegetation) to provide a consistent and robust measure of area-averaged canopy photosynthetic capacity [55]. This simple transformation of spectral bands enables monitoring of seasonal, inter-annual, and long-term variations of vegetation parameters [53]. Two VIs, the normalized difference vegetation index (NDVI) and enhanced vegetation index (EVI), will be considered in this section.

2.6.1 Normalized difference vegetation index

Normalized Difference Vegetation Index (NDVI) is a vegetation index that has been successfully used in many studies related to vegetation [53]. NDVI is a normalized ratio of the Near IR and red bands,

$$\text{NDVI} = \frac{\rho_{\text{NIR}} - \rho_{\text{red}}}{\rho_{\text{NIR}} + \rho_{\text{red}}}, \tag{2.7}$$
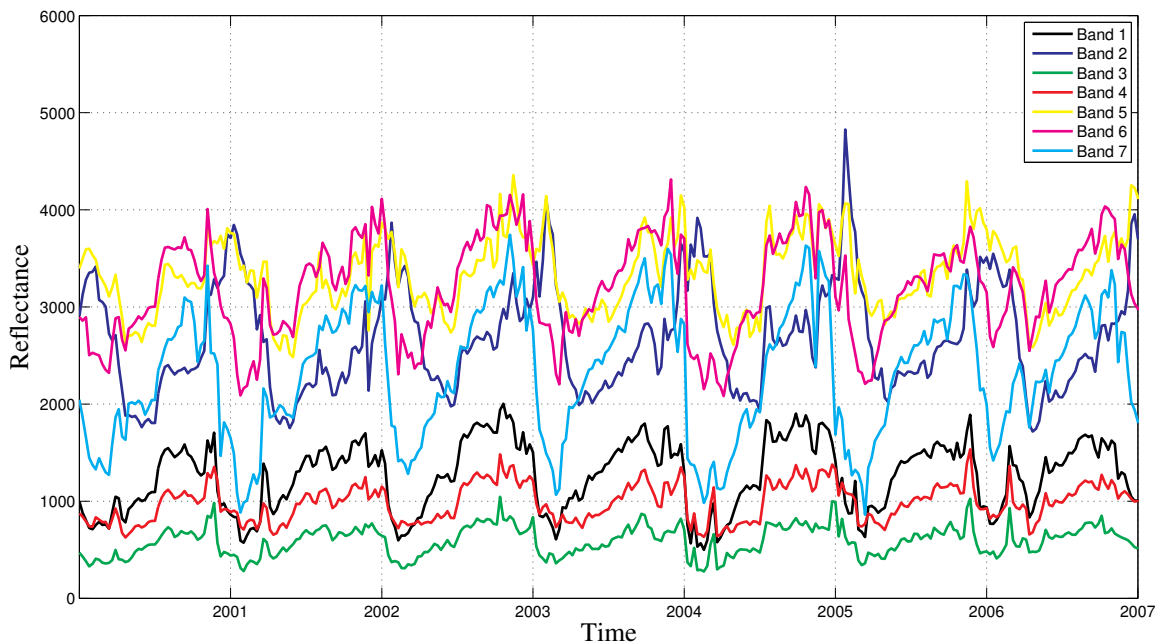
FIGURE 2.17: MODIS pixel and corresponding seven year time-series spanning from 2001/01 to 2008/01 (courtesy of Google$^{\text{TM}}$Earth).

where ρ_{NIR} and ρ_{red} is the surface reflectance of the Near IR and red bands respectively. These bands correspond to MODIS band two and one respectively (Table 2.4). The rationale behind the index is that Photosynthetically Active Radiation (PAR), which is in the 400–700 nm wave band, is used in the process of photosynthesis. This results in a strong absorption of these wavebands as was shown in Figure 2.9. Wavelengths longer than 700 nm are not used for photosynthesis and are reflected due to
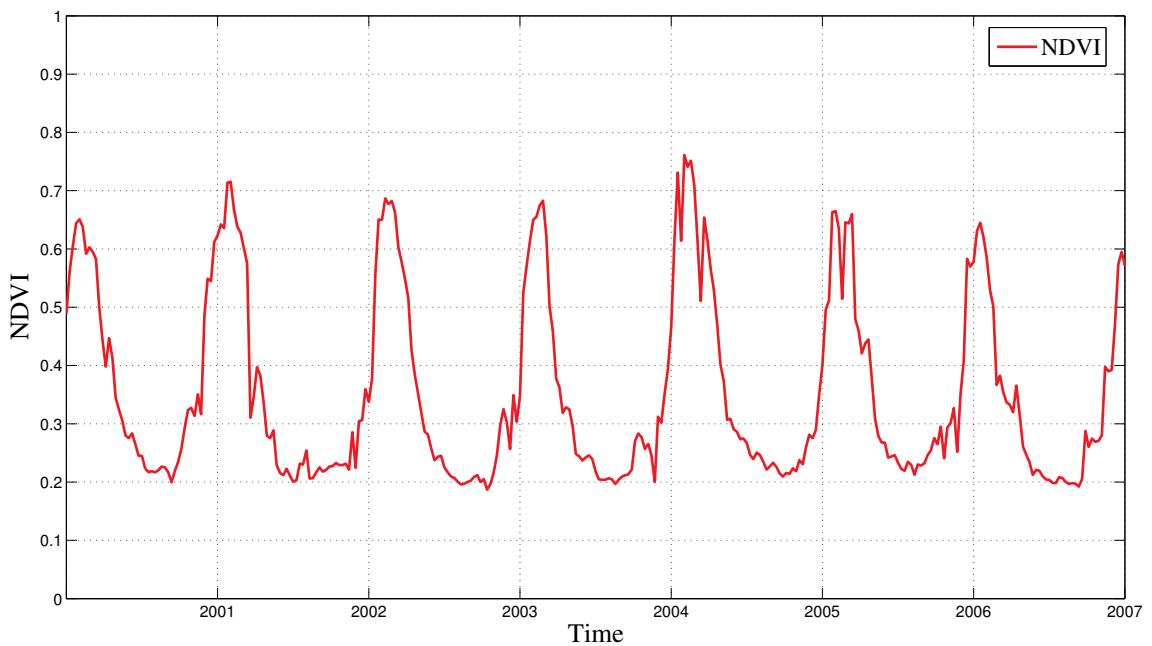
FIGURE 2.18: QuickBird image of an area in northern South Africa (courtesy of Google™Earth). A polygon representing the area covered by a 500 m MODIS pixel together with the corresponding seven-year NDVI time-series spanning from 2001/01 to 2008/01 is also shown.

the internal cell structure of green vegetation [55]. This results in the characteristic low percentage of reflection in the visible region relative to the near IR region of green vegetation (Figure 2.9).

NDVI is a good vegetation measure in the sense that its stability enables meaningful comparisons of seasonal and inter-annual changes in vegetation greenness, growth and activity [53]. NDVI time-series

data have been used in various operational applications including image segmentation methods, land-cover classification, climate studies and change detection [17, 56–58]. The NDVI time-series for the pixel shown in Figure 2.17 is shown in Figure 2.18.

2.6.2   Enhanced vegetation index

The enhanced vegetation index (EVI) optimizes the vegetation signal with improved sensitivity in high biomass regions because of an increased dynamic range, which in the case of NDVI, has a tendency to saturate in high biomass regions [53]. Vegetation monitoring is also improved through de-coupling of the canopy background signal. EVI is calculated as:

$$EVI = G \frac{\rho_{NIR} - \rho_{red}}{\rho_{NIR} + C_1 \times \rho_{red} - C_2 \times \rho_{blue} + L},$$
(2.8)

where ρ_{NIR}, ρ_{red} and ρ_{blue} is the surface reflectance of the Near IR, red and blue bands respectively, L is the canopy background adjustment term, C_1, C_2 are the coefficients of the aerosol resistance term and G is the gain term. The rationale behind the the scaled blue band and red band term is based on the wavelength dependency of the aerosol effects. The blue band is more atmosphere-sensitive and is used to correct the red band for aerosol influences. The canopy background correction term (L) is used since 70% of the terrestrial surface has open canopies with canopy background signals having some effect on the canopy reflectance properties. The coefficients adopted in the MODIS EVI algorithm are, $L = 1$, $C_1 = 6$, $C_2 = 7.5$, and G (gain factor) = 2.5 [53].

2.6.3   Using vegetation indices for land cover change detection

NDVI is the most widely used VI when considering land cover change detection [12, 20, 57, 59–61]. This could be attributed to the simplicity of calculating the NDVI metric as well as the ability to be calculated for sensors that do not have a blue band. Our preliminary results shows that the performance of the methods presented in this study was not influenced considerably by the choice of vegetation index (NDVI vs. EVI). It was consequently decided to use NDVI time-series data as input to the change detection method presented here in order to maximize comparability with previous studies so that the change detection ability could be attributed to the method rather than the choice of index. Although only NDVI data were used, it should be noted that all the change detection methods presented in this thesis could be adapted to other vegetation indices.

2.7   CHANGE DETECTION METHODS

There is no single solution to change detection for all applications. Different change detection methods have their own merits with no single approach being optimal for all change scenarios [15]. Monitoring changes on the surface of the Earth is a dynamic topic with new techniques being continuously developed [14, 15]. There are three major steps involved when developing a change detection framework. The first step is to perform image pre-processing which includes geo-location and image registration, radiometric and atmospheric correction. The goal of this step is to ensure that the data are consistently processed through time and that changes in surface reflectance are not caused by processing artifacts. For example, if two images are not properly co-registered, the location of a pixel in the first image will not correspond with the co-located pixel in the second image, resulting in an erroneous change detection for that pixel. Various studies have shown the adverse effect on change detection accuracy in the event of mis-registration [62–64]. The second step is to implement a suitable change detection method that produces information on where and in some cases when changes occurred in the area in question. In the the third step, an accuracy assessment is performed to quantify the performance of the algorithm using a ground truth dataset.

A distinction can be made between multi-temporal and hyper-temporal change detection methods. Multi-temporal change detection methods usually takes as input a few images (in the order of 2–5) [14, 15] whereas hyper-temporal change detection methods make use of a series of images (up to hundreds) taken at regular, constant intervals, usually a few (8 – 30) days apart. The vast majority of change detection algorithms in the literature are based on medium to high resolution multi-temporal change detection with only a limited number of hyper-temporal change detection methods [14, 15].

Most multitemporal change detection methods found in the literature can broadly be classified into two categories. In the first, two pixels are used as input to a mathematical function to produce a change metric. The second step is then to classify the change metric value as having changed or not. The second category is often referred to as post-classification change detection where a labeled map is compared at two instances and corresponding areas having different labels are then flagged as change areas [14].

When considering land cover change detection, previous studies have shown that multi-temporal change detection methods that infer change based on differences in the surface reflectance at two instances tend to be performance limited due to differences in vegetation [45, 46]. Phenology-induced errors occur when a change map is generated using two images acquired at different stages of the

intra-annual growth cycle [17]. The spectral signature of the same vegetation can vary significantly through the year (Figures 2.10 and 2.11) which could lead to an elevated false alarm rate as the difference in ground reflection between the two acquisitions is not only caused by changes in land cover, but also by a natural seasonal variation in the spectral signature of vegetation. The temporal frequency of the satellite should thus be high enough to distinguish change events from natural seasonal changes in vegetation. Apart from these natural seasonal variations, changes in ecosystems can broadly be classified as being gradual (trend) or abrupt. As the name suggests, gradual change refers to a slow deviation of the time-series caused by, for example, land degradation. Abrupt change refers to an abrupt change in the time-series caused by, for example, deforestation [29]. Therefore, hyper-temporal change detection methods should be able to distinguish phenological cycles from trends or abrupt change in land cover [20, 29, 65]. Another important motivation for using hyper-temporal change detection methods is the need for automated change detection over large areas [66]. While the majority of change detection methods are focused on changes between satellite images from two dates [14, 15], the increasing availability of large archives of historical images makes it possible to develop richer algorithms that fully exploit the temporal dimension of the data. Rather than only focusing on high resolution image to image change detection, it can be complemented by hyper-temporal time-series data. In line with GEOSS philosophy [31], these datasets can be aggregated as a multi-sensor monitoring system and change information obtained using hyper-temporal data could be used to guide high-resolution sensors in acquiring imagery of areas of interest identified using the medium resolution time-series data. Another advantage of hyper-temporal time-series data is that continuous monitoring is possible as the data is not limited to the availability of costly sets of high-resolution images.

Post classification change detection is also not without its challenges. In concept, identifying areas where the class labels are different for two land cover maps is intuitive, but this process relies heavily on the classification accuracy of each of the two land cover maps. The selection of optimal image dates, for example, is crucial since differences in reflectance can be caused by seasonal vegetation fluxes and Sun angle differences which could cause a difference in the the land cover classification for areas that have similar land cover types in both images [14]. For South Africa, two major land cover mapping efforts were made to produce a land cover database in 1994 and 2000, referred to as the South African National Land-Cover (NLC) 94 and NLC 2000 datasets respectively [67]. These datasets were used to determine a change map by comparing the class labels for each pixel. Unfortunately, the 1994 and 2000 versions of the NLC were compiled using very different methods. The NLC 94 had a a minimum mapping unit of 25 ha, and contained 31 land-cover classes whereas the NLC 2000 had a

minimum mapping unit of 2 ha, and contained 45 land-cover classes [67]. Converting these classes into comparable pixel sizes and land cover classes was not a trivial task and taking into consideration that the original classification accuracy of the land cover datasets where 79.4% and 65.8% respectively, the production of a highly accurate land cover change map using this post-classification change detection approach proved challenging [67].

Some of the typical methods used in classical multitemporal change detection, for example image differencing [68–71] , image regression [72], image rationing, vegetation index differencing [73], Principle Component Analysis (PCA) [59, 61] and Change Vector Analysis (CVA) [74], can be adapted to the hyper-temporal case by considering a multitemporal subset of the time-series. For example, in CVA a change vector can be described by an angle of change and a magnitude of change between the reflectance values of multiple bands between two dates. This concept was extended to the hyper-temporal case in [74] by constructing a vector containing a series of biophysical parameter observations within a single year and comparing this vector with the corresponding vector for the following year. The consequent change vector is then analyzed to infer a change or no-change decision. For example, if an NDVI time-series sampled every month is available, a vector containing 12 NDVI values (representing one year) are compared with the corresponding vector for the following year. The idea is that the magnitude and angle of the consequent change vector gives an indication of the change occurring over these consecutive years. The potential problem with this approach, however, is that the change detection is essentially a comparison across multiple instances, comparing two at a time, and does not fully utilize the temporal dimension of the signal.

2.7.1 Hyper-temporal time-series analysis

Time-series analysis comprises of methods that attempt to understand the underlying force structuring the data, identifying patterns and trends, detecting changes, clustering, modeling and forecasting [75]. Because of the high revisit frequency that is required in constructing a hyper-temporal time-series, the data from coarse and medium resolution wide-swath sensors is primarily applicable (section 2.4). In the following section, emphasis will be placed on methods that can be classified as hyper-temporal change detection methods. These methods can be broadly classified into 3 classes namely, regression analysis, Fourier analysis and temporal metrics.

2.7.1.1 Regression Analysis

A fairly common method for change detection using hyper-temporal data is regression analysis. Here, a basic assumption of the underlying form of the data is made, for example a linear trend, and

the parameters of the assumed function is estimated using the observed data. R.E. Kennedy *et al.* considered a set of hypothesized temporal trajectories associated with forest disturbance dynamics [66]. If the time-series fits the idealized trajectory according to a least-squares measure of goodness of fit, it is inferred that the time-series in question experienced the phenomenon described by that trajectory. A similar approach for estimating proportional forest cover change was proposed by D.J. Hayes *et al.* by making use of a regression model and subsequent comparison to reference change data sets derived from Landsat data for a study site in Central America [76]. The advantage of these type of methods is that there is no threshold requirement as a direct classification is made based on the best fit in a finite set of hypothesized temporal trajectories. The disadvantage however is that the performance of methods based on regression analysis depends on the assumption that is made on the form of the hypothesized temporal trajectories. For example, if it is assumed that the temporal trajectory of a hypothesized disturbance will follow the form of a downward step function (i.e. instantaneous drop in reflectance) and the actual temporal trajectory is better described by an exponential decay function, the disturbance in question would not be well represented by the idealized step function. It follows that if the temporal trajectory in question is not well represented by any of the hypothesized trajectories, the change detection method will not perform well. For the method to work in a more general context, a very large dataset of hypothesized trajectories associated with change events will be required as all types of possible changes would have to be characterized, making the approach somewhat impractical for monitoring large heterogeneous areas.

2.7.1.2 Fourier Analysis

Another approach often used when considering hyper-temporal time-series data is Fourier analysis. Fourier analysis expresses a time-series as the sum of a series of cosine waves with varying frequency, amplitude and phase [77]. The frequency of each cosine component is related to the number of completed cycles over the defined interval. The Fast Fourier Transform (FFT) is an effective and computationally efficient algorithm to compute the Discrete Fourier Transform (DFT) [77] and is often used when evaluating satellite time-series data [56–58, 78]. In many applications where the FFT transformation of time-series data is used for classification and segmentation, only the first few FFT components are considered as they tend to dominate the spectrum [56–58]. The reason for this is because of the strong seasonal component and slow variation relative to the sampling interval of the time-series. It has been found that even when considering only the mean and seasonal FFT components [56], reliable class separation can be achieved. A drawback of using FFT-based methods is that the underlying process is assumed to be stationary. This assumption is often invalid in the case of NDVI time-series data, especially if a land cover change is present. Although this method is mostly

used for classification, there has been some recent research interest to use the FFT to perform change detection. For example, B.P. Salmon *et al.* proposed that a sliding window FFT method be used to perform change detection [79]. J. Verbeselt *et.al.* used Fourier analysis as a major step in modeling the seasonal component used in the BFAST (Breaks For Additive Seasonal and Trend) approach [29]. The model used 3 harmonic terms and was found to be more suitable and robust for phenological change detection than the piecewise linear seasonal model using seasonal dummy variables that was employed by the same author in [65].

2.7.1.3   Temporal Metrics

Most of the change detection methods using coarse or medium resolution hyper-temporal time-series are used to detect climate-driven change, phenological modifications and net-primary production on a large scale [16, 17, 19, 80]. J. Borak used temporal change metrics as a land-cover change detection method [16]. These metrics were computed by considering the inter-annual difference of five temporal metrics (annual maximum, annual minimum, annual range, annual mean and temporal vector) as well as two spatial metrics (spatial mean and spatial standard deviation), i.e. $year2 - year1$, for all combinations of the aforementioned spatial and temporal metrics [16]. The underlying idea is that these metrics are compared to a threshold value to determine whether a change or no-change decision should be made. C. Potter used the moving average of the time-series to label pixels as as having changed when the time-series deviated significantly (greater than 1.7 standard deviations) from the 18-year average of the time-series for at least 12 consecutive time-steps [81].

D.J. Mildrexler and N.C Coops used a disturbance index (DI) to detect large-scale ecosystem disturbances [18, 19]. The disturbance index is calculated as:

$$DI_{\mathrm{LST/EVI}} = \frac{LST_{\max}/EVI_{\max}}{LST_{\overline{\mathrm{X}}\max}/EVI_{\overline{\mathrm{X}}\max}}, \tag{2.9}$$

where $DI_{\mathrm{LST/EVI}}$ is the disturbance index, $LST_{\max}$ is the annual maximum land surface temperature, $EVI_{\max}$ is the annual maximum Enhanced Vegetation Index (EVI), $LST_{\overline{\mathrm{X}}\max}$ is the multi-year mean of $LST_{\max}$ and $EVI_{\overline{\mathrm{X}}\max}$ is the multi-year mean of $EVI_{\max}$. From (2.9) it is clear that the disturbance index is calculated on an annual basis. The DI can then be compared to a pre-defined threshold to infer a change or no-change decision.

R.S Lunetta derived a change metric by computing the difference in total annual NDVI for a range of pixels in the given study area and isolating the pixels having an abnormal (relative to the other pixels in the study area) reduction in annual NDVI [17]. The threshold is selected by using standard normal

statistical analysis.

The methods described in [16–18, 81] all work on the principle that when a pixel departs from a normal temporal profile, a change event is detected by comparing the change metric to a threshold value. The change metric that is calculated by the majority of hyper-temporal change detection methods mostly uses an annual composite of the hyper-temporal time-series, for example, the annual NDVI maximum [16], annual maximum land surface temperature [18] or total annual NDVI [17]. Thus, when only the total annual NDVI of a seven-year time-series (sampled every eight days) is used when calculating a change metric, the original time-series, which contains more than 300 samples, is effectively reduced to only 7 samples which decreases the information content of the original time-series considerably. The second consideration is the selection of suitable thresholds. In most of the current hyper-temporal change detection methods in the literature, *a-priori* knowledge of the probability of land-cover change is required when selecting a suitable threshold and more often than not a trial-and-error approach is used in determining these thresholds. In this thesis it is proposed that simulated land cover change be used to determine a suitable threshold. The change metric is calculated for each pixel in a no-change and simulated change dataset and the threshold that best separates the aforementioned datasets is then used. The operator thus only needs to provide examples of no-change time-series, which, unlike change examples is very easy to obtain.

2.7.2   MODIS land cover change products

Although some MODIS change detection products do exist (such as MODIS burn-scar detection [82]), there are currently no operational MODIS products available specifically for land cover change detection. There were however two previous attempts to implement an automated MODIS land cover change product, as an operational system. The first was the MODIS Vegetative Cover Conversion (VCC) product, which uses MODIS 250 m surface reflectance data, and was designed to serve as a global alarm for land cover change caused by anthropogenic activities and extreme natural events [12]. The product was to serve as an alarm which could be augmented by higher resolution sensors such as Landsat 7, Ikonos, and QuickBird once detected. Five change detection methods where proposed [12]:

1. The Red-NIR space partitioning method : Uses a two-dimensional representation of the brightness (mean of band one and two) and greenness (difference between band two and one) at different times to identify change pixels.

2. Red-NIR space change vector: By considering a pixels location in the Red-NIR space at two different dates, the starting and ending positions, direction, and magnitude of the change vector

are used to identify a change event.

3. Modified delta space thresholding: Uses a space defined by differences in pixel values for times 1 and 2 for the red and NIR values of each pixel (no change occurs at the origin). Type of conversion is defined by the angle and distance from the origin and the initial state of the pixel.

4. Texture: Uses the coefficient of variation of the NDVI within a 3×3 kernel at times 1 and 2. When the coefficient of variation exceeds a pre-defined threshold value, a change is flagged.

5. Linear feature: Compute the mean of the absolute difference of the pixel value for each neighboring pixel in a 3×3 kernel. A threshold determines whether a linear feature is present.

The second MODIS land cover change detection product that was proposed was the MODIS Land Cover and Land-Cover Change Algorithm Theoretical Basis Document (ATBD) [83]. The ATBD suggested that the primary change detection technique for the 1 km Land-Cover Change Parameter is change vector analysis [84]. In this technique, a change vector is used to connect two points in multitemporal space. These two points represents an annual multitemporal set of indicator values. The underlying idea is that the change vector is compared to a threshold value, and, when exceeded, a change decision is made. The ATBD also suggested that neural network classifiers be used on a pixel-by-pixel basis to track the probability that a specific pixel changes classes over time. The artificial neural network is used in a supervised manner to develop the Land Cover Parameter. New data that are presented to the neural network is either classified as matching an existing category, or a new category must be created. By monitoring the classification on a per-pixel basis, change can be detected.

When considering the proposed VCC product [12], as well as the change vector analysis method described in the ATBD [84], none of these methods fully utilize the temporal dimension as only two instances are compared rather than considering the complete temporal profile (As discussed in section 2.7.1) and effectively disregards a large suite of time-series methods used in other disciplines e.g. signal processing, telecommunications, etc. The neural network method proposed in the ATBD does show promising results but it should be noted that if a new data presentation does not match an existing category, then it will be necessary to determine whether the new data represent a fundamentally new condition or whether the vigilance parameter needs to be relaxed so that an existing category can now accommodate the new input. This implies that the approach is very sensitive to selection of the vigilance parameter, making the practicality of this approach questionable.

Regardless of the concerns with the proposed MODIS change detection methods, none of these proposed methods were implemented operationally, despite the fact that land cover change detection

was one of the primary objectives of the MODIS sensor [48]. Automated land cover change detection using MODIS data is therefore an ongoing endeavor.

2.8 SUMMARY

In this chapter, the basic principles of electromagnetic radiation were shown together with a description of the properties of the electromagnetic source, which, in the case of optical remote sensing, is the Sun. The interaction of electromagnetic radiation with the atmosphere and land surface was discussed. A brief comparison of sensors showed that there is a trade-off between spatial and temporal resolution. In general, medium-resolution sensors have a much wider swath width compared to high resolution sensors. This implies that when considering a global systematic acquisition strategy, a high resolution image of the same area will be available every couple of months as opposed to the near-daily acquisition of wide swath sensors. This point is crucial as the same area can differ in appearance at different stages of the natural growth seasonal cycle [17]. For this reason, the high temporal frequency provided by medium resolution sensors was opted for. The MODIS sensor was chosen for this thesis, a list of available MODIS products as well the band specifications were given. The MCD43A4 BRDF corrected product was chosen because of the high degree of consistency between images which, in turn, provided accurate surface reflectance time-series information despite large variations in viewing angles. Most change detection methods use multi-temporal data as input and numerous solutions to this class of problem have been presented in the literature. The use of hyper-temporal time-series data for change detection is not as well documented in the literature and most methods that make use of hyper-temporal time-series data for change detection focused on large scale phenological and climate driven changes instead of anthropogenic land cover changes. A novel change detection formulation is thus required when considering change detection for smaller areas that are typically affected by human activities such as new informal settlement developments.

Chapter **THREE**

The Extended Kalman Filter

3.1 INTRODUCTION

As mentioned in chapter 1, one of the change detection methods proposed in this thesis is the Extended Kalman Filter (EKF) change detection method. As the name suggests, the EKF is a critical component of the change detection method and this chapter consequently aims to give some background on conceptual state-space filtering and in particular, the EKF. As will become more apparent in the chapters to follow, the underlying idea of the EKF change detection method lies in modeling an NDVI time-series as a triply modulated cosine function, and tracking the parameters of the model for each time-increment. The state-space filtering method is useful for this specific problem, as the parameters of the triply modulated cosine function could be characterized as a time-variant state-vector which relates to an observation model via the non-linear cosine function. As change detection is our primary objective, the near real-time nature of the state-space filtering method is also particularly useful, as the time from when the change occurred to when change is detected should ideally be minimal.

The EKF framework works on the basis that the posterior density of the state vector given the observed data is always assumed to be Gaussian, which makes for simple implementation and fast execution time [85]. Approximate grid based methods and Gaussian sum filters do not have the limitation of assuming Gaussian posteriors densities, but the computational complexity of these methods are very high which prevents their widespread use in practice [85]. The broader objective of this study is to implement the change detection methods operationally. This requires that the specific non-linear state space filter that is chosen be well understood and lend itself to be easily implemented. The EKF was consequently chosen as it is a well established method which is easily implementable [85]. The EKF was also compared to a sliding window FFT approach (section 4.5) and was found to be superior for the specific problem presented in this thesis (see chapter 6).

3.2   CONCEPTUAL STATE-SPACE FILTERING SOLUTION

In many applications, it is necessary to estimate the state of a dynamic system using only a time-series of noisy-measurements made on the system. In many cases, a discrete-time state-space approach is used to model the dynamic system. The underlying idea is that difference equations are used to model the evolution of the system over time and that measurements are available at discrete times. It is assumed that the state vector of the system contains a vector of state parameters that are able to accurately describe the behavior of a system. For example, in tracking systems, these parameters can be related to the kinematic characteristics of the target [85].

Using the state-space approach, at least two models are required to describe the noisy measurements obtained from the dynamic system. The first model (process model) describes the evolution of each state parameter from time-step $k - 1$ to k. The second model (observation model) takes as input the state parameters at time-step k, obtained during the previous step, to produce an estimate of the output of the system at time-step k. For many applications, an estimate of the state parameters is required every time a measurement is received. The recursive nature of the state-space approach implies that a recursive filtering approach can be used where received data can be processed sequentially. Such a filter consists of two stages, namely predict and update. In the predict stage, the state PDF is predicted forward from one time-step to the next, which effectively broadens the state PDF. In the update stage, the latest available measurement is used to tighten the state PDF. [85]

The two models can be described formally as

$$\mathbf{x}_k = \mathbf{f}(\mathbf{x}_{k-1}) + \mathbf{w}_{k-1}, \tag{3.1}$$

and

$$\mathbf{y}_k = \mathbf{h}(\mathbf{x}_k) + \mathbf{v}_k. \tag{3.2}$$

Where $\mathbf{x}_k$ is the state vector at time-step k in the form

$$\mathbf{x}_k = [x_{k,1} \ x_{k,2} \ x_{k,3} \ ... \ x_{k,s}], \tag{3.3}$$

with s being the total number of state parameters. The relation between $\mathbf{x}_k$ and $\mathbf{x}_{k-1}$ is given by $\mathbf{f}$, a known but possibly non-linear function. The state vector $\mathbf{x}_k$ is related to the observation vector $\mathbf{y}_k$ via a known but possibly non-linear measurement function $\mathbf{h}$ It should be noted that $\mathbf{f}$ and $\mathbf{h}$ are allowed to be time-variant, but the time-invariant assumption was assumed in this thesis.. Both these models

are possibly non-perfect, so the addition of process $\mathbf{w}_{k-1}$ and measurement $\mathbf{v}_k$ noise is included.

The task at hand is to produce an estimate of $\mathbf{x}_k$ given all available measurements $\mathbf{Y}_k = \{\mathbf{y}_1, \mathbf{y}_2, \mathbf{y}_3, ..., \mathbf{y}_k\}$ up to time k. It is thus required to construct the posterior PDF $p(\mathbf{x}_k|\mathbf{Y}_k)$. The initial estimate of $p(\mathbf{x}_k)$ should be provided where-after $p(\mathbf{x}_k|\mathbf{Y}_k)$ is estimated recursively using the predict and update stages mentioned previously. The predicted PDF $p(\mathbf{x}_k|\mathbf{Y}_{k-1})$ is obtained by means of the Chapman-Kolmogoroff equation [85]:

$$p(\mathbf{x}_k|\mathbf{Y}_{k-1}) = \int p(\mathbf{x}_k|\mathbf{x}_{k-1})p(\mathbf{x}_{k-1}|\mathbf{Y}_{k-1})d\mathbf{x}_{k-1}. \tag{3.4}$$

Where $p(\mathbf{x}_k|\mathbf{x}_{k-1})$ is obtained using (3.1) and known statistics of $\mathbf{w}_{k-1}$. When the observation at time k ($\mathbf{y}_k$) becomes available, the state PDF is updated via Bayes' rule:

$$p(\mathbf{x}_k|\mathbf{Y}_k) = \frac{p(\mathbf{y}_k|\mathbf{x}_k)p(\mathbf{x}_k|\mathbf{Y}_{k-1})}{p(\mathbf{y}_k|\mathbf{Y}_{k-1})}, \tag{3.5}$$

where the normalization constant $p(\mathbf{y}_k|\mathbf{Y}_{k-1})$ can be written as

$$p(\mathbf{y}_k|\mathbf{Y}_{k-1}) = \int p(\mathbf{y}_k|\mathbf{x}_k)p(\mathbf{x}_k|\mathbf{Y}_{k-1})d\mathbf{x}_k. \tag{3.6}$$

The likelihood $p(\mathbf{y}_k|\mathbf{x}_k)$ can be obtained by using (3.2) and known statistics of $\mathbf{v}_k$. Knowledge of the posterior density $p(\mathbf{x}_k|\mathbf{Y}_k)$ enables one to not only compute the optimal state estimate with respect to any criterion, but also to determine the measure of accuracy of the state estimate [85]. For example, if $p(\mathbf{x}_k|\mathbf{Y}_k)$ is a multivariate Gaussian distribution, the covariance matrix can be used to determine the state estimate accuracy.

In the case that $\mathbf{w}_{k-1}$ and $\mathbf{v}_k$ in (3.1) and (3.2) are Gaussian distributed and both $\mathbf{f}(\mathbf{x}_{k-1})$ and $\mathbf{h}(\mathbf{x}_k)$ are linear functions, the functional recursion of (3.4) and (3.5) is the Kalman filter [86]. The Kalman filter will be discussed in further detail in the following section.

3.3 KALMAN FILTER

The Kalman filter is named after Rudolf E. Kalman and is a well-established method that was published in 1960 [86]. Since the algorithm was proposed, it has been widely used, especially in military and space applications.

As stated previously, the Kalman filter assumes that the process and observation noise is Gaussian distributed and that both the $\mathbf{f}$ and $\mathbf{h}$ functions in (3.1) and (3.2) are linear. It follows that (3.1) and (3.2) can be written as:

$$\mathbf{x}_k = \mathbf{F}\mathbf{x}_{k-1} + \mathbf{w}_{k-1}, \tag{3.7}$$

and

$$\mathbf{y}_k = \mathbf{H}\mathbf{x}_k + \mathbf{v}_k, \tag{3.8}$$

where $\mathbf{F}$ and $\mathbf{H}$ are known matrices defining the linear functions [85]. It is assumed that $\mathbf{w}_{k-1}$ and $\mathbf{v}_k$ are zero-mean Gaussian distributed with covariances $\mathbf{Q}_{k-1}$ and $\mathbf{R}_k$ respectively. The distributions $p(\mathbf{x}_{k-1}|\mathbf{Y}_{k-1})$, $p(\mathbf{x}_k|\mathbf{Y}_{k-1})$ and $p(\mathbf{x}_k|\mathbf{Y}_k)$ given in equations (3.4) and (3.5) can then be expressed as:

$$p(\mathbf{x}_{k-1}|\mathbf{Y}_{k-1}) = \mathcal{N}(\mathbf{x}_{k-1}; \widehat{\mathbf{x}}_{k-1|k-1}, \mathbf{P}_{k-1|k-1}) \tag{3.9}$$

$$p(\mathbf{x}_k|\mathbf{Y}_{k-1}) = \mathcal{N}(\mathbf{x}_k; \widehat{\mathbf{x}}_{k|k-1}, \mathbf{P}_{k|k-1}) \tag{3.10}$$

$$p(\mathbf{x}_k|\mathbf{Y}_k) = \mathcal{N}(\mathbf{x}_k; \widehat{\mathbf{x}}_{k|k}, \mathbf{P}_{k|k}), \tag{3.11}$$

where $\mathcal{N}(\mathbf{x}; \mathbf{m}, \mathbf{P})$ is a Gaussian distribution with argument $\mathbf{x}$, mean $(\mathbf{m})$ and covariance $(\mathbf{P})$ given as:

$$\mathcal{N}(\mathbf{x}; \mathbf{m}, \mathbf{P}) = \sqrt{|2\pi\mathbf{P}|} \, e^{-\frac{1}{2}(\mathbf{x}-\mathbf{m})^T \mathbf{P}^{-1}(\mathbf{x}-\mathbf{m})}. \tag{3.12}$$

The mean and covariance parameters in (3.9)-(3.11) is given as [86]:

$$\widehat{\mathbf{x}}_{k|k-1} = \mathbf{F}\,\widehat{\mathbf{x}}_{k-1|k-1} \tag{3.13}$$

$$\mathbf{P}_{k|k-1} = \mathbf{Q}_{k-1} + \mathbf{F}\,\mathbf{P}_{k-1|k-1}\mathbf{F}^T \tag{3.14}$$

$$\widehat{\mathbf{x}}_{k|k} = \widehat{\mathbf{x}}_{k|k-1} + \mathbf{K}_k(\mathbf{y}_k - \mathbf{H}\widehat{\mathbf{x}}_{k|k-1}) \tag{3.15}$$

$$\mathbf{P}_{k|k} = \mathbf{P}_{k|k-1} - \mathbf{K}_k\mathbf{S}_k\mathbf{K}_k^T, \tag{3.16}$$

where

$$\mathbf{S}_k = \mathbf{H}\mathbf{P}_{k|k-1}\mathbf{H}^T + \mathbf{R}_\mathbf{k}, \tag{3.17}$$

is the innovation term and

$$\mathbf{K}_k = \mathbf{P}_{k|k-1}\mathbf{H}^T\mathbf{S}_k^{-1}, \tag{3.18}$$

is the Kalman gain. The Kalman filter thus effectively computes the mean and covariance of the Gaussian posterior $p(\mathbf{x}_k|\mathbf{Y}_k)$ and is optimal in the linear Gaussian environment. Unfortunately, many

real world applications are non-linear and quite often non-stationary. In this case, approximation methods have to be used. A popular extension of the Kalman filter to the non-linear case is the Extended Kalman Filter, which will be discussed in more detail in the following section.

3.4   EXTENDED KALMAN FILTER

The extended Kalman filter (EKF) is the nonlinear version of the popular Kalman filter. Similar to the standard Kalman filter, for every increment of k (the discrete time) a state vector $\mathbf{x}_k$ is defined containing the parameters to be estimated. If one were, for example, to estimate the mean (μ) amplitude (α) and phase (ϕ) of a cosine function, the state vector could be in the form $\mathbf{x}_k = [\mu_k \ \alpha_k \ \phi_k]^T$. The state vector can be estimated over time k by recursive iteration based on the observation data $\mathbf{Y}_k$ up to time k. For the EKF, equations (3.7) and (3.8) can be reformulated as:

$$\mathbf{x}_k = \mathbf{f}(\mathbf{x}_{k-1}) + \mathbf{w}_{k-1}, \tag{3.19}$$

and

$$\mathbf{y}_k = \mathbf{h}(\mathbf{x}_k) + \mathbf{v}_k. \tag{3.20}$$

In this formulation, either or both functions $\mathbf{f}$ and $\mathbf{h}$ are non-linear functions. The basic idea is that these non-linear functions can be sufficiently described using local linearization. The posterior PDF $p(\mathbf{x}_k|\mathbf{Y}_k)$ is approximated by a Gaussian distribution which implies that (3.9)-(3.11) are assumed to hold. Equations (3.13)-(3.18) can then be rewritten as:

$$\widehat{\mathbf{x}}_{k|k-1} = \mathbf{f}(\widehat{\mathbf{x}}_{k-1|k-1}) \tag{3.21}$$

$$\mathbf{P}_{k|k-1} = \mathbf{Q}_{k-1} + \mathbf{F}\,\mathbf{P}_{k-1|k-1}\mathbf{F}^T \tag{3.22}$$

$$\widehat{\mathbf{x}}_{k|k} = \widehat{\mathbf{x}}_{k|k-1} + \mathbf{K}_k(\mathbf{y}_k - \mathbf{h}(\widehat{\mathbf{x}}_{k|k-1})) \tag{3.23}$$

$$\mathbf{P}_{k|k} = \mathbf{P}_{k|k-1} - \mathbf{K}_k\mathbf{S}_k\mathbf{K}_k^T, \tag{3.24}$$

where

$$\mathbf{S}_k = \mathbf{H}_k\mathbf{P}_{k|k-1}\mathbf{H}_k^T + \mathbf{R_k} \tag{3.25}$$

$$\mathbf{K}_k = \mathbf{P}_{k|k-1}\mathbf{H}_k^T\mathbf{S}_k^{-1}, \tag{3.26}$$

and $\mathbf{F}$ and $\mathbf{H}$ are the local linearization of the non-linear function $\mathbf{f}$ and $\mathbf{h}$ respectively. They are defined as Jacobians evaluated at $\widehat{\mathbf{x}}_{k-1|k-1}$ and $\widehat{\mathbf{x}}_{k|k-1}$ respectively [85]:

$$\widehat{\mathbf{F}} = \|\nabla_{\mathbf{x_{k-1}}} \mathbf{f}^T(\mathbf{x_{k-1}})^T\|_{\mathbf{x_{k-1}}=\widehat{\mathbf{x}}_{k-1|k-1}} \tag{3.27}$$

$$\widehat{\mathbf{H}} = \|\nabla_{\mathbf{x_k}} \mathbf{h}^T(\mathbf{x_k})^T\|_{\mathbf{x_k}=\widehat{\mathbf{x}}_{k|k-1}}, \tag{3.28}$$

where

$$\nabla_{\mathbf{x_k}} = \left[\frac{\partial}{\partial x_{k,1}} \cdots \frac{\partial}{\partial x_{k,s}}\right]. \tag{3.29}$$

The EKF is referred to as an analytical approximation because the Jacobians $\widehat{\mathbf{F}}$ and $\widehat{\mathbf{H}}$ are computed analytically.

3.5 EXAMPLE OF AN EKF TRACKING APPLICATION

In this section, an example of tracking a cosine function with varying amplitude and phase using an EKF is shown. Assume that noisy observations are made of a process that is governed by the following function:

$$y_k = \alpha \cos(\omega k + \phi) + n_k, \tag{3.30}$$

where $\omega = 2\pi f$. It is assumed that the fundamental frequency f is known and that the task at hand is to estimate the value of α and ϕ for each time-step k given observations up to time-step k. It is proposed that this non-linear problem be solved using an EKF. The state vector can be defined as:

$$\mathbf{x_k} = [\alpha_k \ \phi_k]^T. \tag{3.31}$$

The process and observation models can be formulated as:

$$\mathbf{x_k} = \mathbf{x_{k-1}} + \mathbf{w_{k-1}}, \tag{3.32}$$

and

$$y_k = h(\mathbf{x}_k) + v_k, \tag{3.33}$$

where $h(\mathbf{x}_k) = x_{k,1}\cos(\omega k + x_{k,2})$. In the process model (3.32), it is assumed that the state vector remains constant from one time-step to the next with an additive process noise component. This implies that:

$$\mathbf{f}(\mathbf{x}) = \mathbf{F}\mathbf{x} = \mathbf{I}\mathbf{x}, \tag{3.34}$$

where $\mathbf{I}$ is a 2×2 Identity matrix. It is assumed that the noise component $\mathbf{w_{k-1}}$ is Gaussian distributed having zero mean and covariance $\mathbf{Q_{k-1}}$, i.e. $p(\mathbf{w_{k-1}}) = \mathcal{N}([0\ 0]^T, \mathbf{Q_{k-1}})$

The observation model (3.33) is based on (3.30) with the amplitude and phase parameter being replaced by the state parameters representing each of these variables and the noise component v_k also being assumed to be Gaussian distributed with zero mean and variance $\mathbf{R_k} = \sigma_v^2$, i.e. $p(\mathbf{v_k}) = \mathcal{N}(0, \sigma_v^2)$.

The state parameter $(\widehat{\mathbf{x}}_{k|k-1})$ prediction given in (3.21), can be re-written for this specific problem as:

$$
\begin{align}
\widehat{\mathbf{x}}_{k|k-1} &= \mathbf{f}(\widehat{\mathbf{x}}_{k-1|k-1}) \tag{3.35} \\
&= \mathbf{I}\mathbf{x}_{k-1|k-1} \tag{3.36} \\
&= \mathbf{x}_{k-1|k-1}. \tag{3.37}
\end{align}
$$

The predicted covariance term $(\mathbf{P}_{k|k-1})$, as calculated in (3.22) can also be re-written as:

$$
\begin{align}
\mathbf{P}_{k|k-1} &= \mathbf{Q}_{k-1} + \mathbf{F}\,\mathbf{P}_{k-1|k-1}\mathbf{F}^T \tag{3.38} \\
&= \mathbf{Q}_{k-1} + \mathbf{I}\,\mathbf{P}_{k-1|k-1}\mathbf{I}^T \tag{3.39} \\
&= \mathbf{Q}_{k-1} + \mathbf{P}_{k-1|k-1}. \tag{3.40}
\end{align}
$$

In the state vector update phase of the EKF (3.23), the observation $(\mathbf{y}_k)$ is used to update the current state vector $\widehat{\mathbf{x}}_{k|k-1}$ and can be written as:

$$
\begin{align}
\widehat{\mathbf{x}}_{k|k} &= \widehat{\mathbf{x}}_{k|k-1} + \mathbf{K}_k(\mathbf{y}_k - \mathbf{h}(\widehat{\mathbf{x}}_{k|k-1})) \tag{3.41} \\
&= \widehat{\mathbf{x}}_{k|k-1} + \mathbf{K}_k(\mathbf{y}_k - \widehat{\mathbf{H}}\widehat{\mathbf{x}}_{k|k-1}), \tag{3.42}
\end{align}
$$

where $\widehat{\mathbf{H}}$ is the local linearization of function $\mathbf{h}(\mathbf{x})$ given as:

$$
\begin{align}
\widehat{\mathbf{H}} &= \| \nabla_{\mathbf{x}_k} h(\mathbf{x}_k)\|_{\mathbf{x}_k=\widehat{\mathbf{x}}_{k|k-1}} \tag{3.43} \\
&= \left[\frac{\partial}{\partial x_{k,1}}h(\mathbf{x}_k) \quad \frac{\partial}{\partial x_{k,2}}h(\mathbf{x}_k)\right]_{\mathbf{x}_k=\widehat{\mathbf{x}}_{k|k-1}}, \tag{3.44}
\end{align}
$$

where

$$
\begin{align}
\frac{\partial}{\partial x_{k,1}}h(\mathbf{x}_k) &= \frac{\partial}{\partial x_{k,1}}\,x_{k,1}\cos(\omega k + x_{k,2}) \tag{3.45} \\
&= \cos(\omega k + x_{k,2}), \tag{3.46}
\end{align}
$$

and

$$\frac{\partial}{\partial x_{k,2}} h(\mathbf{x}_k) = \frac{\partial}{\partial x_{k,2}} x_{k,1} \cos(\omega k + x_{k,2}) \tag{3.47}$$

$$= \frac{\partial}{\partial x_{k,2}} x_{k,1} \left[\cos(\omega k) \cos(x_{k,2}) - \sin(\omega k) \sin(x_{k,2}) \right] \tag{3.48}$$

$$= -x_{k,1} \left[\sin(\omega k) \cos(x_{k,2}) + \cos(\omega k) \sin(x_{k,2}) \right]. \tag{3.49}$$

The term $\mathbf{S}_k$ in the parameter covariance update equation (3.24) can also be rewritten for the present case as:

$$\mathbf{S}_k = \mathbf{H}_k \mathbf{P}_{k|k-1} \mathbf{H}_k^T + \mathbf{R}_k \tag{3.50}$$

$$= \widehat{\mathbf{H}}_k \mathbf{P}_{k|k-1} \widehat{\mathbf{H}}_k^T + \sigma_v^2. \tag{3.51}$$

A time-series was generated with a Signal-to-noise Ratio (SNR) of 5 dB (Figure 3.1A). Figures 3.1B and 3.1C show the corresponding amplitude and phase being tracked using the EKF framework. In Figure 3.1A, the noisy observations as well as the actual signal is shown together with the filtered EKF estimate. It can be seen that the filter requires an initial number of observations before the EKF state parameters start to stabilize. The stabilized state vector corresponds to the accurate tracking of the underlying signal by the EKF, i.e. as soon as the state parameters start to stabilize, the value of the underlying signal is very accurately tracked by the EKF.
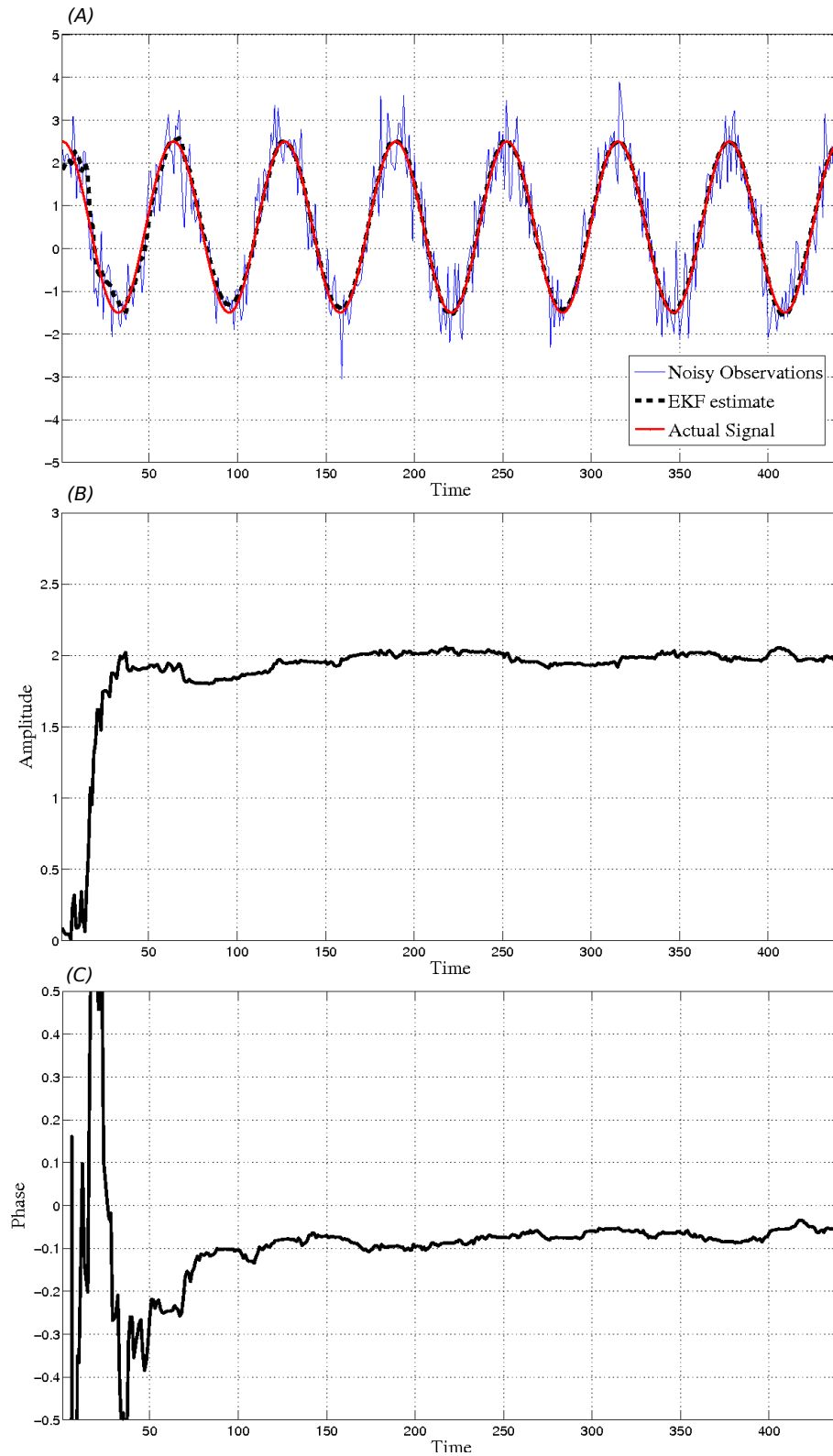
FIGURE 3.1: Figure *A* shows the noisy observation, actual signal and EKF output. Figures *B* and *C* show the estimated amplitude and phase state parameter for each time-step.

CHAPTER FOUR

IMPROVING LAND-COVER SEPARABILITY USING AN EXTENDED KALMAN FILTER

As stated in chapter 1, the main objective of this thesis is to develop an automated land cover change detection method. The EKF change detection methodology that is proposed in this thesis is based on the assumption that the parameters of the underlying EKF model (which will be discussed in detail in the following sections) is separable for the two classes involved in the land cover transition, which for the present case is natural vegetation and settlement. It follows that the more separable the EKF derived parameters are for natural vegetation and settlement classes, the easier it would be to detect when this type of land-cover transition occurs. In this chapter, the focus will be on evaluating the land-cover separability of the proposed method.

A recent method proposed in [56] shows that features estimated using Fourier analysis on NDVI signals provide very good land-cover class separability. The method proposed in this chapter extends on the method in [56] by modeling an NDVI time-series (section 2.6) as a triply modulated cosine function and updates the mean (μ) amplitude (α) and phase (ϕ) parameters of the model for each iteration by means of an EKF (section 3.4). These parameters are then used to separate natural vegetation and settlement time-series more effectively. Another competitor, the sliding window FFT method, which is an extension proposed by the author to the method presented in [56] is also evaluated and the performance of the EKF method is compared to that of the aforementioned methods as validation of the increased land cover separability achievable using the proposed EKF formulation. The following chapter will show how the parameters, which will be shown to be adequately separable for the land cover classes considered in this study, can be used in a spatio-temporal context for land-cover change detection.

4.1 INTRODUCTION

Land-cover classification based on multi-temporal satellite data can capitalize on seasonal variation in land surface reflectance due to vegetation phenology to provide better classification than single-date imagery [15, 87]. Multi-temporal coarse resolution satellite imagery such as MODIS and AVHRR have been widely used to map land-cover at regional to global scales [88–90]. Land-cover classification methods are often based on a series of secondary metrics derived from the NDVI time-series (section 2.6) and include Principal Component Analysis (PCA) [87, 91, 92], phenological metrics [93] or Fourier (spectral) analysis [56, 94].

Fourier (spectral) analysis expresses a time-series as the sum of a series of sinusoidal waves with varying frequency, amplitude and phase [77]. The frequency of each sinusoidal component is related to the number of completed cycles over the defined interval. The Fast Fourier Transform (FFT) is an effective and computationally efficient algorithm to compute the Discrete Fourier Transform (DFT) [77] and is often used when evaluating NDVI time-series data [56–58, 78].

In many applications where the FFT transformation of NDVI time-series data are used for classification and segmentation, only the first few FFT components are considered as they tend to dominate the spectrum [56–58]. The reason for this is because of the strong seasonal component and slow variation relative to the sampling interval of the time-series (8 days for the MODIS MCD43 product). It has been found that even when considering only the mean and seasonal FFT components [56], reliable class separation can be achieved. A drawback of using FFT-based methods is that the underlying process is assumed to be stationary. This assumption is often invalid in the case of NDVI time-series data, especially if a land-cover change is present.

The EKF is a non-linear estimation method that can potentially be employed to estimate unobserved parameters (process model) using noisy observations of a related measurement model (Section 3.4). EKF techniques in remote sensing have been used for parameter estimation of values related to physical, biogeochemical processes or vegetation dynamics models [95, 96].

In this chapter an FFT approach will firstly be shown that separates different land-cover types based on their FFT mean and annual components [56]. A novel method is then proposed that models the NDVI time-series as a triply modulated cosine function. An EKF is used to track the parameters of the mean (μ), amplitude (α) and the phase (ϕ) parameters of the proposed model for each time-step.
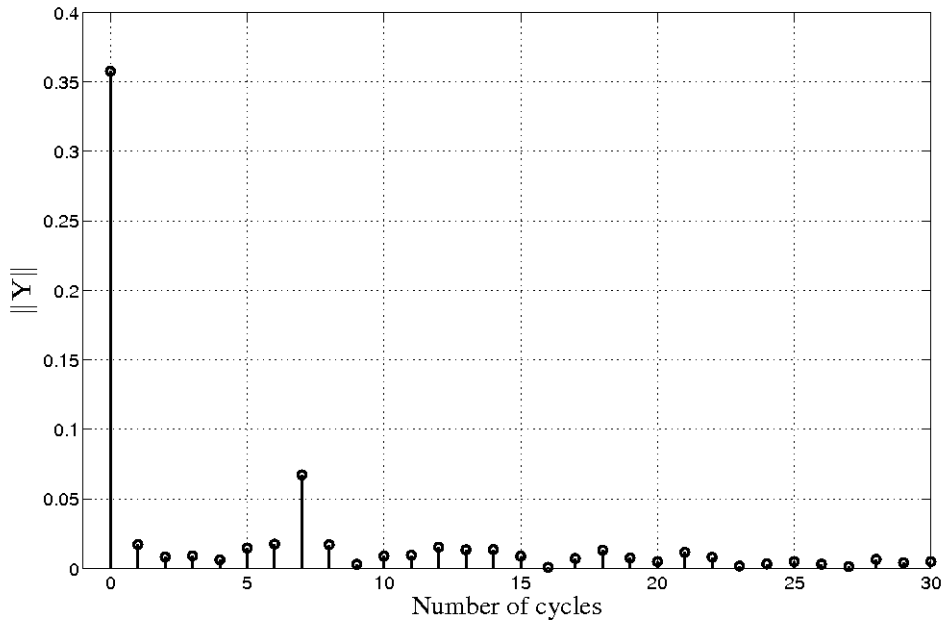
FIGURE 4.1: Magnitude of the first 30 FFT components of a typical natural vegetation NDVI series.

The objective is to show that using MODIS MOD43 data (Section 2.5), the μ, α, and ϕ parameter sequences over time are similar for same class land-cover types and dissimilar for different land-cover types representing natural vegetation and settlement land-cover types in northern South Africa.

4.2   LAND-COVER CLASS SEPARATION USING THE FFT

As discussed in section 4.1, the Fourier analysis of the NDVI time-series has proved to be insightful because the signal can be decomposed into a series of cosine waves with varying amplitude, phase and frequency. The DFT can be written in matrix form as:

$$\mathbf{Y} = \mathbf{F}_N \mathbf{y}, \tag{4.1}$$

where $\mathbf{y}^T = [y_0 \; y_1 \; y_2 \; ... \; y_{N-1}]$ is the NDVI time-series of length N in vector form. $\mathbf{Y}^T = [Y_0 \; Y_1 \; Y_2 \; ... \; Y_{N-1}]$ is the DFT of $\mathbf{y}$ and $\mathbf{F}_N$ is the DFT matrix in the form:

$$\mathbf{F}_N(r, c) = \left[\frac{1}{\sqrt{N}} \, e^{\frac{-2\pi i}{N}} \right]^{(r-1)\cdot(c-1)}, \tag{4.2}$$

where $\mathbf{F}_N(r, c)$ is the value of row r and column c of the $\mathbf{F}_N$ matrix [77]. The first 30 FFT components of a typical seven-year natural vegetation NDVI time-series is shown in Figure 4.1.

As expected, the majority of signal energy is contained in the mean and the annual component which relates to FFT component zero and seven respectively when considering a seven-year time-series. As proposed in [56], the similarity of any two arbitrary NDVI time-series can be evaluated by computing their FFT transformation respectively and then comparing the first and seasonal FFT component of each FFT series. A distance metric based on the mean (μ) and seasonal (α) FFT component difference for any two FFT series can then be formulated as follows:

$$D_\mu = \|Y_0^1 - Y_0^2\|, \tag{4.3}$$

and

$$D_\alpha = \|2(Y_7^1 - Y_7^2)\|, \tag{4.4}$$

where D_μ and D_α are the Euclidean distance between the mean and annual FFT components respectively of two NDVI time-series.

4.3   TRIPLY MODULATED COSINE MODEL

It can be seen from Figure 4.1 that the majority of the signal energy is contained in the mean and annual FFT component. This implies that the signal is well represented in the time-domain as a single cosine function with a specific mean offset, amplitude and phase, as shown in Figure 4.2. This single cosine model is, however, not a very good representation when the time-series is non-stationary, which is often the case because of, for example, inter annual variability or land-cover change. It is proposed that an NDVI time-series for a given pixel be modeled using a triply modulated cosine function given as

$$y_k = \mu_k + \alpha_k \cos(\omega k + \phi_k) + v_k, \tag{4.5}$$

where y_k denotes the observed value of the NDVI time-series at time k and v_k is the noise sample at time k. The noise is additive but with an unknown distribution. The cosine function is based on a number of parameters (that are not directly observable), namely the frequency ω, the nonzero mean μ, the amplitude α and the phase ϕ. The frequency can be explicitly computed as $\omega = 2\pi f$ where f is based on the annual vegetation growth cycle. Given the 8 daily composite MCD43 MODIS data, f was calculated to be 8/365. The values of μ_k, α_k and ϕ_k are functions of time and must be estimated given y_k for $k \in 1, \ldots, N$, where N is the total number of observations. The estimation of these parameters is non-trivial and require a non-linear estimator. The estimator that was used in this thesis is an EKF.
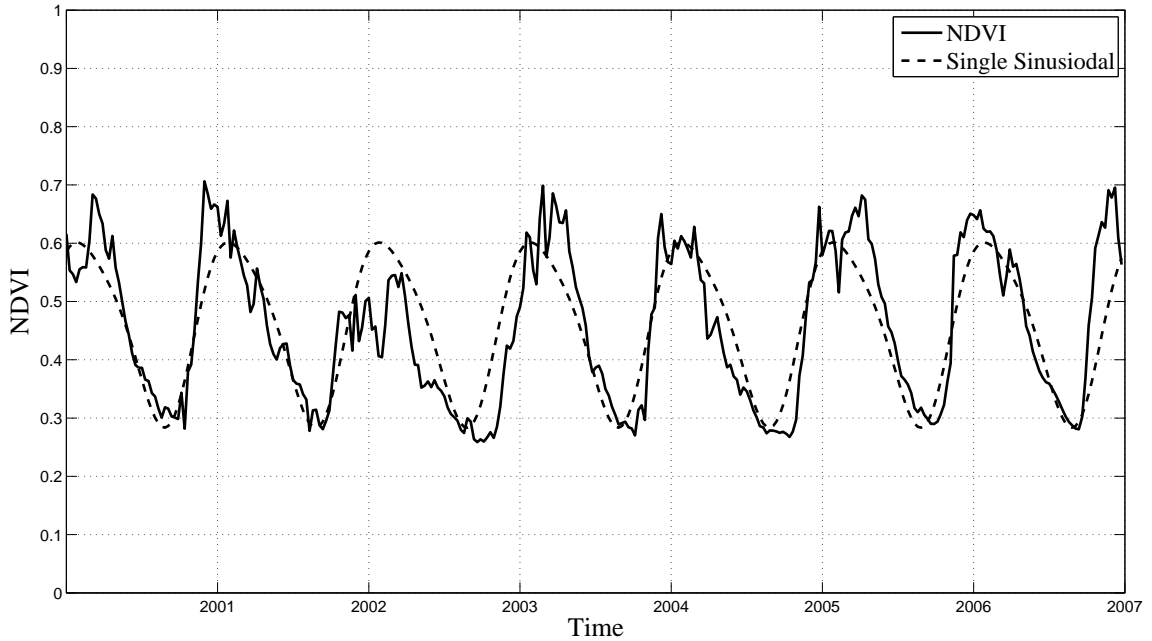
FIGURE 4.2: Typical natural vegetation NDVI time-series modeled by a single sinusoidal function with fixed mean offset, amplitude and phase.

4.4   NEW CLASS SIMILARITY METRIC

As shown in [56], substantial separability can be achieved when comparing mean and annual FFT components of NDVI time-series of different land-cover types. The underlying idea in [56] is that a similarity index can be calculated by considering the mean and annual FFT components of two pixel's time-series. It is proposed that instead of taking a single FFT of the entire seven-year time-series and considering a scalar mean and amplitude value, the estimated values for μ_k, α_k and ϕ_k as presented in (4.5) be estimated for each value of k using an EKF. The state vector is defined as:

$$\mathbf{x}_k = \begin{bmatrix} \mu_k \ \alpha_k \ \phi_k \end{bmatrix}^T. \tag{4.6}$$

and the process and observation models are formulated as:

$$\mathbf{x}_k = \mathbf{x}_{k-1} + \mathbf{w}_{k-1}, \tag{4.7}$$

and

$$y_k = x_{k,1} + x_{k,2} \cos(2\pi f k + x_{k,3}) + n_k. \tag{4.8}$$

The process model assumes that the state vector remains constant from one time-step to the next
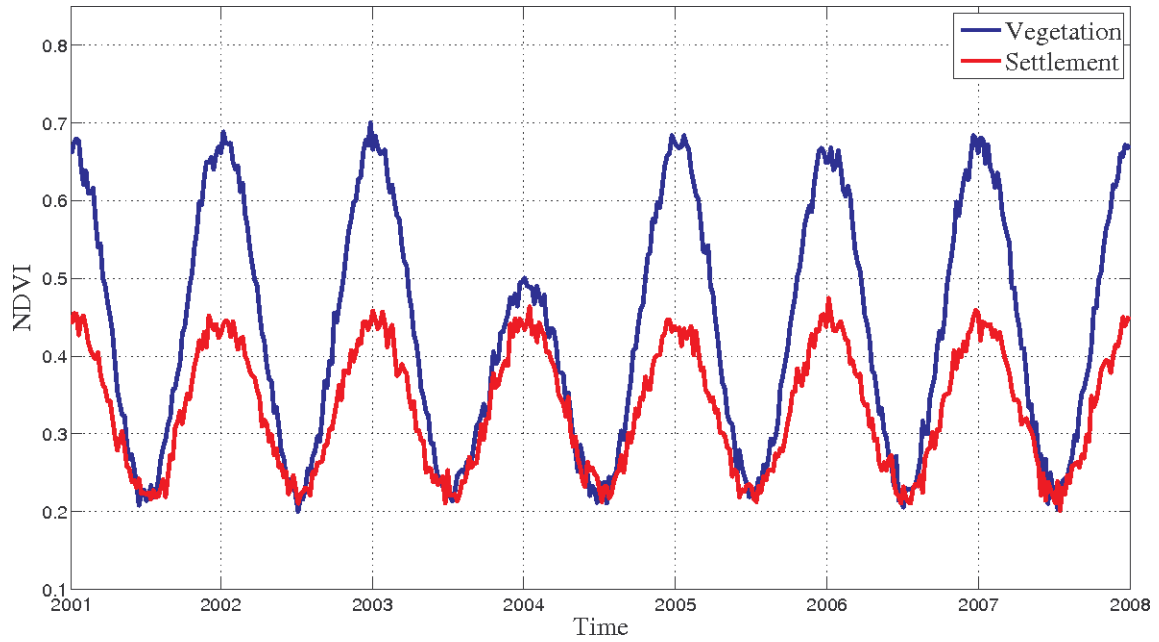
FIGURE 4.3: Natural vegetation and settlement time-series.

with an additive process noise component. The observation model is based on (4.5) with the mean, amplitude and phase parameter being replaced by the state parameters representing each of these variables. Having an estimate of each of the state parameters for each time-step k effectively results in a time-series for each of the three parameters, the advantage of which will become apparent when considering the following example.

Consider the seven-year natural vegetation and settlement NDVI time-series shown in Figure 4.3. As expected, the NDVI for the natural vegetation time-series shows a much higher peak in the summer time due to the increased biomass compared to a typical settlement time-series. The low peak in the NDVI for the vegetation time-series in the summer of 2004 is attributed to a very dry season leading to a reduction in biomass. Using the methodology shown in section 4.2, a similarity metric can be computed by comparing the FFT components of each of these NDVI time-series. In particular, the mean and annual FFT components are compared (Section 4.2). The annual FFT components of both the natural vegetation and settlement NDVI time-series are shown in Figure 4.4. When considering the natural vegetation annual FFT component, it can be seen that the non-stationarity due to the dry year reduces the natural vegetation annual FFT component which effectively reduces the separability between the two time-series.

On the other hand, when tracking the vegetation amplitude using an EKF, it can be seen that an accurate estimate of the amplitude is produced for each time-step (Figure 4.3). The separability between the
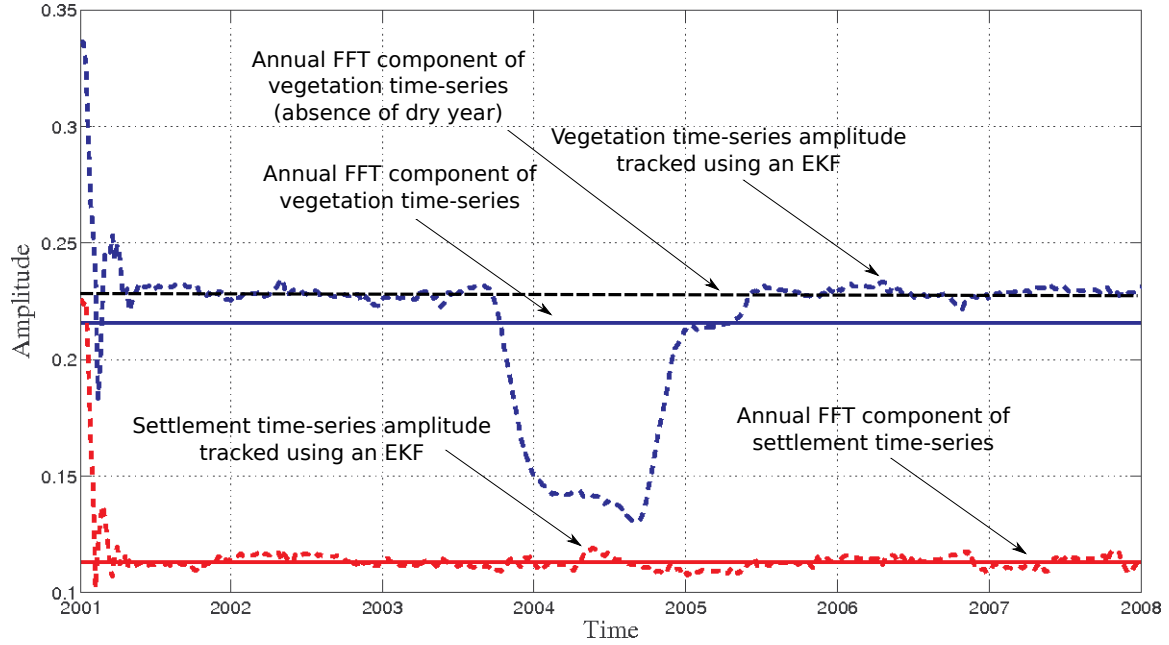
FIGURE 4.4: FFT annual component as well as EKF tracked amplitude of the vegetation and settlement time-series given in Figure 4.3.

natural vegetation and settlement amplitude (tracked using the EKF framework) remains at a maximum when considering the years that are unaffected by the dry year. It is thus proposed that a distance metric describing the similarity between the two time-series be formulated by taking the maximum distance between the EKF derived parameter streams of the time-series given as

$$D_\mu = \max\{\mu_{k,1} - \mu_{k,2}\}, \quad 1 \leq k \leq N, \tag{4.9}$$

and

$$D_\alpha = \max\{\alpha_{k,1} - \alpha_{k,2}\}, \quad 1 \leq k \leq N. \tag{4.10}$$

D_μ is the maximum distance between the first (μ_1) and second (μ_2) parameter sequence over time k. D_α is calculated in a similar manner finding the maximum distance between the amplitude parameter sequences.

4.5 SLIDING WINDOW FFT APPROACH

From figure 4.4 it is clear that the EKF produces a time-series for the mean and amplitude parameter where the comparative mean and annual component of the FFT method produces a single frequency domain estimate. A more "fair" comparison would be to use a sliding window FFT to estimate the mean and annual component for a sliding-window by keeping the window-size constant and incrementing the start and endpoints of the window by one time-step. The underlying idea is that the FFT is calculated
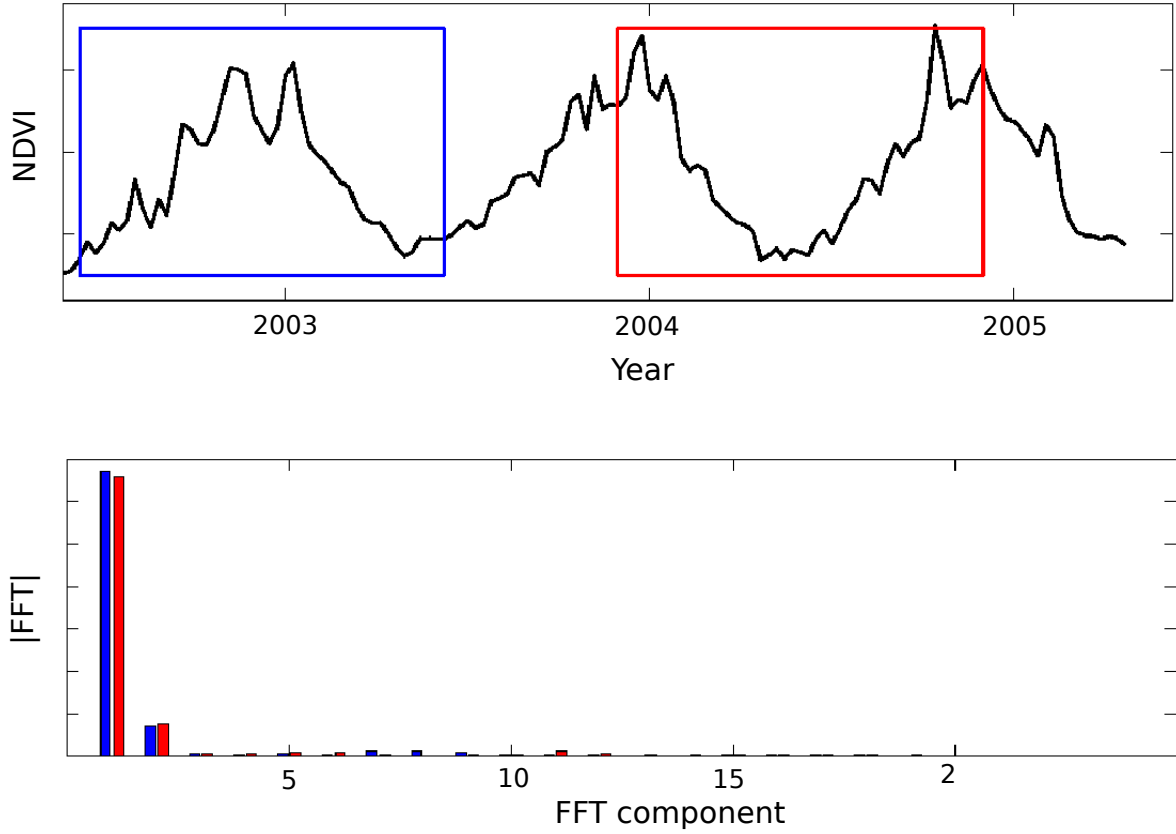
FIGURE 4.5: Two instances of a one year sliding window together with their corresponding FFT.

over each time-series window and that that mean and annual component is then recorded for each increment. As the window slides over the time-series, the mean and annual component can each be expressed as a time-series. The first FFT component is related to the mean of the time-series, the FFT component that corresponds to the annual components can be calculated as

$$C_a = L/P + 1. \tag{4.11}$$

Where L is the window size and P is the number of time-series samples in one year. For this study, it is assumed that L will always be a multiple of P. Figure 4.5 illustrates the concept of a sliding window. In this illustration, a one year sliding window was used. Two instances of the sliding window are shown together with their corresponding FFT components.

The sliding window DFT formulation of 4.1 can be written as

$$\mathbf{Y}_i = \mathbf{F}_N \mathbf{y}_i \quad i \in \{1, N - L + 1\}, \tag{4.12}$$

where $\mathbf{y}_i = [y_i, y_{i+1}, y_{i+2}, ..., y_{i+L-1}]$, N is the length of the time-series and L is the window size. The

mean and annual time-series can then be expressed as

$$\mu = \{Y(1)_1, Y(1)_2, Y(1)_3, ..., Y(1)_{,N-L+1}\}, \tag{4.13}$$

$$\alpha = \{2|Y(C_a)_1|, 2|Y(C_a)_2|, 2|Y(C_a)_3|, ..., 2|Y(C_a)_{,N-L+1}|\}. \tag{4.14}$$

$$\tag{4.15}$$

Where μ is the mean time-series and α is the amplitude time-series. $Y(z)_i$ is the zth value of vector $\mathbf{Y}_i$ and C_a is the location of the annual FFT component, determined by the window size (see equation 4.11). Having μ^{SWF} and α^{SWF}, a distance metric D_μ and D_α can be calculated similar to (4.9) and (4.9) as:

$$D_\mu = \max\{\mu_{k,1} - \mu_{k,2}\}, \quad 1 \le k \le N - L + 1, \tag{4.16}$$

and

$$D_\alpha = \max\{\alpha_{k,1} - \alpha_{k,2}\}, \quad 1 \le k \le N - L + 1. \tag{4.17}$$

4.6 SUMMARY

Previous research has found that class separability is achievable by considering the difference in FFT components related to the NDVI time-series of two different classes [56]. In particular, the mean and annual FFT components are considered as they tend to carry the majority of signal energy [56, 57]. It is proposed that this concept be extended by modeling the NDVI time-series as a triply modulated cosine function with varying mean, amplitude and phase and estimating these parameters for each time-step using an EKF. In short, by using this time domain approach, the mean, amplitude and phase is estimated for each time-step as opposed to the frequency domain approach that assumes a stationary time-series and consequently only gives a single estimate of the mean and annual frequency component. Having iterative estimates of these components allows one to exploit the fact that the mean and annual frequency dissimilarity is more prevalent during certain parts of the seasonal cycle than others, an effect that is merely averaged out using the traditional FFT over the entire NDVI time-series. A sliding window FFT approach was also introduced for comparison, unlike the traditional FFT method [56], the sliding window FFT also produces a time-series of the mean and amplitude and using the same methodology as with the EKF method, a change metric can be derived by computing the maximum deviation in the mean and amplitude time-series respectively. A comparison between the three methods is given in chapter 6.

A further application of the EKF method is towards land-cover change detection. By following the changes of the cosine parameters through time and comparing them with neighboring pixels, a change detection method can be formulated. This possibility is further explored in the following chapter.

CHAPTER FIVE

DETECTING LAND-COVER CHANGE USING MODIS TIME-SERIES DATA

5.1 INTRODUCTION

In this chapter two novel change detection methods are proposed. The first method, hereafter referred to as the EKF change detection method, is based on the work done in the previous chapter. The algorithm acts as a per-pixel change alarm and takes as input the NDVI time-series of a 3×3 grid of MODIS pixels. The NDVI time-series for each of these pixels was modeled as a triply (mean, phase and amplitude) modulated cosine function, and an EKF was used to estimate the parameters of the modulated cosine function for each time-step. A spatial comparison between the center pixel of the the 3×3 grid and each of its neighboring pixel's mean and amplitude parameter sequence was done to calculate a change metric. This change metric is then compared to a threshold to yield a change or no-change decision.

The second method, hereafter referred to as the temporal ACF change detection method, is a per-pixel change alarm that uses temporal autocorrelation to infer a change metric which also yields a change or no-change decision after thresholding.

A third method, which is based on the work of Lunetta et al. [17] (see section 2.7.1.3), is also shown in this chapter. This method uses a MODIS NDVI time-series to determine the occurrence of change in areas that are typically covered by natural vegetation and was included for comparison. All three these methods were compared with one another and their results are presented in chapter 6.

Both of the proposed methods (EKF and ACF change detection methods) make use of a simulated change dataset for initial parameter estimation. Making use of simulated or synthetic data is a

well-known concept in the remote sensing community [25, 97, 98]. The use of simulated change data is twofold. Firstly, during development of the new method the simulated change data were used to optimize the method and to tentatively evaluate the performance of the algorithm. Simulation was opted for during the optimization phase, since new settlement developments are infrequently mapped on an ad hoc basis in South Africa and the data on known settlement development amount to a relatively small number of MODIS pixels. Secondly, the start date and rate of the land-cover change could be controlled in the simulated or synthetic data which greatly facilitates the development and evaluation phases. After the method was optimized and performing well on simulated (synthetic) change data, it was evaluated by applying it to examples of known new settlement developments in South Africa.

5.2 EKF CHANGE DETECTION METHOD

Based on the results obtained in the previous chapter, the focus in this chapter shifts towards land-cover change detection. In the previous chapter it was shown that a triply modulated cosine function can be used to model an NDVI time-series and that the parameters of the function can be estimated for each time-step using a non-linear EKF. The consequent μ and α parameter stream is expected to be similar for the same class land-cover types and dissimilar for different land-cover types when considering natural vegetation and settlement pixels. Assuming that land-cover separability is achievable, it can be inferred that when a land-cover type changes from a naturally vegetated state to a settlement state, the corresponding μ and α parameter sequence will also be affected. The proposed method uses a MODIS 8-day NDVI time-series (see section 2.18) to calculate a change metric by means of a spatial comparison of the EKF parameter sequence of any given pixel with that of its neighboring pixels. The objective was to demonstrate that by making use of an EKF-derived change metric and a threshold optimized based on simulated land-cover change, a semi-supervised change detection method can be formulated that accurately detects change using MODIS NDVI time-series data.

5.2.1 Change metric formulation

As was shown in chapter 4, the NDVI time-series for a given pixel can be modeled by a triply modulated cosine function given as

$$y_k = \mu_k + \alpha_k \cos(\omega k + \phi_k) + v_k, \tag{5.1}$$

where y_k denotes the observed value of the NDVI time-series at time k and v_k is the noise sample at time k. The values of μ_k, α_k and ϕ_k are functions of time, and must be estimated given y_k for
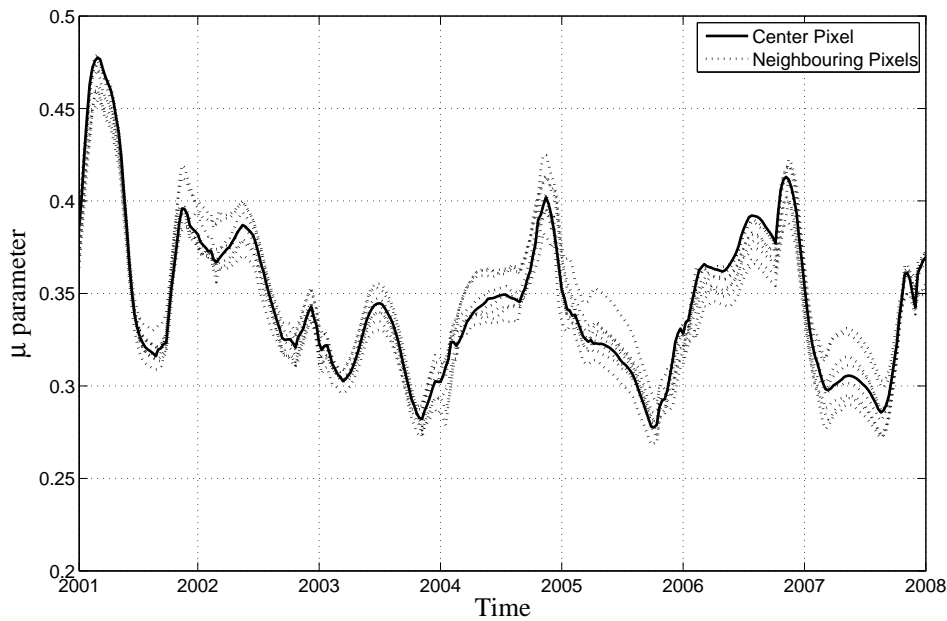
FIGURE 5.1: Mean parameter sequence comparison of a 3×3 pixel grid having an unchanged center pixel.

$k \in 1, \ldots, N$ [99, 100]. An EKF was used to estimate these parameters for every increment of k. The estimated values for $\mathbf{x}_k = [\mu_k \; \alpha_k \; \phi_k]^T$ over time k effectively results in a time-series for each of the three parameters.

Having the parameter sequence for μ_k, α_k and ϕ_k for $k \in 1, \ldots, N$ for a given pixel, a change detection method was formulated by comparing the parameter sequences of the pixel with that of its direct neighboring pixels. This effectively means focusing on the center pixel of a 3×3 grid of pixels and examining each neighboring pixel's EKF parameter sequence relative to the center pixel. It was found that the ϕ parameter sequence does not yield any significant separability between natural vegetation and settlement land-cover types and consequently only the μ and α parameter sequences were considered (See section 6.2.2).

Figure 5.1 shows the μ parameter sequence of a natural vegetation pixel over the seven-year study period compared to that of its neighboring pixels. As expected, the μ parameter sequence for the nine pixels is highly correlated. Figure 5.2 shows the μ parameter sequence for the same grid but with the center pixel gradually changing to settlement over a 6 month period. It is clear that the μ parameter sequence for the center pixel becomes less correlated with that of its neighboring pixels. The μ and α parameter sequence difference between the center pixel and an arbitrary neighboring pixel at time k
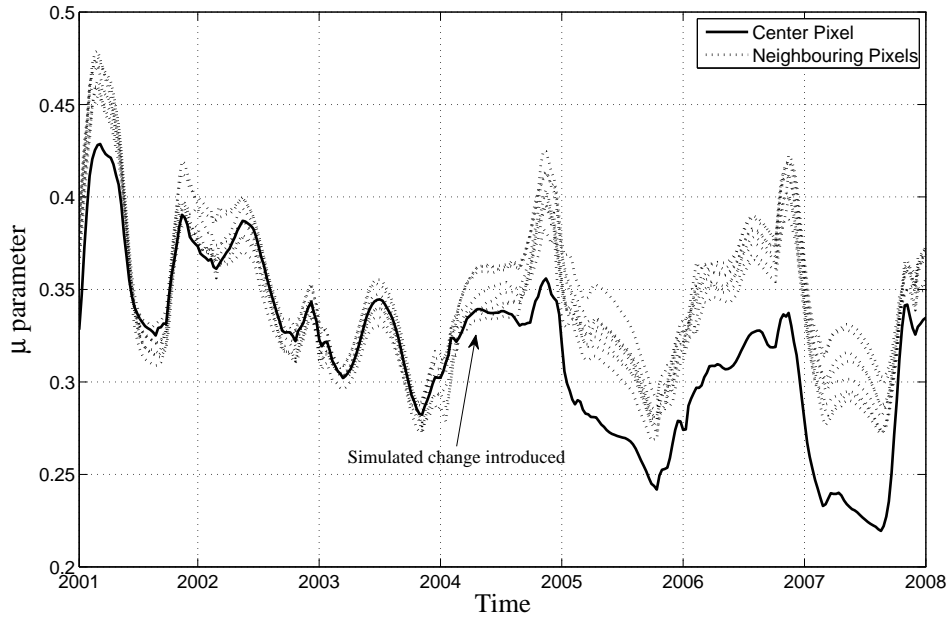
FIGURE 5.2: Mean parameter sequence comparison of a 3×3 pixel grid with simulated natural vegetation to settlement change introduced to the center pixel.

can be written as

$$D_{\mu(n)}^k = |\mu_k - \mu_k^n| \ \ n \in 1, \ldots, 8, \tag{5.2}$$

$$D_{\alpha(n)}^k = |\alpha_k - \alpha_k^n| \ \ n \in 1, \ldots, 8, \tag{5.3}$$

where $D_{\mu(n)}^k$ is the distance between the μ parameter sequence of a selected pixel (μ_k) with its nth neighboring pixel (μ_k^n) at time k. $D_{\alpha(n)}^k$ is the distance between the α parameter sequence of a selected pixel (α_k) with its nth neighboring pixel (α_k^n) at time k. Equation 5.2 and 5.3 can be combined as

$$D_n^k = D_{\mu(n)}^k + D_{\alpha(n)}^k \ n \in 1, \ldots, 8. \tag{5.4}$$

Having obtained the distance of the center pixel's parameter sequences relative to each of the neighboring pixel's parameter sequences, these could be combined at time k by simply adding all the values of $D_n^k \ n \in 1, \ldots, 8$ at time k

$$D^k = \sum_{n=1}^{8} D_n^k \ k \in 1, \ldots, N. \tag{5.5}$$

Having vector $\mathbf{D} = [D^1 \ D^2 \ D^3 \ \ldots \ D^N]$, a change metric was derived by firstly determining how the relative distance of the parameter sequences between the center pixel and its neighboring pixel changes
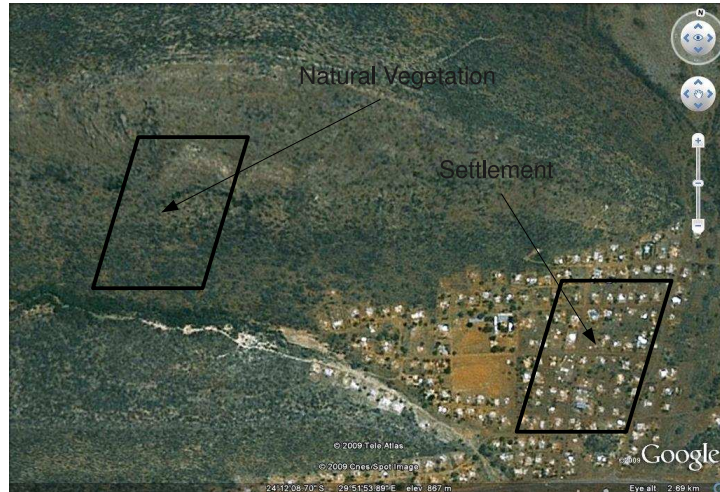
FIGURE 5.3: 500 m MODIS pixel covering natural vegetation and settlement land-cover in close proximity (courtesy of Google$^{\text{TM}}$Earth).

through time. This was done by differentiating the vector D. A single change metric was then derived by summing all the values of the differentiated D vector to yield

$$\delta = \sum_{k=2}^{N} |D^k - D^{k-1}|, \tag{5.6}$$

where δ is a single valued change metric for the center pixel of the 3×3 pixel grid. The change metric for each of the pixels in the study area was thus calculated by sliding a 3×3 pixel grid over the entire study area and calculating δ for the center pixel in each case.

5.2.2 Off-line optimization phase

Simulated change data are used together with a no-change dataset to optimize and tentatively evaluate the change detection method. Simulated change data were created by linearly blending a time-series of a pixel covered by natural vegetation with that of a pixel of a settlement which is in close proximity to ensure that the rainfall, soil type and local climate was similar. Figure 5.3 shows the footprint of a typical MODIS pixel covered by natural vegetation and a settlement pixel in close proximity. Figure 5.4 shows the corresponding NDVI time-series from 2001/01 to 2008/01 for each of these pixels as well as the simulated time-series where the blending period was set at 6, 12 and 24 months respectively with the midpoint of the blending period being 2004/04. It was found that the method was not sensitive to the exact date of change but rather to the transition duration, hence the variable simulated blending period. As was discussed in section 5.2.1, the algorithm uses a 3×3 pixel grid with the center pixel being compared to all neighboring pixels. It is, however, not realistic to assume that only the center pixel has changed with all neighboring pixels remaining unchanged. For this reason,
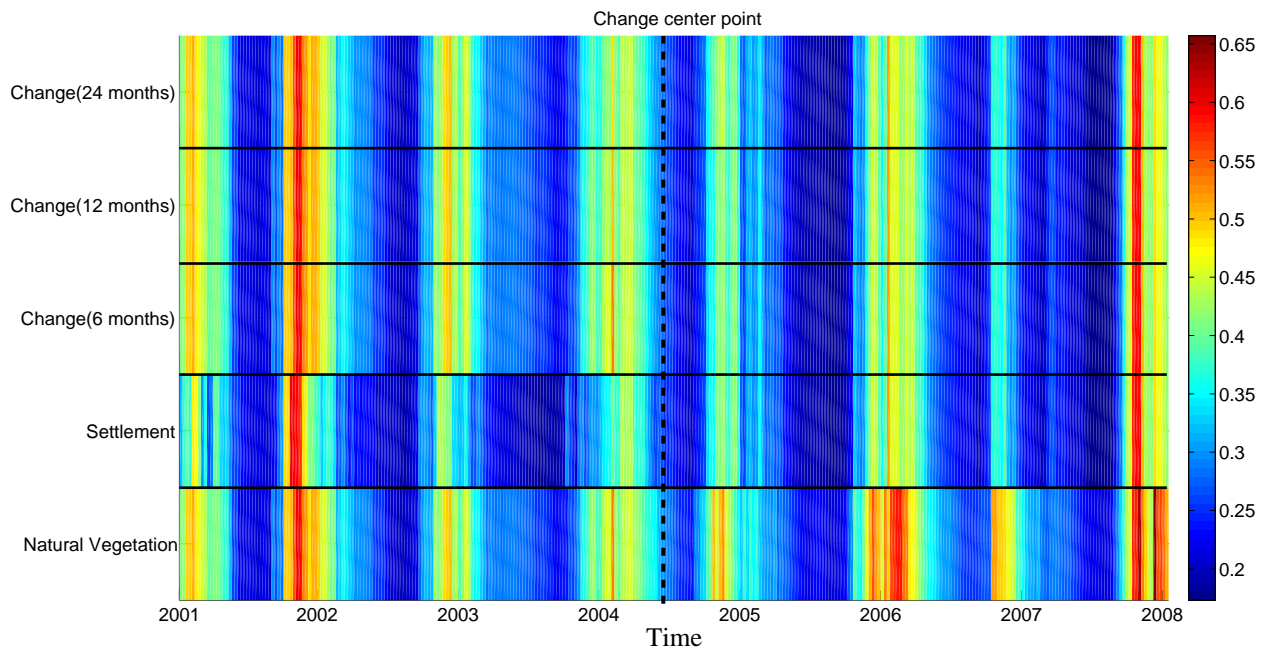
FIGURE 5.4: NDVI time-series of natural vegetation, settlement and simulated change pixels where the simulated change time-series had blending periods of 6, 12 and 24 months respectively.

the center pixel, together with a subset of neighboring pixels (zero to all eight), were subjected to a simulated land-cover change. The simulated change for each of the neighboring pixels was done in a similar manner, ensuring that the initial state of each neighboring pixel is in a vegetated state and gradually blends to a settlement state.

As previously stated, the method requires an *a-priori* database of simulated change and no-change examples. The change metric is firstly calculated (equation 5.6) for all the no-change and simulated change pixels in the database. The distribution of δ for both cases is then calculated. Figure 5.5 shows an example of the anticipated distribution of δ in the case of no-change $p(\delta|\overline{C})$ and simulated change $p(\delta|C_r^p)$ respectively. In $p(\delta|C_r^p)$, r is the rate of simulated change, i.e. 6, 12 or 24 months and p is the number of pixels in the 3×3 grid subjected to a simulated change. The value of the optimal threshold (δ^*) will change depending on the value of p and r respectively. The Bayesian decision error can be calculated as
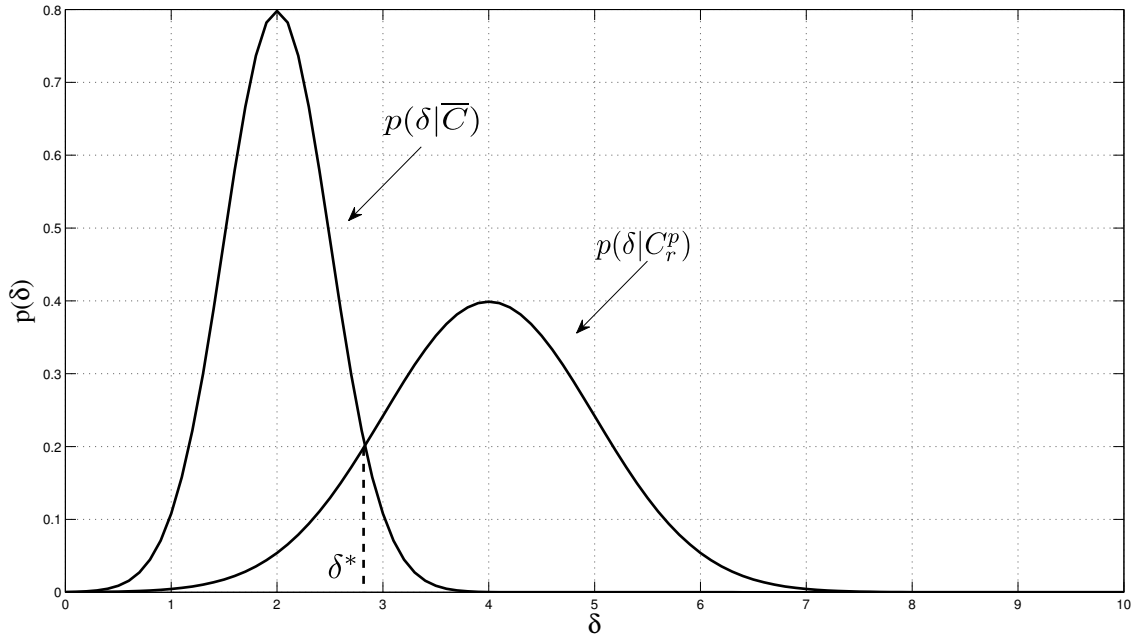
FIGURE 5.5: Probability distribution of δ in the case of no-change $p(\delta|\overline{C})$ and simulated change $p(\delta|C_r^p)$ respectively.

$$P(C|C) = \int_{\delta=\delta^*}^{\delta=\infty} p(\delta|C_r^p), \tag{5.7}$$

$$P(C|\overline{C}) = \int_{\delta=\delta^*}^{\delta=\infty} p(\delta|\overline{C}), \tag{5.8}$$

$$P(\overline{C}|C) = \int_{\delta=0}^{\delta=\delta^*} p(\delta|C_r^p), \tag{5.9}$$

$$P(\overline{C}|\overline{C}) = \int_{\delta=0}^{\delta=\delta^*} p(\delta|\overline{C}). \tag{5.10}$$

$P(C|C)$ is the probability that a change was detected given that a change was introduced (percentage change correctly detected), $P(C|\overline{C})$ is the probability that a change was detected given that no change was introduced (percentage false alarms), $P(\overline{C}|C)$ is the probability that no change was detected given that a change was introduced and $P(\overline{C}|\overline{C})$ is the probability that no change was detected given that no change was introduced (5.7)-(5.10). The value of δ^* is the optimal decision threshold that minimizes the Bayesian decision error.

The underlying idea is that $p(\delta|\overline{C})$, which is estimated using actual no-change examples, remains constant, while $p(\delta|C_r^p)$ which is estimated using simulated change data varies for different realizations of p and r. This implies that that δ^* will vary for different values of r and p. By calculating δ^* for all
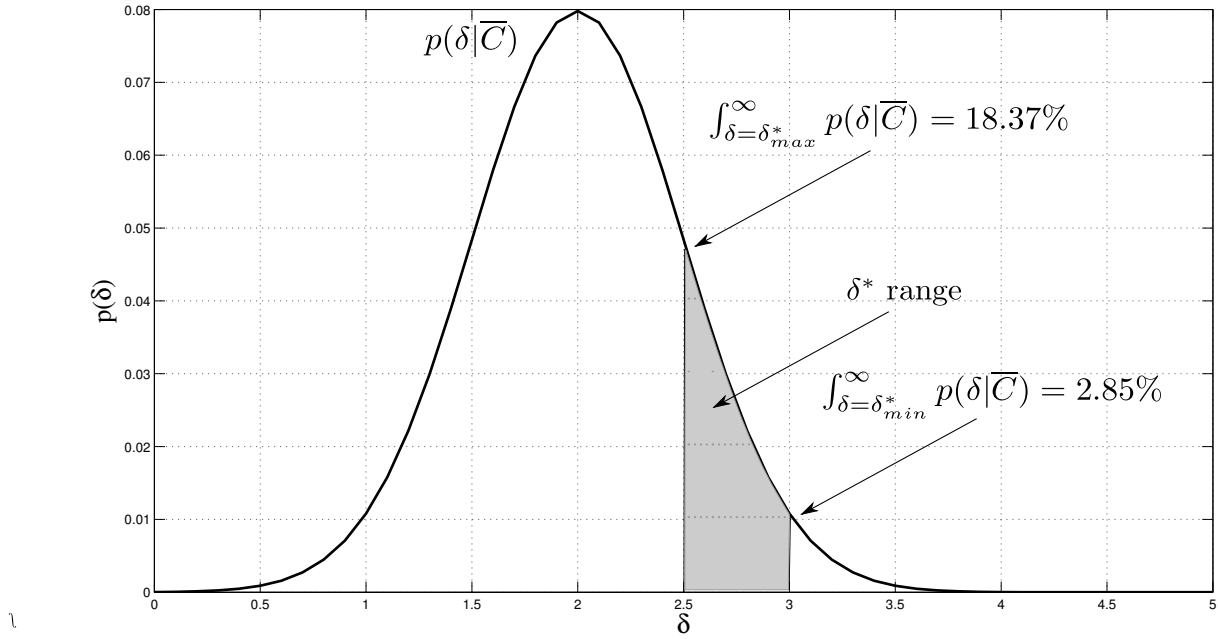
FIGURE 5.6: Range of δ^* and corresponding maximum and minimum false alarm rate.

values of $r \in \{6, 12, 24\}$ and $p = \{1, 2, 3, ..., 9\}$, will result in a range of δ^* values. Each of the δ^* values in this range result in a different false alarm rate, calculated using $p(\delta|\overline{C})$. Figure 5.6 shows an example of $p(\delta|\overline{C})$, together with a range of δ^*, which was determined by means of simulated change with all permutations of $r \in \{6, 12, 24\}$ and $p = \{1, 2, 3, ..., 9\}$. The corresponding maximum and minimum false alarm rate is also shown. Having a range of false alarm rates that were identified as being optimal for different change scenarios, it is up to the operator to select the maximum allowable false alarm rate that is deemed acceptable in the given application environment.

5.2.3   Operational phase

The threshold that is selected for operational use $(\widehat{\delta})$ is within the range $[\delta^*_{\min}, \delta^*_{\max}]$ and corresponds to the maximum allowable false alarm rate (Δ) chosen by an operator for the specific application and region. The δ^* value corresponding to Δ $(\widehat{\delta})$ is expressed as:

$$\widehat{\delta} = \delta^* \ \text{ where } \int_{\delta=\delta^*}^{\delta=\infty} p(\delta|\overline{C}) = \Delta \ \ \delta^* \in [\delta^*_{min}, \delta^*_{max}]. \tag{5.11}$$

Having the value of $\widehat{\delta}$, the EKF change detection method is run in an unsupervised manner for the entire study area. The value of δ (equation 5.6) is calculated for each pixel and a change is declared if δ exceeds the threshold value $\widehat{\delta}$

$$
\text{Change} = \begin{cases} \text{true} & \text{if } \delta \geq \widehat{\delta} \\ \text{false} & \text{if } \delta < \widehat{\delta}. \end{cases}
$$

For example, if the no-change PDF corresponded to the one shown in Figure 5.6, the region of the optimal false alarm rate would be between 2.85% and 13.37%, which corresponds to a δ^* value of 3 and 2.5 respectively. An operator thus needs to choose the maximum allowable false alarm rate within the aforementioned range. If the maximum false alarm rate chosen by the operator was 10%, the corresponding value of δ^* could easily be determined as being 2.65, in which case:

$$
\text{Change} = \begin{cases} \text{true} & \text{if } \delta \geq 2.65 \\ \text{false} & \text{if } \delta < 2.65. \end{cases}
$$

5.3 TEMPORAL ACF METHOD

The ACF, in the temporal context, have been used selectively in remote sensing [101], but is mostly applied in the spatial context [102], [103]. In this section the temporal ACF of a pixel's time-series was considered. An ACF of a time-series that is stationary behaves differently from an ACF of a time-series that is non-stationary due to land-cover change.It should be noted that the ACF of a non-stationary time-series under the ergodic assumption can not be technically defined as being the ACF of the time-series. When referring to the ACF in this context, it only refers to the ACF operation performed on the given time-series under the assumption that the time-series is stationary. By determining suitable detection parameters using only a no-change database, it will be shown that real land-cover change can be detected reliably in a semi-supervised fashion.

Similar to the EKF change detection method, the temporal ACF change detection method uses a two-stage approach. Firstly, a simulated change dataset, together with a no-change dataset, is used in an off-line optimization phase to determine the appropriate parameters (band, lag and threshold selection). Second, the method is run in an unsupervised manner using the parameter-set that was determined during the aforementioned off-line optimization phase. These two stages will be discussed in further detail in the following sections.

5.3.1 Change metric formulation

Assume that the time-series for any given band of MODIS is expressed as:

$$
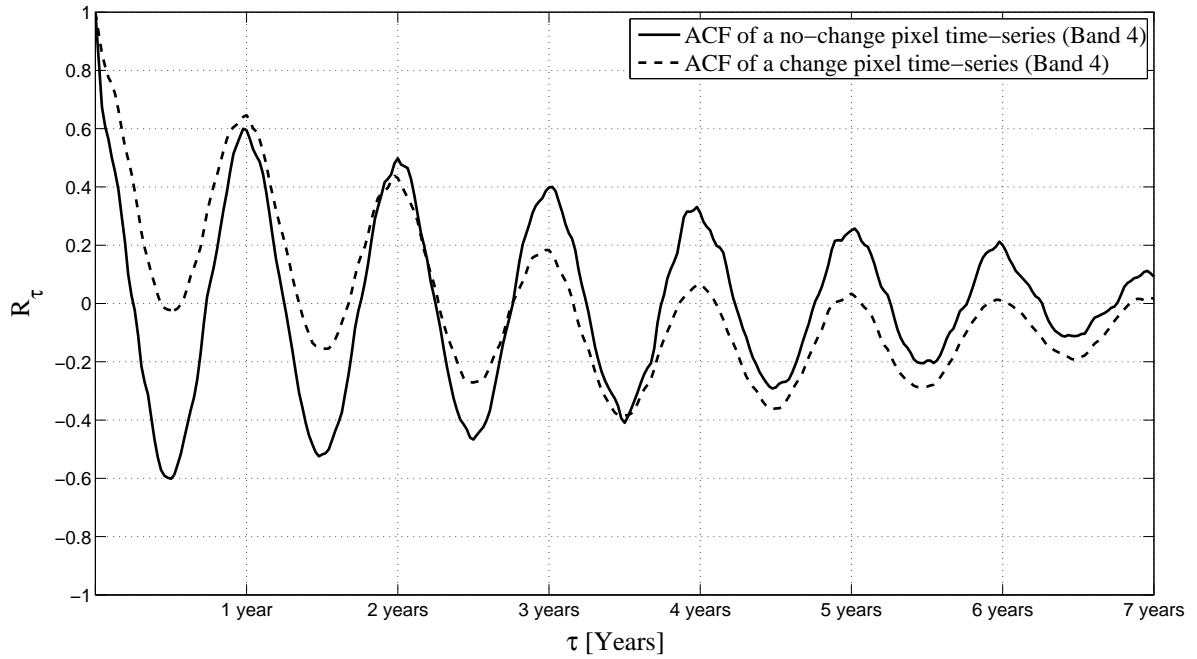X_n^b \ \ n \in \{1, 2, ..., N\} \ b \in \{1, 2, ..., 8\}, \tag{5.12}
$$

FIGURE 5.7: Autocorrelation of a change and no-change pixel's MODIS band 4 time-series.

where X_n^b is the observation from spectral band b at time n and N is the number of time-series observations available. It should be noted that band 8 in (5.12) refers to computed NDVI. It is assumed that N is equal for all seven bands.

The normalized ACF for time-series $\mathbf{X}^b = [X_1^b, X_2^b, ..., X_N^b]$ can then be expressed as:

$$R^b(\tau) = \frac{E[(X_n^b - \mu^b)(X_{n+\tau}^b - \mu^b)]}{\text{var}(\mathbf{X}^b)}, \tag{5.13}$$

where τ is the time-lag and E denotes the expectation. The mean of $\mathbf{X}^b$ is given as μ^b and the variance, which is used for normalization, is given as $\text{var}(\mathbf{X}^b)$. Figure 5.7 shows the typical ACF of an actual change and no-change pixel's time-series. It is clear that the no-change pixel has a symmetrical form relative to the $R^b(\tau) = 0$ axis, whereas the change pixel shows a strong non-symmetrical property. The reason for this is the stationarity requirement of the ACF in (5.13). The mean and variance of the time-series of X_n^b in (5.13) is required to remain constant through time to determine the true ACF of the time-series. The inconsistency of the mean and variance typically associated with a change pixel's non-stationary time-series thus becomes apparent when analyzing the ACF of the time-series. The change metric is thus simply equivalent to the temporal correlation of a specific band (b) at a specific lag (τ)
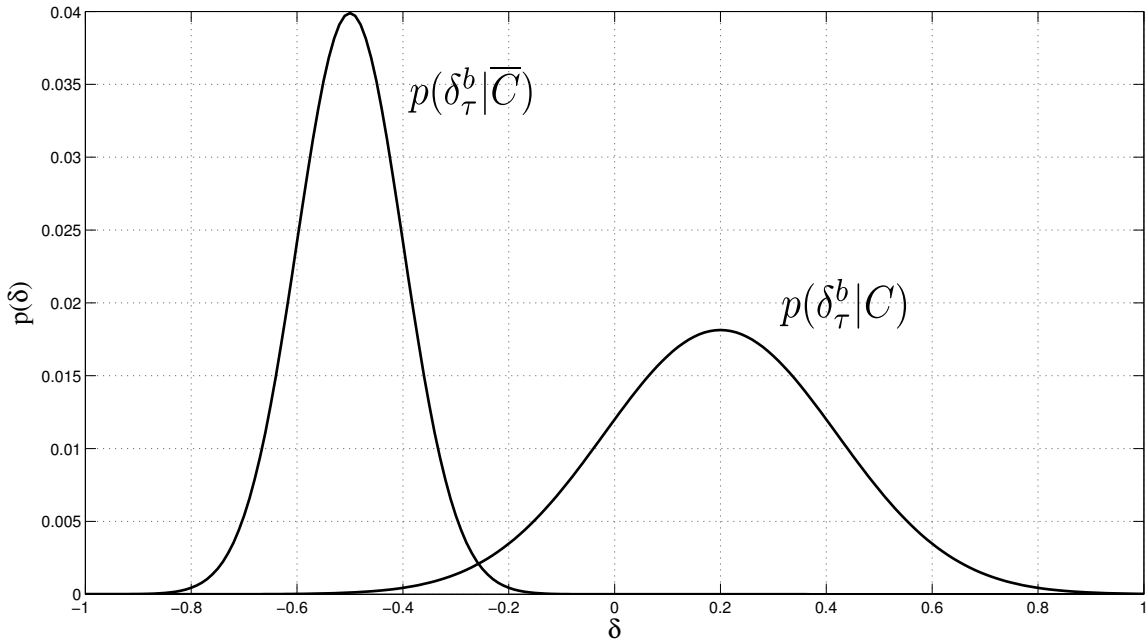
FIGURE 5.8: Example of the distribution of δ_τ^b in the case of change and no-change respectively.

$$R^b(\tau) = \delta_\tau^b. \tag{5.14}$$

It is clear, however, that the distribution of δ_τ^b in the case of change and no-change, as shown in figure 5.8, will vary for different values of τ and b. The aim is thus to determine the value of τ and b in δ_τ^b that will result in the most separable distributions between δ_τ^b for the change ($p(\delta_\tau^b|C)$) and no-change ($p(\delta_\tau^b|\overline{C})$) case respectively. The value of the optimal threshold (δ_τ^{b*}) also needs to be determined. The selection procedure for these parameters are done in an off-line optimization phase and will be discussed in more detail in the following section.

5.3.2   Off-line optimization phase

Similar to the methodology used in section 5.2.2, a no-change and simulated change dataset is used to optimize the parameters of the temporal ACF change detection method. A simulated change dataset is generated by linearly blending a time-series of a pixel covered by natural vegetation with that of a settlement pixel time-series. Unlike the simulated change dataset used in section 5.2.2, the start date of change is chosen at random. The resulting simulated change database thus has a uniformly spread change date between 2001/01 and 2008/01 corresponding to the study period. The blending period was found not to influence the method's performance, and a representative blending period of

6 months was chosen.

The right sided normalized ACF for band b can be expressed as $R^b(\tau) = [R^b(0), R^b(1), ..., R^b(N)]$. The task at hand is to determine the separation between the ACF of the change and no-change dataset for each band at each lag. The Bayesian decision error in the form of a confusion matrix was calculated based on the distribution of the change metric δ_τ^b for the change and no-change dataset:

$$P(C|C) = \int_{\delta_\tau^b = \delta_\tau^{b*}}^{\delta_\tau^b = \infty} p(\delta_\tau^b|C),$$
(5.15)

$$P(C|\overline{C}) = \int_{\delta_\tau^b = \delta_\tau^{b*}}^{\delta_\tau^b = \infty} p(\delta_\tau^b|\overline{C}),$$
(5.16)

$$P(\overline{C}|C) = \int_{\delta_\tau^b = 0}^{\delta_\tau^b = \delta_\tau^{b*}} p(\delta_\tau^b|C),$$
(5.17)

$$P(\overline{C}|\overline{C}) = \int_{\delta_\tau^b = 0}^{\delta_\tau^b = \delta_\tau^{b*}} p(\delta_\tau^b|\overline{C}).$$
(5.18)

$P(C|C)$ is the probability that a change was detected given that a change was present (percentage change correctly detected), $P(C|\overline{C})$ is the probability that a change was detected given that no change was present (percentage false alarms), $P(\overline{C}|C)$ is the probability that no change was detected given that a change was introduced and $P(\overline{C}|\overline{C})$ is the probability that no change was detected given that no change was introduced. The value of δ_τ^{b*} is the optimal decision threshold. To relate the confusion matrix into a single measure of accuracy, the overall accuracy was calculated as:

$$O_A = \frac{P(C|C) + P(\overline{C}|\overline{C})}{P(C|C) + P(\overline{C}|\overline{C}) + P(C|\overline{C}) + P(\overline{C}|C)}.$$
(5.19)

The optimal value of τ, b and δ_τ^{b*} could thus be calculated by solving

$$[\tau, b, \delta_\tau^{b*}] = \underset{\tau, b, \delta_\tau^{b*}}{\mathrm{argmax}} \frac{\int_{\delta_\tau^b = \delta_\tau^{b*}}^{\delta_\tau^b = \infty} p(\delta_\tau^b|C) + \int_{\delta_\tau^b = 0}^{\delta_\tau^b = \delta_\tau^{b*}} p(\delta_\tau^b|\overline{C})}{\int_{\delta_\tau^b = \delta_\tau^{b*}}^{\delta_\tau^b = \infty} p(\delta_\tau^b|C) + \int_{\delta_\tau^b = 0}^{\delta_\tau^b = \delta_\tau^{b*}} p(\delta_\tau^b|\overline{C}) + \int_{\delta_\tau^b = \delta_\tau^{b*}}^{\delta_\tau^b = \infty} p(\delta_\tau^b|\overline{C}) + \int_{\delta_\tau^b = 0}^{\delta_\tau^b = \delta_\tau^{b*}} p(\delta_\tau^b|C)},$$
(5.20)

where $p(\delta_\tau^b|C)$ is estimated by means of the simulated change dataset and $p(\delta_\tau^b|\overline{C})$ is calculated using the no-change dataset.

5.3.3 Operational phase

After the off-line optimization phase is complete, the resulting parameters are used to run the algorithm in an unsupervised manner for the entire area of interest. A pixel is labeled as having changed by
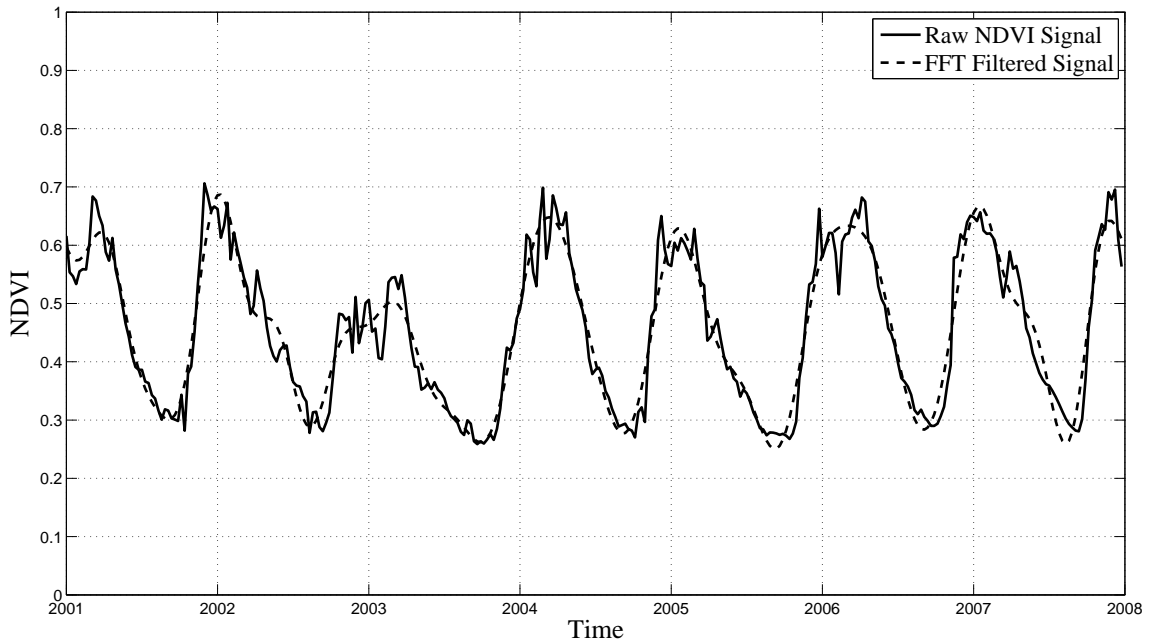
FIGURE 5.9: Comparison between a raw and filtered NDVI signal.

evaluating the following,

$$
\text{Change} = \begin{cases} \text{true} & \text{if } R^b(\tau) \geq \delta_\tau^{b*} \\ \text{false} & \text{if } R^b(\tau) < \delta_\tau^{b*}, \end{cases}
$$

where $R^b(\tau)$ is the ACF of band b evaluated at lag τ and δ_τ^{b*} is the decision threshold. The value of τ, b and δ_τ^{b*}, was provided in the aforementioned off-line optimization phase. The results obtained for both the off-line optimization phase and operational phase are presented in Chapter 6.

5.4　ANNUAL NDVI DIFFERENCING METHOD

Both the EKF and ACF change detection methods are compared to a computationally simple change detection method proposed by Lunetta *et al.* [17]. Using this method, the NDVI time-series was firstly filtered and cleaned using Fourier transformation filtering. In this step, the raw NDVI signal is transformed to the frequency domain using the FFT. The high frequency components are removed and the remainder is transformed back to the time-domain using the IFFT. Figure 5.9 shows the raw NDVI signal as well as the FFT filtered signal. It is clear that the filtered signal is considerably smoother than the original raw NDVI signal.

Assume that the entire time-series of the filtered NDVI time-series is denoted as

$$\mathbf{y} = [y_1, y_2, y_3, ..., y_N],$$ (5.21)

where $\mathbf{y}$ is a vector containing the filtered NDVI value for each time-step and N is the total number of observations. A new time-series can be obtained by summing all the filtered NDVI values for a year and reducing the time-series elements to the number of years.

$$\mathbf{c} = [c_1, c_2, c_3, ..., c_K],$$ (5.22)

where K is number of years that the time-series spans and c_i is the cumulative NDVI for year i given as:

$$c_i = \sum_{k=1+46(i-1)}^{k=46+46(i-1)} y_k.$$ (5.23)

The number 46 in equation 5.23 refers to the total number of eight day observations in a single year. The difference between the c_i for consecutive years can be expressed as a vector $\mathbf{d} = [d_1, d_2, d_3, ..d_{K-1}]$ where d_i is calculated as:

$$d_i = c_i - c_{i+1}.$$ (5.24)

The value of d_i is calculated for each of the pixels in the study area, the underlying idea being that pixels experiencing a considerable reduction in NDVI will have a higher d_i value and would thus be a good indication of land-cover change. The problem, however, is identifying a suitable threshold value that when compared to d_i, produces a change or no-change decision. The threshold value would obviously also need to be adjusted for each value of i. A pixel would be flagged as having changed if any of the values of d_i exceed the threshold δ_i for $i \in [1, 2, 3, .., K-1]$. A change vector could be formulated as $\zeta = \{\zeta_1, \zeta_2, \zeta_3, ..., \zeta_{K-1}\}$ where ζ_i is defined as

$$\zeta_i = \begin{cases} 0 & \text{if } d_i \geq \delta_i \\ 1 & \text{if } d_i > \delta_i. \end{cases}$$

A change or no-change decision is made as

$$\text{Change} = \begin{cases} \text{true} & \text{if } \sum \zeta > 0 \\ \text{false} & \text{if } \sum \zeta = 0. \end{cases}$$

Where $\sum \zeta$ refers to the summation of all the values in the vector ζ given as
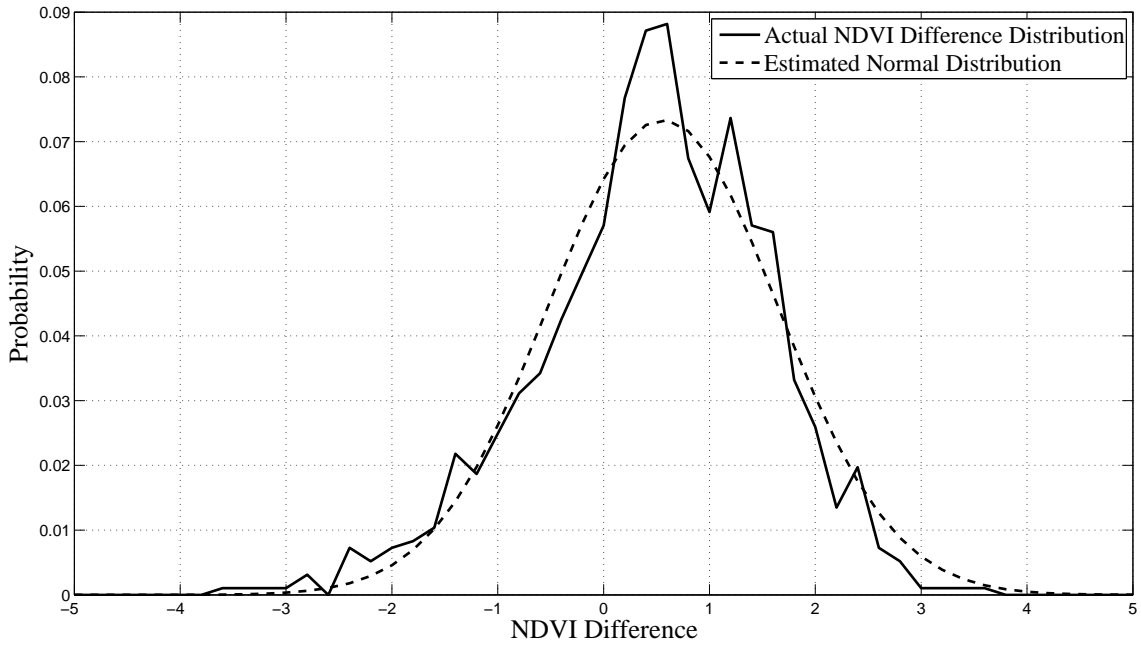
FIGURE 5.10: Distribution of the annual NDVI difference between 2002 and 2003 for the study period.

$$\sum \zeta = \sum_{i=1}^{K-1} \zeta_i. \tag{5.25}$$

Choosing the threshold values δ_i for $i \in \{1, 2, 3, .., K - 1\}$ is not a trivial task. This was achieved by using standard normal statistics. Firstly, the difference value (d_i, $i \in \{1, 2, 3, .., K - 1\}$) is computed for all the pixels in the study area. This is then used to estimate normal distribution $p(d_i)$ $i \in \{1, 2, 3, .., K - 1\}$. Figure 5.10 shows the annual NDVI difference between two consecutive years (2002 and 2003) during the study period. It can also be seen that the actual distribution of the NDVI difference is well approximated using a normal distribution.

Using standard normal distribution statistics, the threshold value δ_i was determined by choosing the NDVI difference value that corresponds to the z value that is representative of the *a-priori* probability of change in the study area [17]. Figure 5.11 shows a normal distribution. It can be seen that 95% of the values fall between a z value of -1.98 and 1.98 where 99% of the values are between the values of -2.58 and 2.58. It follows that if the *a-priori* change probability of 2.5% is expected for a specific area, the threshold value will correspond to a z value of 1.98 because only the right tail of the distribution is considered, as a reduction in NDVI from year to year will result in a positive d_i value when considering equation 5.24.
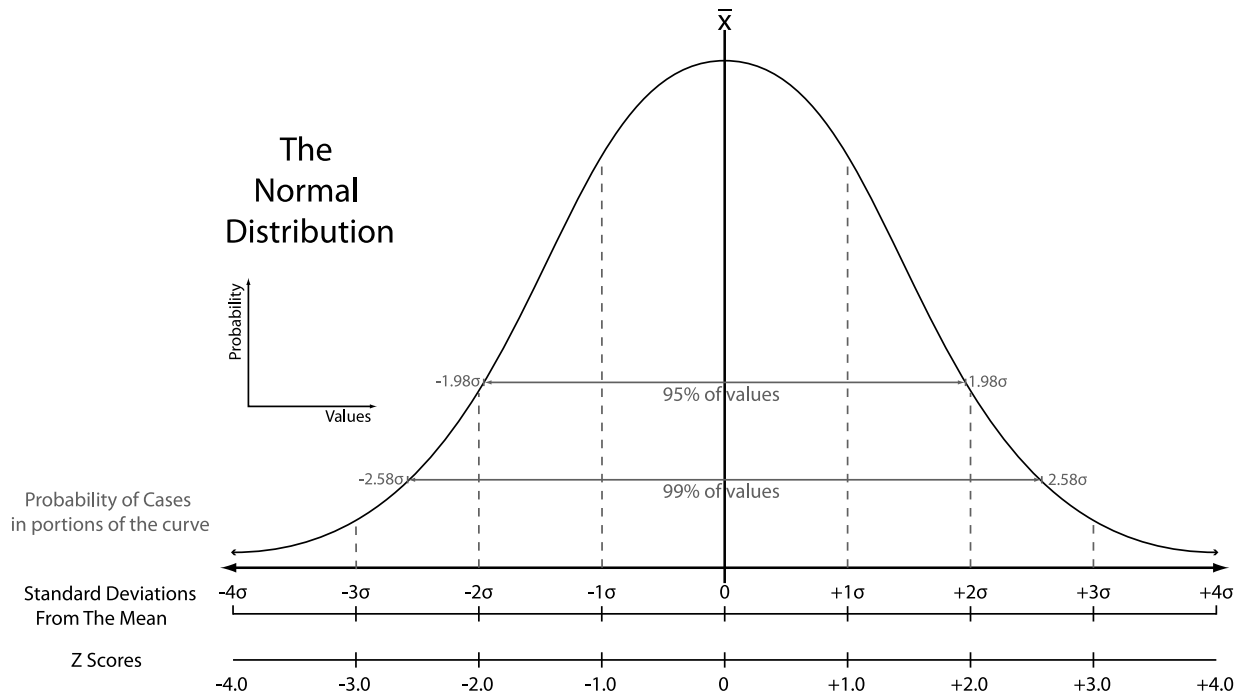
FIGURE 5.11: The Normal distribution.

5.5   SUMMARY

In this chapter, two novel land-cover change detection methods were proposed. The first method models an NDVI time-series as a triply modulated cosine function and estimates the mean, amplitude and phase for each time-increment using an EKF. A change index was derived by comparing each pixel's mean and amplitude parameters with that of its neighboring pixels, effectively considering the center pixel of a 3×3 grid of pixels. The threshold that determined whether the change index associated with each pixel should be classified as change or no-change was determined by means of land-cover change simulation.

The second method that was proposed is a temporal ACF change detection method. This method exploits the non-stationary property that is typical of a time-series of a pixel that undergoes land-cover change by considering the temporal ACF of the time-series. A change metric is defined by considering an ACF band and lag combination. The most appropriate band, lag and threshold selection is performed using a no-change and simulated change dataset.

For comparison, the NDVI differencing method proposed in [17] is also discussed. The performance of all three methods are evaluated on two study areas in South Africa, the results of which are presented in the following chapter.

CHAPTER SIX

RESULTS

The results for the three change detection methods presented in the previous chapter as well as the EKF framework proposed in chapter 4 are shown in this chapter. The procedure for identifying ground truth data which are used for training and validation is also shown.

6.1 IDENTIFYING EXAMPLES OF SETTLEMENT DEVELOPMENT

In any change detection method, representative examples of change and no-change are necessary for not only training (supervised methods) but also for validation of the change detection method. Examples of confirmed settlement developments and no-change areas were obtained by means of visual interpretation of high resolution Landsat and SPOT5 images of 2000 and 2008 respectively. The following sections shows how the ground truth examples of no-change natural vegetation and settlement MODIS pixels as well as examples of MODIS pixels that transitioned from natural vegetation to settlement were identified.

6.1.1 Identification of change pixels

The extraction of the MODIS ground truth pixels which transitioned from natural vegetation in 2000 to settlement by 2008, was done using a six-step process. A graphical representation of each step is shown in Figure 6.1. During the first step, the SPOT5 imagery of Limpopo were used to identify human settlements. On-screen digitizing was done by manually creating a polygon along the outer edge of each settlement area (Step 2). This settlement polygon was then displayed on a co-located Landsat image from 2000 (Step 3). If the settlement polygon identified in 2008, was covered by natural vegetation in 2000, the polygon is labeled as "changed". The next step was to extract the MODIS pixels corresponding to the area covered by the change polygon. This was done by overlying the change polygons on a MODIS grid and identifying all MODIS pixels that intersect the change
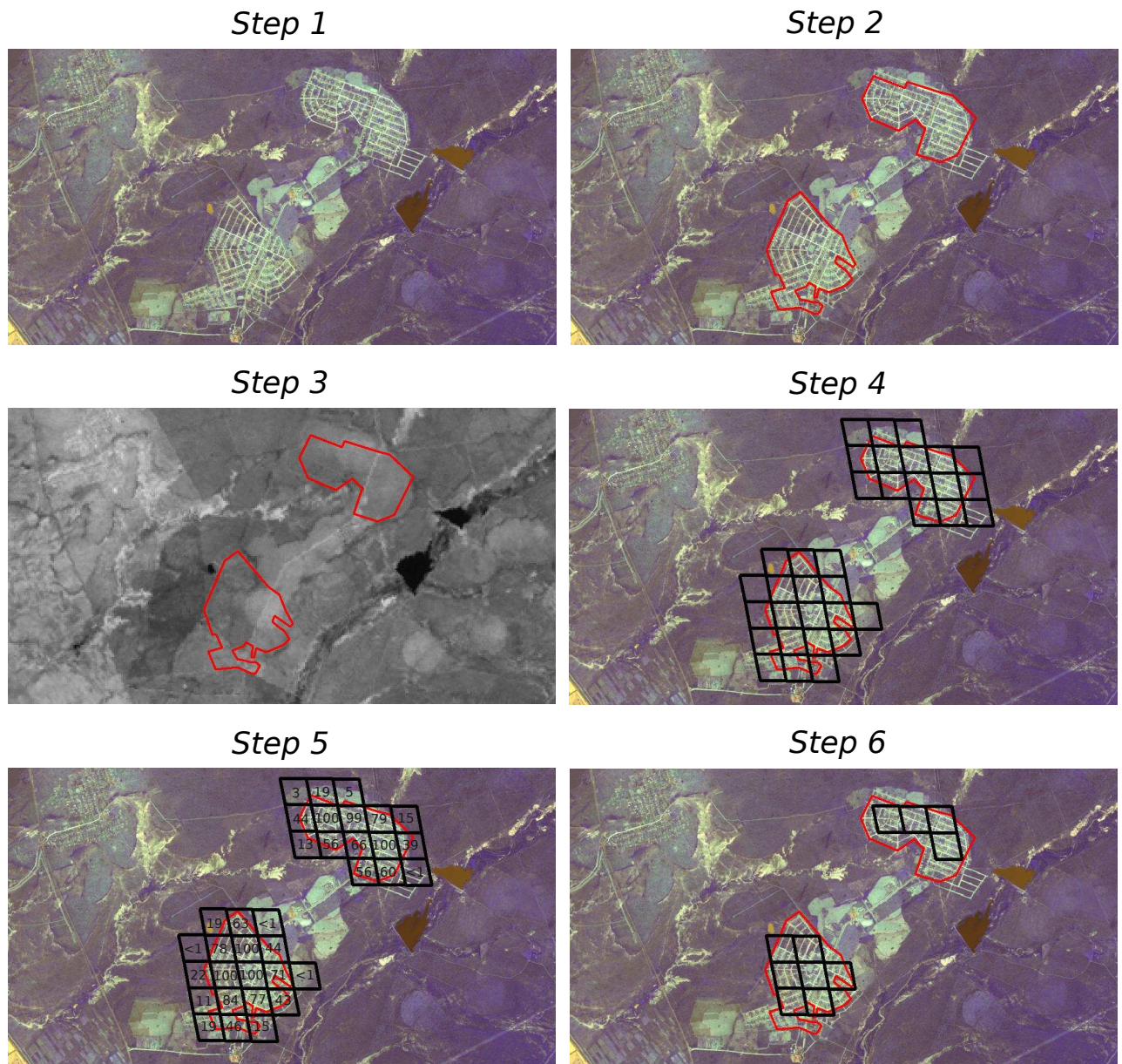
FIGURE 6.1: Graphical representation of the six steps used to identify MODIS pixels that changed from natural vegetation to settlement.

polygons (Step 4). The next step was to determine the percentage overlap between the settlement polygon and intersecting MODIS pixels (step 5). Step 5 of Figure 6.1 illustrates the percentage of polygon area intersecting each MODIS pixel. The final step was to identify the MODIS pixels that are covered by at least 70% of the change polygon, which yields the final set of MODIS pixels which changed from natural vegetation to settlement.

6.1.2   Identification of no-change pixels

The procedure for identifying no-change settlement MODIS pixels is very similar to the procedure described in the previous section with the only difference being step 3. If the Landsat 2000 image shows that the settlement polygon identified in 2008 corresponds to a settlement area in 2000, the polygon is classified as being a "no-change" settlement polygon. The procedure for extracting the corresponding MODIS pixels was done using steps 4 to 6 described in the previous section. The procedure for identifying no-change natural vegetation pixels is also conceptually similar. Representative natural vegetation areas were identified throughout the study area using the 2008 SPOT5 imagery. Polygons were created manually by means of on-screen digitization. These polygons were compared to co-located Landsat imagery in 2000 to ensure land-cover class consistency. Once the "no-change" natural vegetation polygons were identified, the process of extracting the corresponding MODIS pixels was performed using steps 4 to 6 as described in section 6.1.1.

6.1.3   Validation of MODIS pixels using Google Earth

High resolution satellite imagery in Google Earth are being used more routinely in the validation of land cover products [104]. As a validation procedure, the MODIS pixels identified during the process given in sections 6.1.1 and 6.1.2 were investigated in Google Earth using QuickBird imagery of multiple dates (Figure 6.2). The true color, high resolution QuickBird images from Google Earth proved very useful when inspecting the class membership of MODIS pixels at different time-instances. The only problem with using Google Earth for validation is that certain areas are imaged more regularly than other areas and thus multiple images are not available everywhere. This implies that in certain areas only one image was available which does not provide any information on the land cover change history of MODIS pixels.
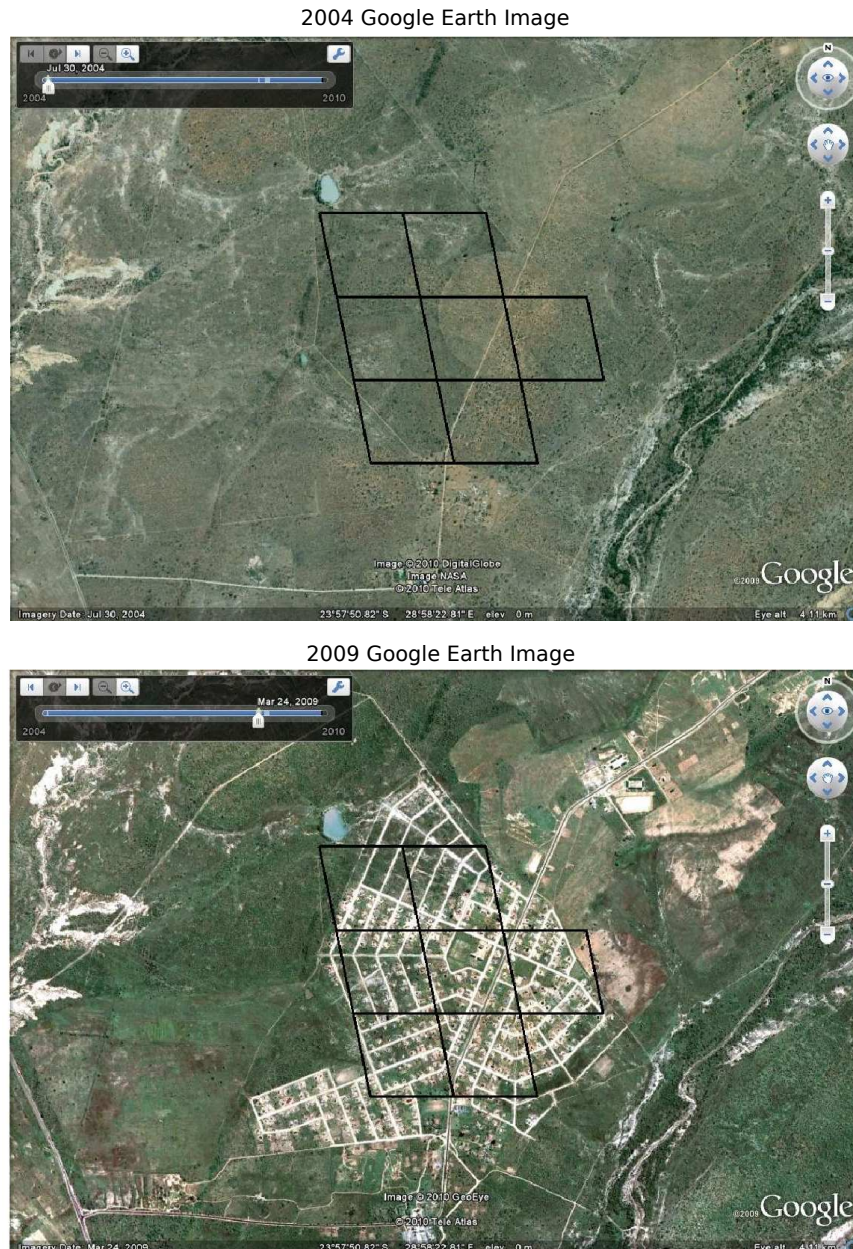
2004 Google Earth Image

2009 Google Earth Image

FIGURE 6.2: Validating MODIS pixels using QuickBird imagery at different dates (courtesy of Google^{TM}Earth).

6.2 IMPROVING CLASS SEPARABILITY USING AN EXTENDED KALMAN FILTER

6.2.1 Study area used for testing class separability

The methods introduced in chapter 4 were tested in two regions in the Limpopo province. The first study area (Region A) is centered around latitude $24°17'21.43''$S and longitude $29°39'42.96''$E and is 43 km south east of the city of Polokwane. Region A covers a geographic area of approximately 190 km^2,
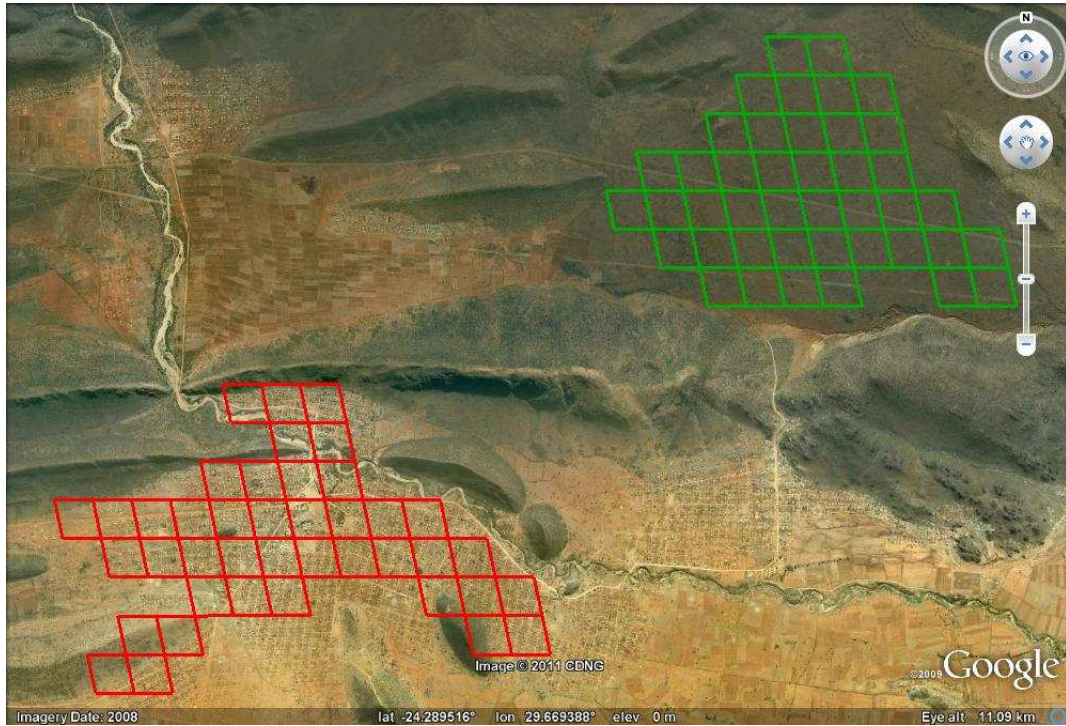
FIGURE 6.3: QuickBird image of Region A together with the MODIS pixels corresponding to the natural vegetation and settlement areas (courtesy of Google™Earth).

42 natural vegetation and 42 settlement pixels were selected for analysis. Region B is centered around latitude $24°19'51.50''$S and longitude $29°18'04.07''$E and is 47 km south west of the city of Polokwane. Region B covers a geographical area of 100 km^2, 32 settlement and 61 natural vegetation pixels were selected. The study regions that were considered had settlements and natural vegetation areas in close proximity which ensured that the rainfall, soil type and local climate were similar. Figure 6.3 shows the MODIS pixels that where selected for region A. Each of the MODIS pixels were evaluated using SPOT5 high resolution data to ensure that none of them had experienced any land-cover change during the study period (Section 6.1).

6.2.2 Separability results and discussion

To recap from chapter 4, the separability between two arbitrary NDVI time-series can be determined by comparing the spectral characteristics of the two time-series by making use of the FFT. In particular, the distance between the first and annual FFT components are calculated which produces a scalar quantity in each case. Based on these distance metrics, the similarity between two NDVI time-series are quantified. When using the EKF to estimate the μ and α parameter sequence for each NDVI time-series, the difference between the parameter sequences fluctuates over time. This is illustrated in figure 6.4 where the μ sequence estimated using the EKF is shown along with the FFT mean
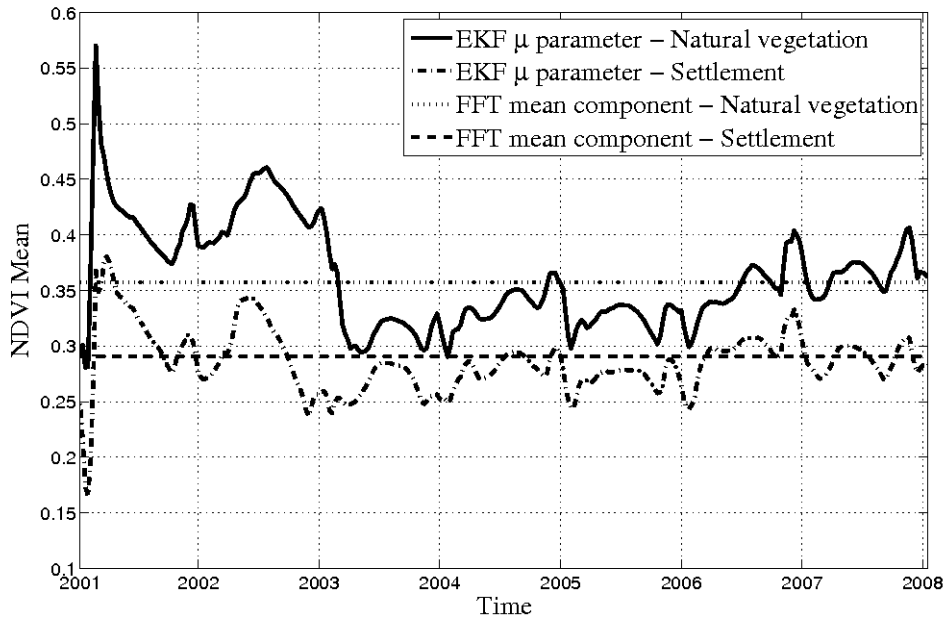
FIGURE 6.4: Comparing the EKF derived μ parameter with the FFT mean component for natural vegetation and settlement for region A.

component for two typical NDVI time-series belonging to each of the two classes in region A.

The μ sequence for the settlement and natural vegetation time-series clearly vary in similarity (Figure 6.4). This is to be expected as land-cover classes tend to be more similar during certain seasons than others. This characteristic was exploited by only considering the maximum distance between each pair of parameter sequences.

In essence, both approaches takes as input two NDVI time-series and outputs two distance metrics, D_μ and D_α, which is then subsequently used to quantify the similarity between these two NDVI time-series. In order to determine which of these methods produce the best measure of similarity, the joint distribution of D_μ and D_α can be calculated using same-class NDVI time-series examples ($p(D_\mu, D_\alpha|s)$) and then compared to the corresponding distribution using different-class NDVI time-series examples ($p(D_\mu, D_\alpha|d)$). By integrating the relevant densities over the overlapping areas of these distributions, the Bayes' error can be calculated and used to determine the performance of each method. The underlying idea is that the lower the Bayes' error, the more "unique" the distributions and consequently, the better the class separability. $p(D_\mu, D_\alpha|s)$ was estimated by comparing the NDVI time-series of each pixel in the natural vegetation class with each pixel in the natural vegetation class, as well as each pixel in the settlement class with each pixel in the settlement class, calculating

D_μ and D_α for each instance. Similarly, $p(D_\mu, D_\alpha|d)$ was estimated by comparing the NDVI time-series of each pixel in the natural vegetation class with each of the pixels in the settlement class and calculating D_μ and D_α for each instance. The distributions $p(D_\mu, D_\alpha|s)$ and $p(D_\mu, D_\alpha|d)$ where estimated by means of the Parzen-Rosenblatt window method using Gaussian kernels [105, 106].

For the EKF method, the initial state parameters as well as the observation and process noise estimates were determined off-line, based on known training data from the study areas. The training data were a random selection of 5% of the total number of pixels per region. The initial state parameters were calculated using the FFT mean and annual components of the training data as

$$\mu_1 = \sum_{i=1}^{Z} \frac{\mathbf{Y}_0^i}{Z}, \tag{6.1}$$

$$\alpha_1 = \sum_{i=1}^{Z} \frac{2\|\mathbf{Y}_7^i\|}{Z}, \tag{6.2}$$

$$\phi_1 = \sum_{i=1}^{Z} \frac{\angle \mathbf{Y}_7^i}{Z}. \tag{6.3}$$

Where Z is the total number of training time-series and $\mathbf{Y}_n^i$ is the n'th FFT component of time-series i. The observation noise was determined as

$$\sigma_v = \sum_{i=1}^{Z} \frac{\mathrm{std}(\mathbf{e}_i)}{Z} \tag{6.4}$$

$$\mathbf{e}_i = \|\hat{\mathbf{y}}_i - \mathbf{y}_i\|. \tag{6.5}$$

Here σ_v is the estimated standard deviation of the observation noise, $\mathrm{std}(\mathbf{e}_i)$ is the standard deviation of a vector containing the difference between the original time-series $\mathbf{y}_i$ and a filtered version $\hat{\mathbf{y}}_i$ calculated as

$$\hat{\mathbf{y}}_i = \mathbf{F}_N^{-1} \hat{\mathbf{Y}}^i. \tag{6.6}$$

$\hat{\mathbf{Y}}^i$ is defined as

$$\widehat{Y}^i(k) = \begin{cases} Y^i(k), & k = \{0, 7\} \\ 0, & 1 \le k \le 6 \\ 0, & 8 \le k \le N \end{cases}, \tag{6.7}$$

TABLE 6.1: Initial EKF state parameter values.

Region	μ_1	α_1	ϕ_1
A	0.3008	0.0835	0.2700
B	0.3447	0.1185	0.1708

TABLE 6.2: EKF observation and process noise values.

Region	σ_v	σ_μ	σ_α	σ_ϕ
A	3.8×10^{-2}	8×10^{-5}	8×10^{-5}	1.5×10^{-2}
B	4.4×10^{-2}	9×10^{-5}	9×10^{-5}	1.7×10^{-2}

and $\mathbf{F}_N^{-1}$ denotes the inverse DFT operation. $\hat{\mathbf{Y}}^i$ is thus a copy of $\mathbf{Y}^i$ but with only the mean and seasonal FFT components. All other components were set to zero.

The initial state parameters as well as the observation and process noise standard deviation for region A and B is shown in Table 6.1 and 6.2 respectively. The values of μ_1, α_1 and ϕ_1 in Table 6.1 were calculated using equations (6.1), (6.2) and (6.3) respectively. In Table 6.2, the observation noise variance σ_v was calculated using equations (6.4) and (6.5) while the process noise variance σ_μ, σ_α and σ_ϕ were estimated by maximizing the class separability on the training data for each region. This was done by determining the parameter distributions of each of the classes using the training data, and varying the ratio between σ_v and each of the process noise components. Using the maximum distance between distributions as criterion and a non-linear optimizer, the corresponding process noise parameters were determined.

Once determined, the parameters were kept fixed for all numerical results relating to the specific region. Figure 6.5 shows the joint distribution of D_μ and D_α using the FFT method (A) and EKF method (B) respectively. Here, $p(D_\mu, D_\alpha|s_f)$ is the distribution of D_μ and D_α calculated using the FFT method and using same class NDVI examples, $p(D_\mu, D_\alpha|d_f)$ is the distribution of D_μ and D_α calculated using the FFT method and using different class NDVI examples, $p(D_\mu, D_\alpha|s_k)$ is the distribution of D_μ and D_α calculated using the EKF method and using same class NDVI examples and $p(D_\mu, D_\alpha|d_k)$ is the distribution of D_μ and D_α calculated using the EKF method and using different
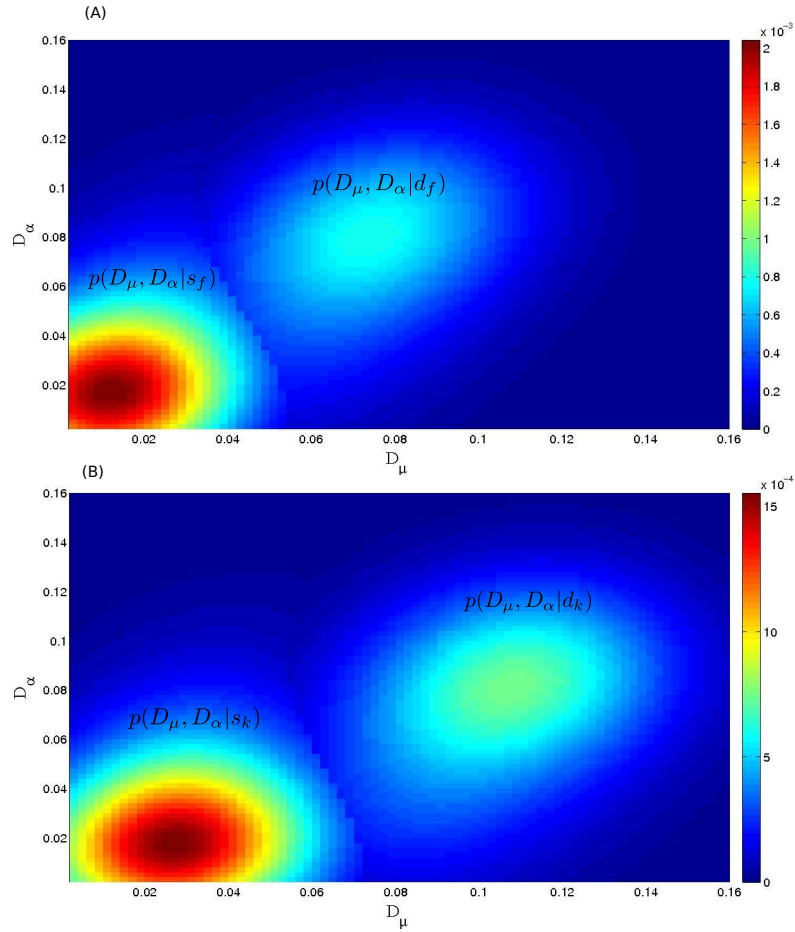
FIGURE 6.5: Joint distribution of D_μ and D_α using the FFT method (A) and EKF method (B) where $p(D_\mu, D_\alpha|s_f)$ is the distribution of D_μ and D_α calculated using the FFT method and using same class NDVI examples, $p(D_\mu, D_\alpha|d_f)$ is the distribution of D_μ and D_α calculated using the FFT method and using different class NDVI examples, $p(D_\mu, D_\alpha|s_k)$ is the distribution of D_μ and D_α calculated using the EKF method and using same class NDVI examples and $p(D_\mu, D_\alpha|d_k)$ is the distribution of D_μ and D_α calculated using the EKF method and using different class NDVI examples.

class NDVI examples. Table 6.3 gives the Bayesian decision error for both the FFT and EKF methods as well as the standard deviation of the error. The standard deviation was computed by using a random subset of 90% of the time-series to estimate the distributions $p(D_\mu, D_\alpha|s)$ and $p(D_\mu, D_\alpha|d)$ to infer the Bayes' error, and then repeating the experiment 10 times.

Consistent with most EKF implementations, the tracking of state parameters is not instantaneous and does require a certain number of observations. As this period is unknown, an initial number of state parameter values need to be excluded when calculating D_α and D_μ. The average square difference between the EKF derived μ parameter and the FFT mean component is shown in figure 6.6, it can be seen that the variation seems to stabilize within the first two years which relates to approximately 100 samples.
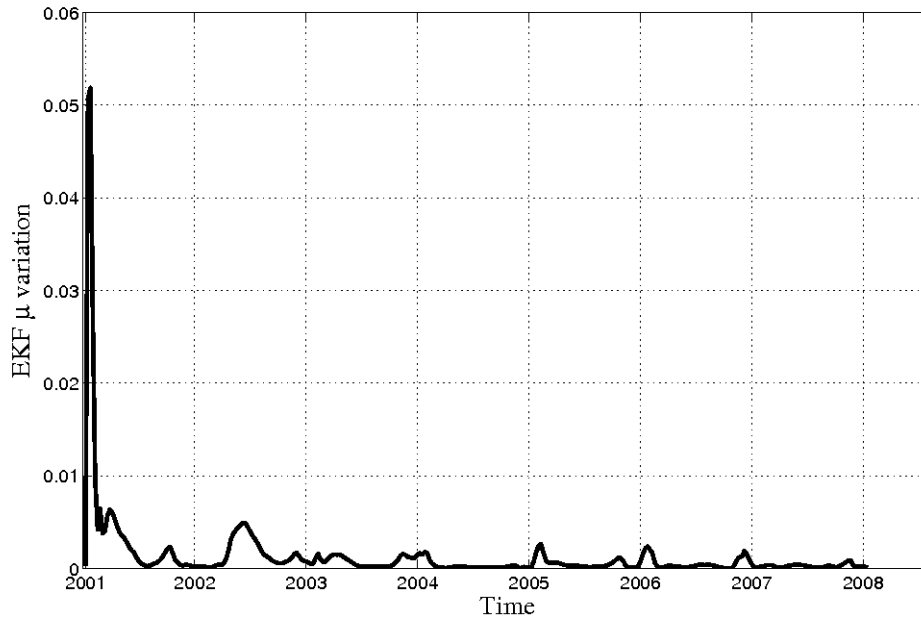
FIGURE 6.6: Average square difference between the EKF derived μ parameter and the FFT mean component for all settlement pixels in Region A.

It can be seen from Table 6.3 that the Bayesian decision error in region A (P_e^{EKF}) using the EKF was reduced by nearly 5% over the FFT method (P_e^{FFT}). In region B the Bayes' error of the EKF method was reduced by 2.63% over the FFT method. The standard deviation of the error probability was also reduced using the EKF method for both regions. Thus, overall it may be concluded that the EKF formulation has a reduced probability of error which implies that the EKF formulation offers improved separability of land-cover classes for the study areas A and B. The phase parameter ϕ was found to provide negligible additional separability (less than 0.01%) in the classes and was consequently disregarded.

As discussed in section 4.5, a sliding window alternative was proposed to extend on the FFT method presented in [56]. The mean and amplitude could be extracted by considering the relevant FFT components of a windowed FFT iterating through the time-series with the value of D_μ and D_α being calculated in an identical manner as was proposed for the EKF method (see section 4.5). The Bayes' error for the EKF, FFT and sliding window (SW) FFT method together with the corresponding variance of each of these methods are shown in figure 6.7 . The window size of the SW FFT method was varied between one and five years, denoted as SW FFT 1 to SW FFT 5 (figure 6.7).

Table 6.3: Bayes' error of the FFT and EKF method for region A and B. Percentage in parentheses indicates the standard deviation of the error.

Region	P_e^{FFT}	P_e^{EKF}
A	9.33% (1.95%)	4.34% (0.77%)
B	5.85% (1.60%)	3.22% (1.24%)

The overall improved separability of natural vegetation and settlement land-cover types using the EKF based on a triply modulated cosine function model over FFT and sliding window FFT is evident for both regions A and B. In an effort to improve the results, a sum of sinusoids model was also considered but preliminary results showed a negligible performance increase with a significant increase in the complexity as more parameters needed to be estimated. This corresponds to results shown in [56], where no significant added separability was achieved when considering more sinusoidal components other than the annual component.

In conclusion, the initialization procedure used to determine the initial EKF parameters as shown in section 6.2.2 was found to work well for each region. By using an initial training set and keeping the EKF initialization parameters constant for each region, the EKF is effectively adaptable for each region and requires minimal manual parameter selection. It was also found that the sliding window FFT method did improve on the standard FFT method when the correct window size was selected. The optimal window size for region A was 2 years whereas the optimal window size for region B was 1 year (figure 6.7). The EKF method had a lower percentage error compared to the sliding window FFT, regardless of the window size.
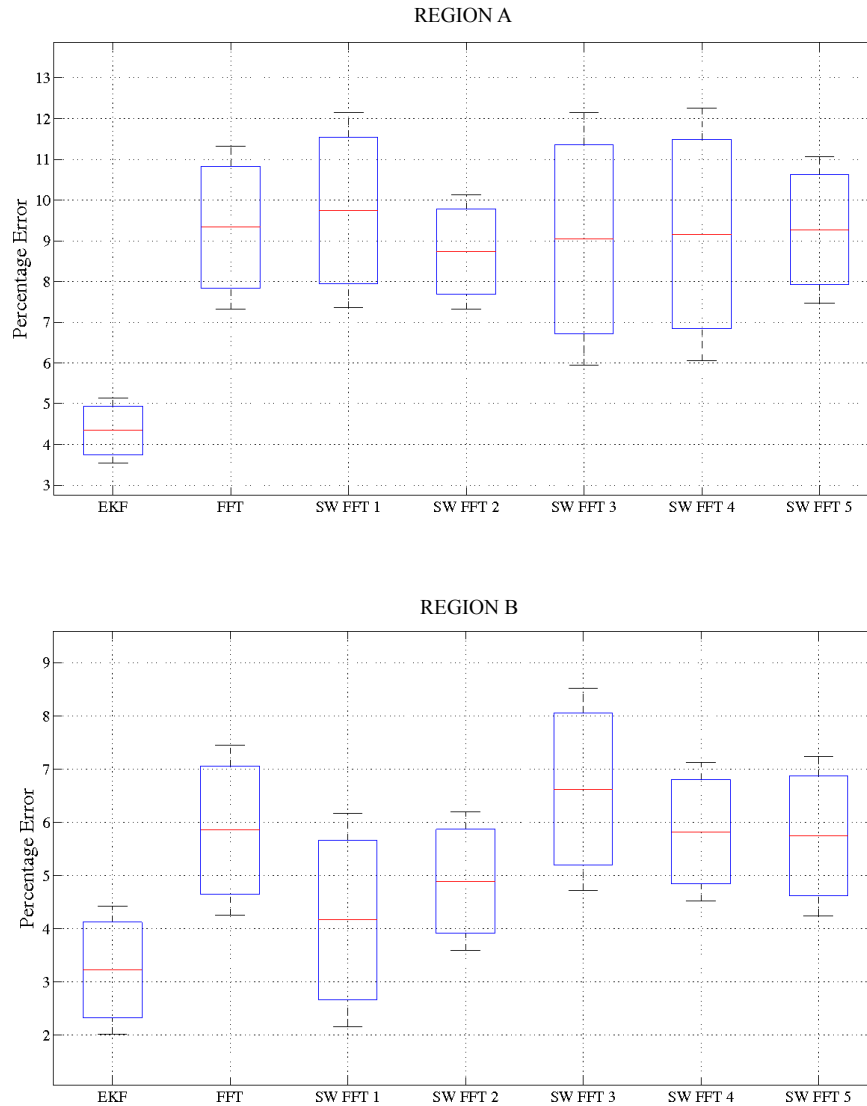
FIGURE 6.7: The Bayes' error and variance for the EKF, FFT and SW FFT method for region A and B. The window size of the SW FFT method was varied between one and five years.

6.3 DETECTING LAND-COVER CHANGE IN THE LIMPOPO PROVINCE OF SOUTH AFRICA

The Limpopo province is located in the northern region of South Africa. Figure 6.8 shows the location of the province. In this region, large families typically live under low-density conditions as opposed to high density squatter communities that live on the urban fringe in southern regions [7]. The province has a history of isolation from major urban and industrial centers. When compared to the rest of the country, people in this province are more reliant on subsistence production. Limpopo is one of the poorest provinces with more than 70% of people living under the poverty line [107]. The predominant land-cover type in the province is natural vegetation with the land use being mostly informal [107].
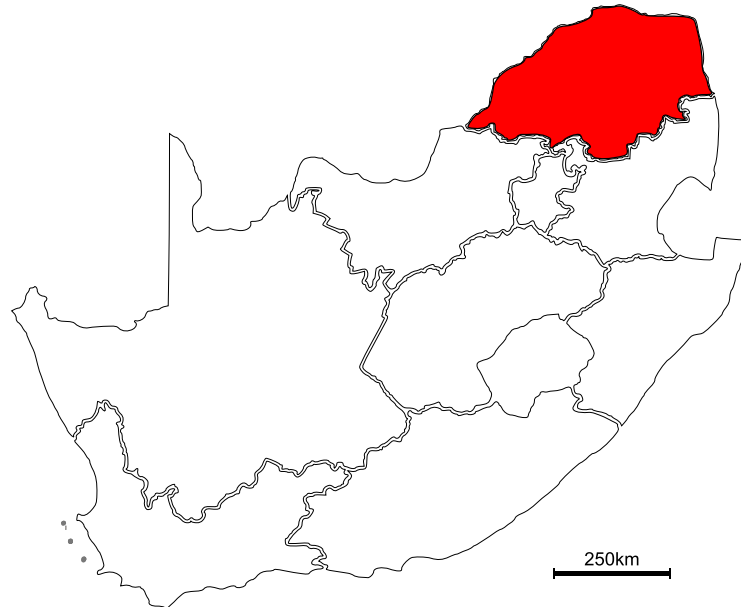
FIGURE 6.8: Location of the Limpopo province in South Africa.

The study area covers an approximate $25\,000$ km^2 having an upper left coordinate of ($23°20'12.09''$S ; $28°35'25.18''$E) and a lower right coordinate of ($25°00'14.59''$S ; $30°06'58.30''$E).

A total of 1 497 examples of natural vegetation, 1 735 examples of settlement and 117 examples of real change 500 m MODIS pixels were identified within the study area. Landsat and SPOT high resolution data were used to identify the aforementioned pixels as described in section 6.1.

6.3.1   Evaluation of the EKF change detection method in Limpopo

6.3.1.1   Off-line optimization of the EKF method in Limpopo

The simulated change dataset was generated using the methodology proposed in section 5.2.2. Roughly half (750 pixels) of the natural vegetation dataset were used to generate the simulated dataset. Each of these pixels were blended with a settlement pixel as described in section 5.2.2. The value of δ^* (as described in section 5.2.2) is shown for 6, 12 and 24 month blending periods in tables 6.4, 6.5 and 6.6 respectively. It is clear that the value of δ^* varies between 1.68 (when only the center pixel changing over a six-month period) and 1.37 (when all 9 pixels are changing over a 24-month period).

Table 6.4: Land-cover change detection accuracy, false alarm rate and optimal threshold (δ^*) for a range of pixels having changed in the 3×3 pixel grid using the EKF change detection method in Limpopo. The simulated change had a 6-month blending period and the value in parentheses indicates the standard deviation.

Number of pixels changed in 3×3 grid	Detection accuracy	False alarm rate	δ^*
1	91.79% (0.91%)	7.92% (0.67%)	1.68 (0.03)
2	92.90% (0.84%)	8.48% (0.62%)	1.65 (0.03)
3	92.59% (0.62%)	8.61% (0.60%)	1.66 (0.02)
4	92.63% (0.58%)	9.19% (0.93%)	1.63 (0.02)
5	92.70% (0.71%)	10.03% (1.21%)	1.59 (0.03)
6	93.11% (1.04%)	11.21% (0.60%)	1.56 (0.01)
7	92.73% (1.06%)	12.87% (0.93%)	1.52 (0.01)
8	90.88% (0.83%)	14.78% (0.73%)	1.47 (0.01)
9	90.42% (0.93%)	17.83% (1.01%)	1.42 (0.01)

The corresponding false alarm rate varies between 7.92% and 22.13% respectively. It follows that the operator needs to choose the maximum desirable false alarm rate in the aforementioned false alarm rate range. For this application, that maximum false alarm rate was chosen to be 13%. Substituting these values in equation 5.11:

$$\widehat{\delta} = \delta^* \ \text{where} \int_{\delta=\delta^*}^{\delta=\infty} p(\delta|\overline{C}) = 13\% \ \ \delta^* \in [1.36, 1.68], \tag{6.8}$$

$\widehat{\delta}$ was calculated as 1.5 and was used to determine change in the operational phase, as will be discussed in the following section.

6.3.1.2   Real change detection performance of the EKF method in Limpopo

Substituting the value of $\widehat{\delta}$ yields,

$$\text{Change} = \begin{cases} \text{true} & \text{if } \delta \geq 1.5 \\ \text{false} & \text{if } \delta < 1.5. \end{cases}$$

The change detection accuracy using the threshold of 1.5 was 89% using the 117 examples of real change in the study area. The false alarm rate was 13%.

Table 6.5: Land-cover change detection accuracy, false alarm rate and optimal threshold (δ^*) for a range of pixels having changed in the 3×3 pixel grid using the EKF change detection method in Limpopo. The simulated change had a 12-month blending period and the value in parentheses indicates the standard deviation.

Number of pixels changed in 3×3 grid	Detection accuracy	False alarm rate	δ^*
1	91.22% (0.96%)	7.92% (1.09%)	1.68 (0.04)
2	91.97% (0.84%)	8.24% (0.67%)	1.66 (0.02)
3	92.56% (0.65%)	8.64% (0.84%)	1.64 (0.03)
4	92.46% (1.16%)	9.27% (1.15%)	1.62 (0.02)
5	92.65% (0.95%)	10.38% (0.93%)	1.59 (0.02)
6	92.69% (0.60%)	11.53% (1.03%)	1.55 (0.01)
7	91.65% (1.25%)	13.06% (0.87%)	1.50 (0.02)
8	89.77% (1.11%)	15.25% (0.89%)	1.46 (0.01)
9	89.65% (0.91%)	18.83% (0.98%)	1.40 (0.01)

Table 6.6: Land-cover change detection accuracy, false alarm rate and optimal threshold (δ^*) for a range of pixels having changed in the 3×3 pixel grid using the EKF change detection method in Limpopo. The simulated change had a 24-month blending period and the value in parentheses indicates the standard deviation.

Number of pixels changed in 3×3 grid	Change simulated	No Change simulated	δ^*
1	91.46% (0.74%)	9.25% (0.79%)	1.63 (0.02)
2	91.54% (1.20%)	9.33% (0.86%)	1.63 (0.01)
3	91.53% (0.65%)	10.25% (1.18%)	1.61 (0.02)
4	92.12% (0.66%)	11.10% (0.53%)	1.58 (0.02)
5	92.34% (0.86%)	11.52% (1.14%)	1.54 (0.01)
6	92.47% (0.58%)	13.69% (1.18%)	1.50 (0.01)
7	90.63% (0.82%)	14.93% (1.37%)	1.48 (0.01)
8	87.98% (0.49%)	17.53% (0.98%)	1.43 (0.01)
9	87.06% (1.24%)	22.13% (0.61%)	1.37 (0.01)

Table 6.7: Confusion Matrix, overall accuracy (O_A) and optimal threshold (δ^*) showing the best land-cover change detection performance during the ACF method's off-line optimization phase using MODIS band 4 *(550 nm)* with a lag of 104 days. Value in parentheses indicates the standard deviation.

	Simulated change (n=750)	No Change (n=1616)	δ^*	O_A
Change Detected	78.16% (1.5%)	12.25% (1.4%)	0.13 (0.01)	82.95% (1.4%)
No Change Detected	21.84% (1.5%)	87.75% (1.4%)		

6.3.2 Evaluation of the temporal ACF change detection method in Limpopo

6.3.2.1 Off-line optimization of the ACF method in Limpopo

As described in section 5.3.2, a subset of the no-change dataset, consisting of vegetation and settlement pixels were used in the off-line optimization phase. Of the available 1 497 examples of natural vegetation and 1 735 settlement pixels, 750 simulated change pixels were generated by linearly blending a time-series of a pixel covered by natural vegetation with that of a settlement pixel time-series (Section 5.3.2). The resulting simulated change database had a uniformly spread change date between 2001/01 and 2008/01. The blending period was found not to influence the method's performance [108], and a representative blending period of six months was chosen. From the total of 3 232 no-change pixels, a random selection of 1 616 pixels were used during the off-line optimization phase with the remainder (1 616 pixels) being used to infer the false alarm rate performance during the real change detection phase.

The overall accuracy (O_A) as calculated in (5.19) was calculated for each band $b \in \{1, 2, ..., 8\}$ and lag $\tau \in \{1, 2, ..., 46\}$ using the no-change and change dataset described above is shown in figure 6.9. It was found that the highest overall detection accuracy was obtained by using the change index $\delta_\tau^b = \delta_{13}^4 = R^4(13)$. Because the time-series has an observation of 8 days, the τ value of 13 corresponds to 104 days. The value of δ_{13}^{4*} was found to be 0.13. Table 6.7 summarizes the performance of the method when using the aforementioned parameters.

6.3.2.2 Real change detection performance of the ACF method in Limpopo

After the band, lag and optimal threshold selection was completed, the performance of the proposed method was validated using the no-change and real change datasets. A change or no-change decision for each pixel was obtained by evaluating
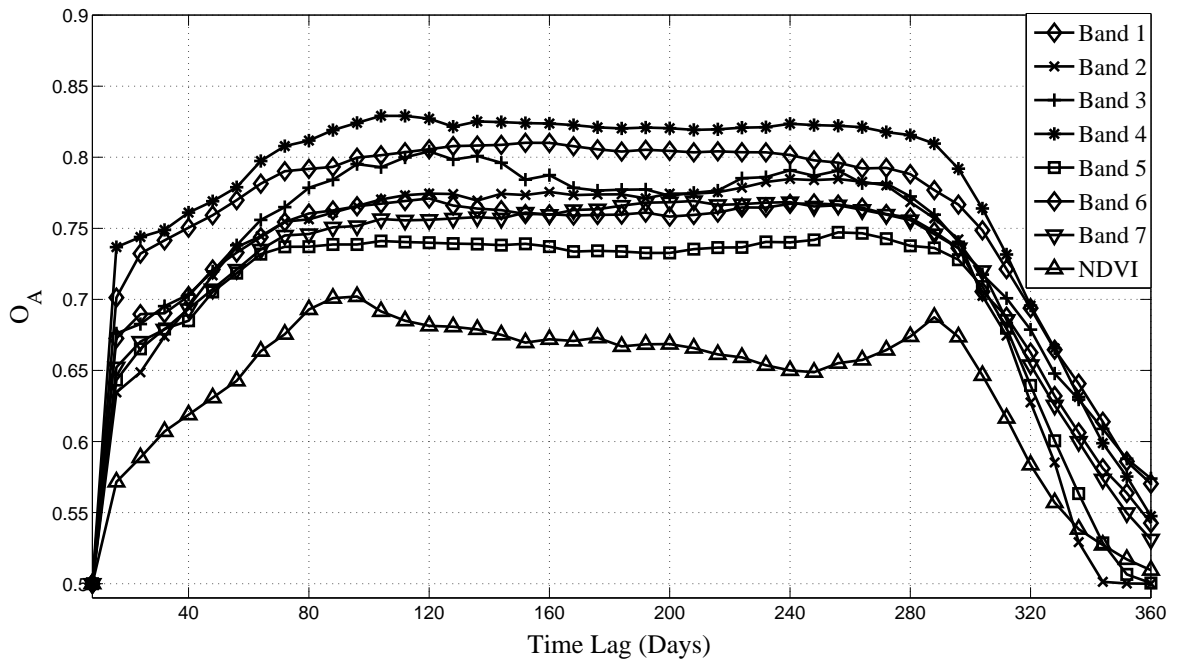
FIGURE 6.9: Overall accuracy of the ACF method computed for a range of band and lag combinations using a no-change and simulated change dataset for the Limpopo province.

$$\text{Change} = \begin{cases} \text{true} & \text{if } R^b(\tau) \geq 0.13 \\ \text{false} & \text{if } R^b(\tau) < 0.13. \end{cases}$$

Table 6.8 summarizes the performance of the method using the parameters obtained during the off-line optimization phase.

Table 6.8: Confusion Matrix, overall accuracy (O_A) and threshold (δ) for the case of real change detection using the MODIS band 4 *(550 nm)* with a lag of 104 days as determined during the ACF method's off-line optimization phase. Value in parentheses indicates the standard deviation.

	Real change (n=117)	No Change (n=1616)	δ	O_A
Change Detected	81.20% (2.7%)	12.00% (1.1%)	0.13 (0.01)	84.60% (2%)
No Change Detected	18.80% (2.7%)	88.00% (1.1%)		

Table 6.9: Confusion matrix of the NDVI differencing method using a fixed and optimal threshold for the Limpopo province. Value in parentheses indicates the standard deviation.

	Real change (n=117)	No Change (n=1616)	z	O_A
Fixed false alarm rate			2.1	77.79% (1.8%)
Change Detected	69.00% (3.7%)	13.00% (1.0%)		
No Change Detected	31.00% (3.7%)	87.00% (1.0%)		
Optimal Threshold			1.6 (0.2)	79.21% (1.3%)
Change Detected	83.76% (4.7%)	25.34% (4.1%)		
No Change Detected	16.24% (4.7%)	15.40% (4.1%)		

6.3.3 Evaluation of the NDVI differencing method in Limpopo

Using the methodology given in section 5.4, the NDVI differencing change detection method was applied in the Limpopo province, Table 6.9 shows the performance of the method using an optimal threshold as well as the threshold corresponding to a constant false alarm rate of 13%. To get an indication of the NDVI method's performance as a function of z, the false alarm rate and change detection accuracy was calculated for a series of z values ranging from 1 to 3.5 (figure 6.10). The optimal threshold (z^*) and the threshold corresponding to a false alarm rate of 13% (z) is indicated on the false alarm rate curve.

6.4 DETECTING LAND-COVER CHANGE IN THE GAUTENG PROVINCE OF SOUTH AFRICA

The Gauteng province is located in northern South Africa, because of a high level of urbanization it has seen significant human settlement expansion during the 2001 and 2008 period. A total area of approximately 17 000 km^2 was considered being centered around $26°07'29.62''$S, $28°05'40.40''$E. Figure 6.11 shows the location of the Gauteng province in South Africa. Gauteng is the smallest province in South Africa, occupying a land area of only 1.4% of the land area of the country, but it is highly urbanized as it contains two of the largest cities in South Africa, Johannesburg and Pretoria.

A total of 592 examples of natural vegetation, 372 examples of settlement and 181 examples of real change 500 m MODIS pixels were identified within the study area. Landsat and SPOT high resolution
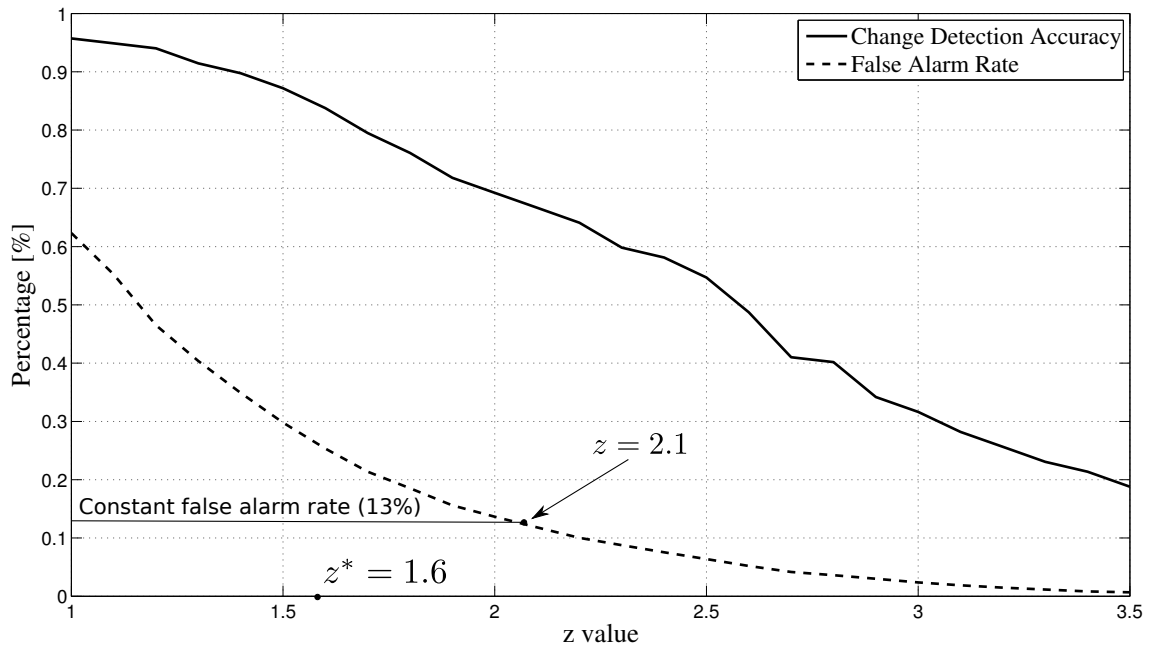
FIGURE 6.10: NDVI differencing method's change detection accuracy and false alarm rate for a range of z values in Limpopo.

data were used to identify the aforementioned pixels as described in section 6.1.

6.4.1 Evaluation of the EKF change detection method in Gauteng

6.4.1.1 Off-line optimization of the EKF method in Gauteng

The simulated change dataset was also generated using the methodology proposed in section 5.2.2. In this case, 296 pixels in the natural vegetation dataset were used to generate the simulated dataset. The value of δ^* (as described in section 5.2.2) is shown for 6, 12 and 24 month simulated blending periods in tables 6.10, 6.11 and 6.12 respectively. The value of δ^* varied between 2.5 and 1.91 with a corresponding false alarm rate being between 3.62% and 16.05% respectively. As in the previous study area, a maximum false alarm rate was chosen to be 13%. Substituting these values in Equation 5.11

$$\widehat{\delta} = \delta^* \ \ \text{where} \int_{\delta=\delta^*}^{\delta=\infty} p(\delta|\overline{C}) = 13\% \ \ \delta^* \in [1.91, 2.5], \tag{6.9}$$

$\widehat{\delta}$ was calculated as 1.975.

Table 6.10: Land-cover change detection accuracy, false alarm rate and optimal threshold (δ^*) for a range of pixels having changed in the 3×3 pixel grid using the EKF change detection method in Gauteng. The simulated change had a 6-month blending period and the value in parentheses indicates the standard deviation.

Number of pixels changed in 3×3 grid	Detection accuracy	False alarm rate	δ^*
1	99.29% (0.40%)	3.33% (0.59%)	2.49 (0.06)
2	99.23% (0.34%)	3.15% (0.56%)	2.49 (0.04)
3	99.44% (0.43%)	3.63% (0.60%)	2.45 (0.04)
4	98.86% (0.32%)	4.17% (0.73%)	2.44 (0.03)
5	98.09% (0.67%)	4.88% (1.03%)	2.36 (0.05)
6	98.26% (0.97%)	7.26% (1.03%)	2.22 (0.03)
7	98.52% (0.37%)	8.69% (0.80%)	2.14 (0.02)
8	97.11% (0.75%)	9.32% (1.45%)	2.09 (0.02)
9	95.14% (0.84%)	11.39% (1.07%)	2.02 (0.01)

Table 6.11: Land-cover change detection accuracy, false alarm rate and optimal threshold (δ^*) for a range of pixels having changed in the 3×3 pixel grid using the EKF change detection method in Gauteng. The simulated change had a 12-month blending period and the value in parentheses indicates the standard deviation.

Number of pixels changed in 3×3 grid	Detection accuracy	False alarm rate	δ^*
1	99.44% (0.38%)	3.62% (0.79%)	2.50 (0.04)
2	99.29% (0.40%)	3.76% (0.82%)	2.42 (0.05)
3	99.29% (0.41%)	4.24% (0.39%)	2.38 (0.04)
4	98.99% (0.49%)	4.45% (0.73%)	2.37 (0.05)
5	98.29% (0.65%)	5.98% (0.73%)	2.28 (0.04)
6	98.44% (0.63%)	8.18% (0.83%)	2.16 (0.04)
7	98.24% (0.49%)	8.89% (0.66%)	2.10 (0.02)
8	97.37% (0.75%)	10.28% (0.85%)	2.05 (0.03)
9	94.58% (0.94%)	12.79% (1.07%)	1.97 (0.02)
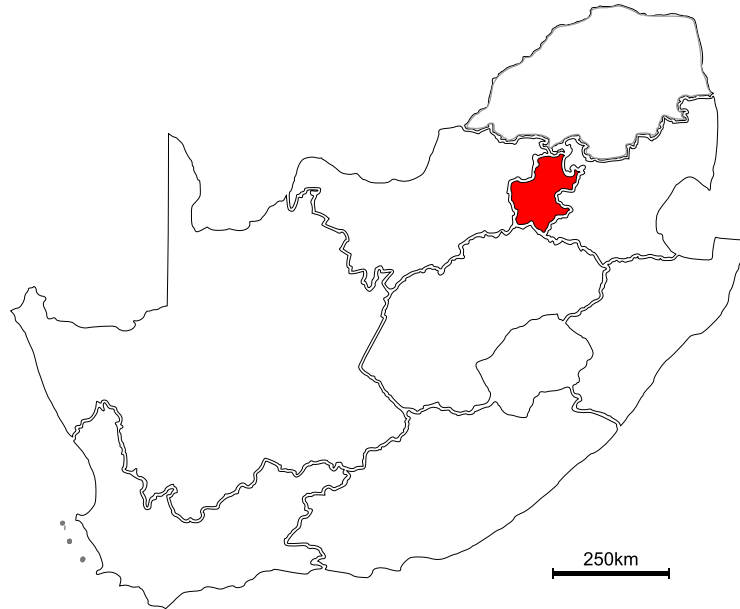
FIGURE 6.11: Location of the Gauteng province in South Africa.

6.4.1.2 Real change detection performance of the EKF method in Gauteng

Substituting the value of $\widehat{\delta}$ yields,

$$
\text{Change} = \begin{cases} \text{true} & \text{if } \delta \geq 1.97 \\ \text{false} & \text{if } \delta < 1.97. \end{cases}
$$

The change detection accuracy using the threshold of 1.97 was 75% using the 181 examples of real change in the study area. The false alarm rate was 12.75%.

6.4.2 Evaluation of the temporal ACF change detection method in Gauteng

6.4.2.1 Off-line optimization of the ACF method in Gauteng

Of the available 592 examples of natural vegetation and 372 settlement pixels, 592 simulated change pixels were generated. From the total of 964 no-change pixels, a random selection of 482 pixels were used during the off-line optimization phase with the remainder (482 pixels) being used to infer the false alarm rate performance during the real change detection phase.

Table 6.12: Land-cover change detection accuracy, false alarm rate and optimal threshold (δ^*) for a range of pixels having changed in the 3×3 pixel grid using the EKF change detection method in Gauteng. The simulated change had a 24-month blending period and the value in parentheses indicates the standard deviation.

Number of pixels changed in 3×3 grid	Detection accuracy	False alarm rate	δ^*
1	99.25% (0.48%)	4.50% (0.77%)	2.40 (0.04)
2	99.29% (0.35%)	4.78% (0.79%)	2.37 (0.05)
3	99.01% (0.56%)	5.28% (0.65%)	2.34 (0.04)
4	98.20% (0.82%)	5.82% (0.66%)	2.28 (0.04)
5	97.73% (0.64%)	8.51% (0.60%)	2.18 (0.03)
6	97.75% (1.09%)	9.53% (0.95%)	2.09 (0.02)
7	97.71% (0.88%)	10.53% (0.65%)	2.04 (0.03)
8	94.92% (1.55%)	12.37% (1.03%)	1.98 (0.01)
9	91.61% (0.70%)	16.05% (1.25%)	1.91 (0.02)

O_A was calculated for each band $b \in \{1, 2, ..., 8\}$ and lag $\tau \in \{1, 2, ..., 46\}$ using the aforementioned no-change and simulated change datasets (figure 6.12). It was found that the highest overall detection accuracy was obtained by using the change index $\delta_\tau^b = \delta_{12}^4 = R^4(12)$. The τ value of 12 corresponds to 96 days. The value of δ_{12}^{4*} was found to be 0.16. Table 6.13 summarizes the performance of the method when using the aforementioned parameters.

Table 6.13: Confusion Matrix, overall accuracy (O_A) and optimal threshold (δ^*) showing the best land-cover change detection performance during the ACF method's off-line optimization phase using MODIS band 4 *(550 nm)* with a lag of 96 days. Value in parentheses indicates the standard deviation.

	Simulated change (n=592)	No Change (n=482)	δ^*	O_A
Change Detected	75.17%(4.0%)	14.73% (1.6%)	0.16 (0.01)	80.22% (2%)
No Change Detected	24.83% (4.0%)	85.27% (1.6%)		
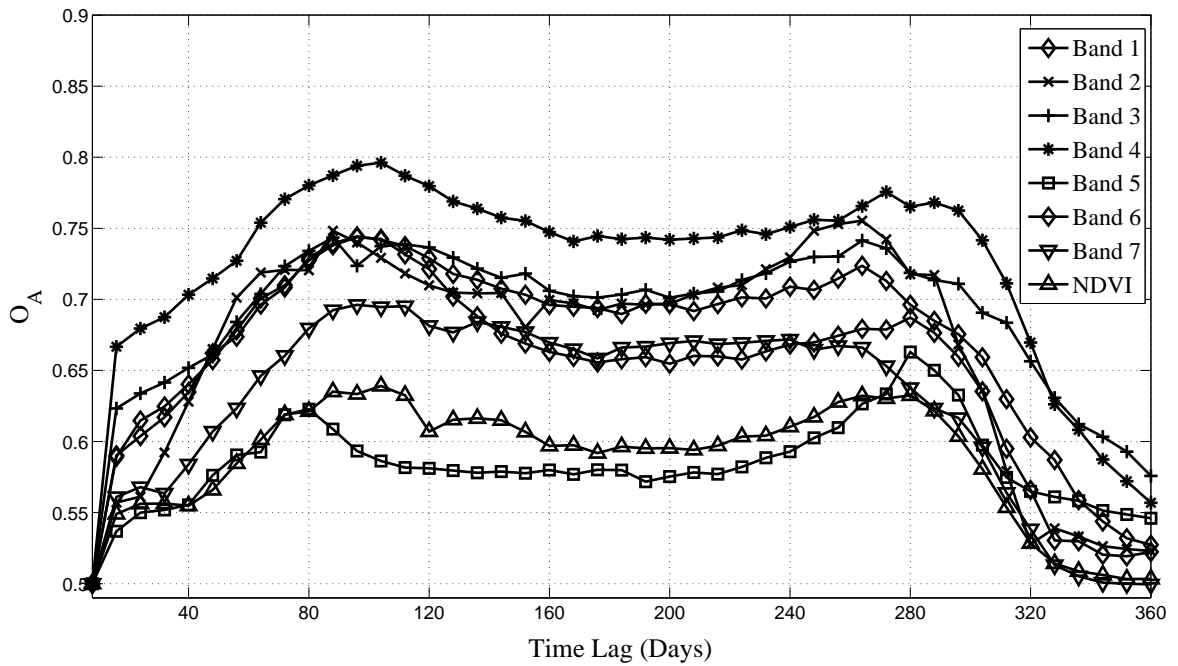
FIGURE 6.12: Overall accuracy evaluated for a range of band and lag combinations using a no-change and simulated change dataset for the Gauteng province.

6.4.2.2   Real change detection performance of the ACF method in Gauteng

After the band, lag and optimal threshold selection was completed, the performance of the proposed method was validated using the no-change and real change datasets. A change or no-change decision for each pixel was obtained by evaluating

$$\text{Change} = \begin{cases} \text{true} & \text{if } R^b(\tau) \geq 0.16 \\ \text{false} & \text{if } R^b(\tau) < 0.16. \end{cases}$$

Table 6.14 summarizes the performance of the method using the parameters obtained during the off-line optimization phase.

6.4.3   Evaluation of the NDVI differencing method in Gauteng

Using the methodology given in section 5.4, the NDVI difference change detection method was used in the Gauteng province, Table 6.15 shows the performance of the method at the optimal threshold as well as the threshold corresponding to a constant false alarm rate of 13%. Figure 6.13 shows the false alarm rate and change detection accuracy as a function of the z value.

Table 6.14: Confusion Matrix, overall accuracy (O_A) and threshold (δ) for the case of real change detection using the MODIS band 4 *(550 nm)* with a lag of 96 days as determined during the ACF method's off-line optimization phase. Value in parentheses indicates the standard deviation.

	Real change (n=181)	No Change (n=482)	δ	O_A
Change Detected	92.27% (4.5%)	15.35% (1.9%)	0.16 (0.02)	88.46% (3%)
No Change Detected	7.73% (4.5%)	84.65% (1.9%)		

Table 6.15: Confusion matrix of the NDVI differencing method using a fixed and optimal threshold for the Gauteng province. Value in parentheses indicates the standard deviation.

	Real change (n=181)	No Change (n=482)	z	O_A
Fixed false alarm rate				
Change Detected	56.91% (4.5%)	13.51% (1.0%)	1.8	71.70% (2.2%)
No Change Detected	43.09% (4.5%)	86.49% (1.0%)		
Optimal Threshold				
Change Detected	78.45% (4.2%)	26.27% (5.2%)	1.4 (0.11)	76.09% (1.7%)
No Change Detected	21.55%(4.2%)	73.73% (5.2%)		
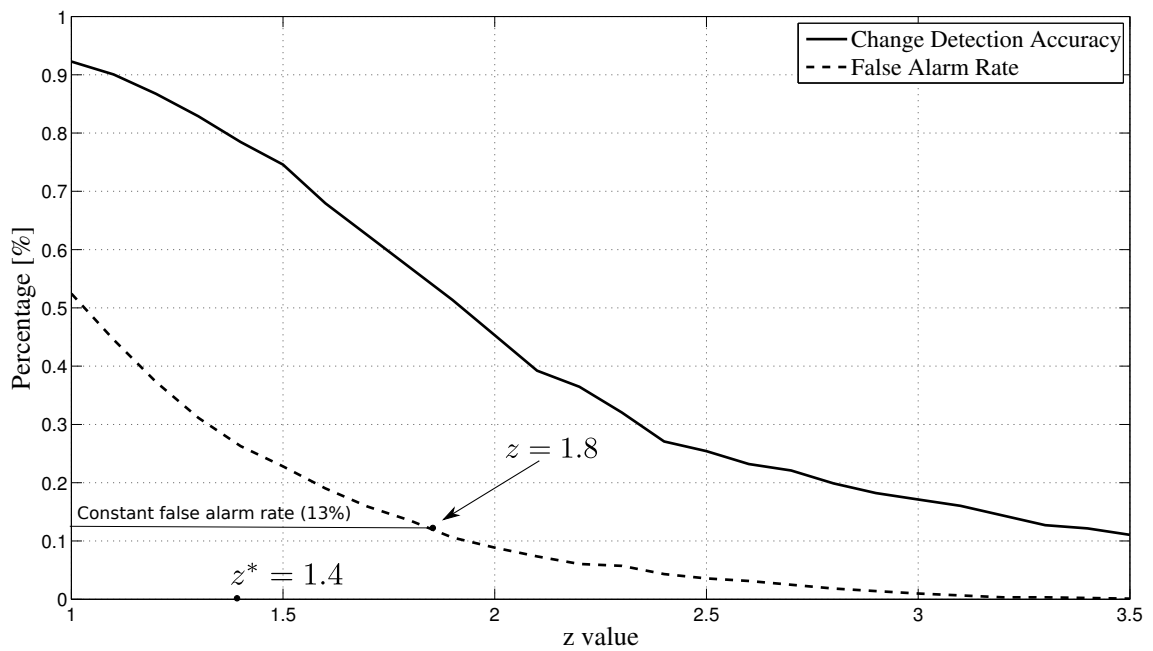
FIGURE 6.13: NDVI differencing method's change detection accuracy and false alarm rate for a range of z values in Gauteng.

6.5   DISCUSSION OF THE CHANGE DETECTION METHODS

Table 6.16 gives a performance comparison of all the methods presented in this chapter. The threshold was selected so that the false alarm rate is within the $10\% - 15\%$ range to enable a fair comparison of all three methods. The following section will discuss the results obtained using each of these methods for the case of real change detection in greater detail.

6.5.1   Discussion of the EKF change detection method results

From Table 6.16 it is evident that the performance of the EKF method is acceptable in both provinces, achieving more than a 75% detection accuracy with the false alarm rate being less than 15% for each of the areas. The performance of the method is, however, better in the Limpopo region. The reason for this could be that the Limpopo province is mostly covered by natural vegetation which implies an inherent high correlation between pixels when considering a 3×3 pixel grid in a natural vegetation area. As was shown in tables 6.10, 6.11 and 6.12, the method performs best when fewer pixels in the 3×3 grid change, for example, 7.92% with only the center pixel changing versus 18.83% with all 9 pixels changing in the case of a 6-month simulated land cover change (Table 6.10). The conclusion can thus be drawn that the EKF method performs best in an environment where most of the pixels in

Table 6.16: Summary of real change detection results. Value in parentheses indicates the standard deviation.

Algorithm	No. of Real Change Pixels	% Change Correctly Detected	% False Alarms	Threshold
Limpopo Province				
EKF method	117	89% (2.8%)	13% (0.98%)	$\delta = 1.5$
ACF method	117	81% (4.5%)	12% (1.9%)	$\delta = 0.13$
NDVI Differencing method [17]	117	69% (3.7%)	13% (1.0%)	$z = 2.1$
Gauteng Province				
EKF method	181	75% (2.9%)	13% (0.9%)	$\delta = 1.97$
ACF method	181	92% (2.7%)	15% (1.1%)	$\delta = 0.16$
NDVI Differencing method [17]	181	57% (4.5%)	14% (1.3%)	$z = 1.8$

the 3×3 pixel grid are highly correlated. This was found to be the case in Limpopo as the province is mostly covered by natural vegetation. A typical 3×3 grid of pixels in Limpopo thus have a high probability of having the same land-cover type and consequently a high correlation when considering the EKF derived parameter sequences. In the case of Gauteng, being the smallest province with the highest population, the landscape is much more diverse. A typical 3×3 grid of pixels, which corresponds to an area of 2.25 km^2, has a much higher probability of having de-correlated pixels and subsequently, the method's performance in this area was compromised. To test this hypothesis, the standard deviation between the center pixel and neighboring pixels of a 3×3 pixel grid was calculated for all the pixels in the Limpopo and Gauteng study area. The underlying idea is that a low standard deviation would indicate that the grid area is more homogeneous than a pixel grid having a high standard deviation. A summer MODIS image over the Limpopo and Gauteng study area was used for the experiment. As expected, it was found that Gauteng had a 15% increase in the standard deviation relative to Limpopo. This finding was also supported when considering the bio-diversity in both study areas (Figure 6.15).

In an effort to determine the stability of the false alarm rate as a function of the region size, the EKF method was run blindly, i.e. without having any knowledge of the land cover type or usage, over a 70 km radius from the center of each study area in the Limpopo and Gauteng provinces (Figure
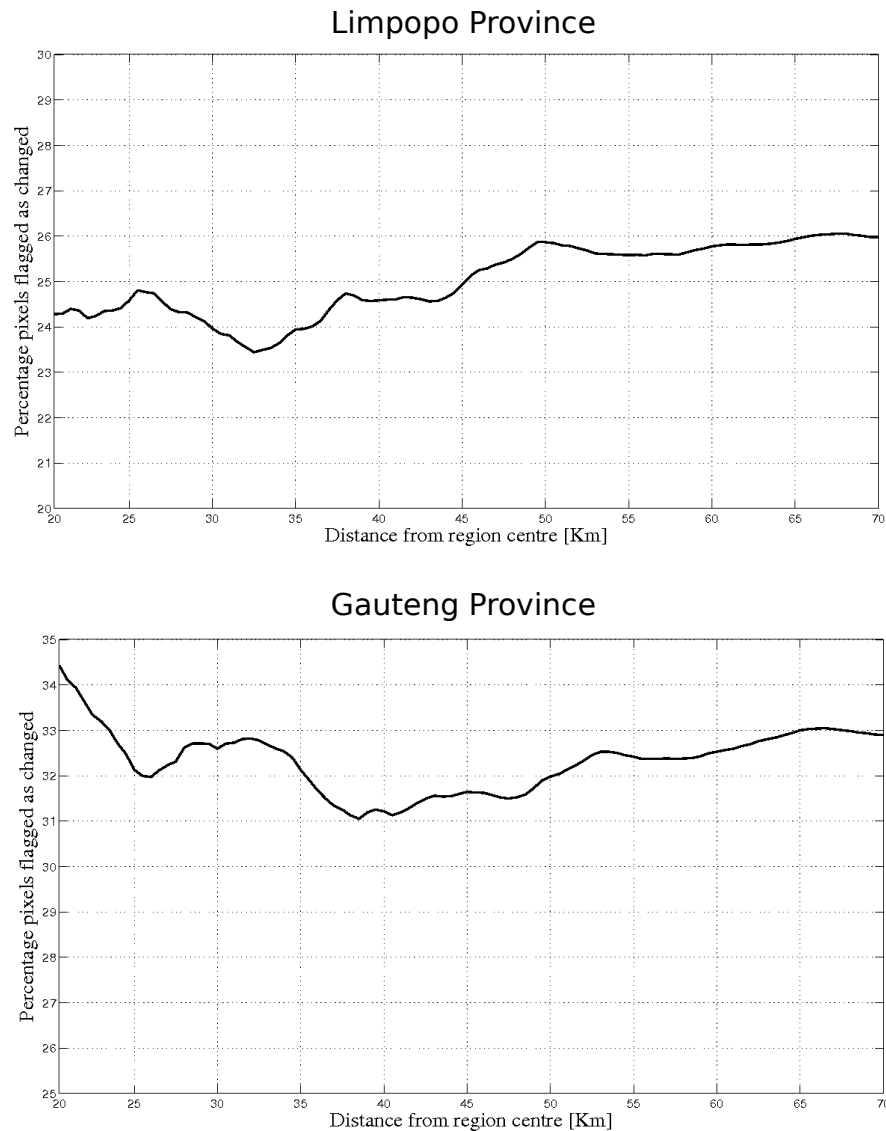
FIGURE 6.14: Percentage pixels flagged as changed as a function of the distance from the center of each region.

6.14). The rationale behind this experiment is that, with all other parameters being kept constant, there will be a dramatic change in the percentage pixels flagged as having changed if the threshold, which determines the false alarm rate, becomes invalid when increasing the radius of the operation. It is evident that the percentage pixels having changed does not vary significantly as a function of the distance from the region center, having a standard deviation of roughly 1% for both the Limpopo and Gauteng province. The 70 km radius was postulated to be representative when considering the bio-regions found in South Africa which are typically less than 140 km in diameter (Figure 6.15). Bio-regions are characteristic flora, fauna, and environmental conditions and as such would have to be taken into consideration when determining the threshold for operational use.
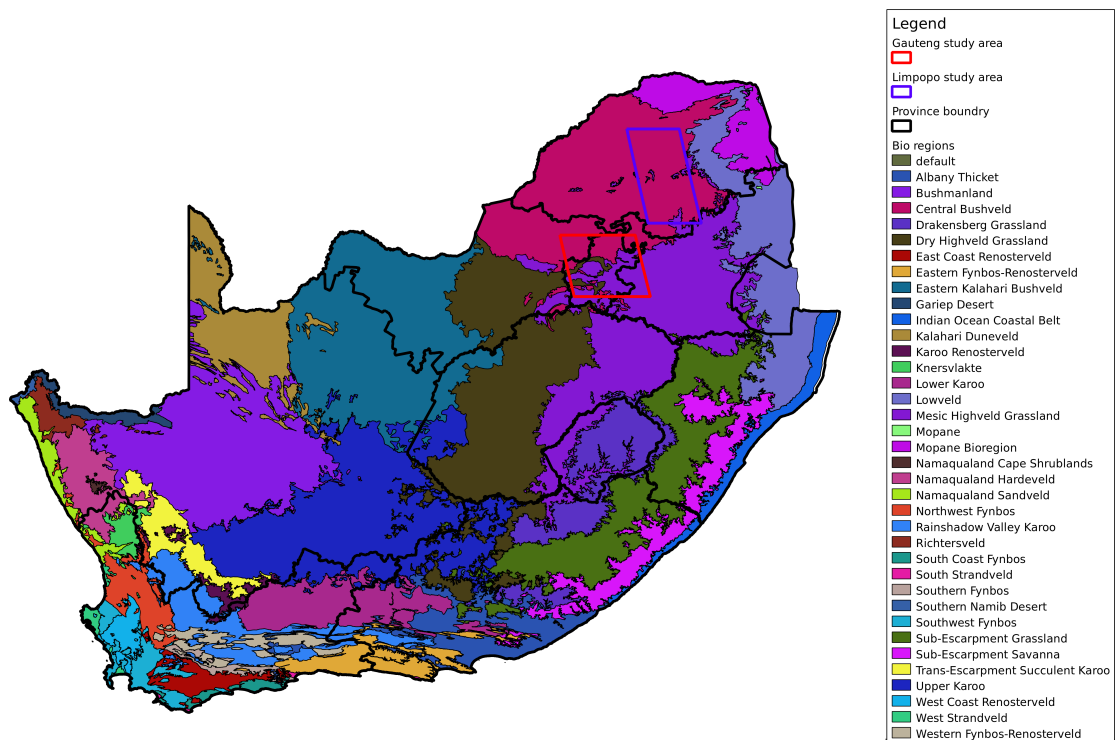
FIGURE 6.15: Location of the Gauteng and Limpopo study areas as well as the bio-regions found in South Africa.

Another interesting point is that the number of pixels having been flagged as changed which ranged between 24% and 34%. The false alarm rate in the study area using the predetermined threshold was found to be less than 14% (Table 6.16) in both provinces which raises the question of the source of the remaining 10 to 20%. One obvious source of the additional pixels being flagged as change, other than the false alarms, are pixels that did in fact change from a natural vegetation to settlement land cover and were consequently detected as having changed. As this type of change is a relatively rare event in a regional landscape (typically 4% according to F. Schoeman *et al.* [67]), it is highly unlikely that this is the only source of the additional percentage difference. It is safe to assume that land cover change from natural vegetation to settlement in both provinces is not the only type of land cover change possibility which implies that the additional 6 to 16% of pixels flagged as changed could be because of a host of other changes which could include, for example, agriculture, mining, deforestation, etc. It is very probable that the EKF change detection method was sensitive to these types of changes as well which could have resulted in the higher than expected number of pixels flagged as having changed. There is also a strong possibility that the EKF method could be sensitive to other land cover types, for example, water. Sensitivity for various types of land cover changes is advantageous when using the method as a change alarm, this thesis only considered settlement expansion as an example but the

Limpopo Province

Gauteng Province
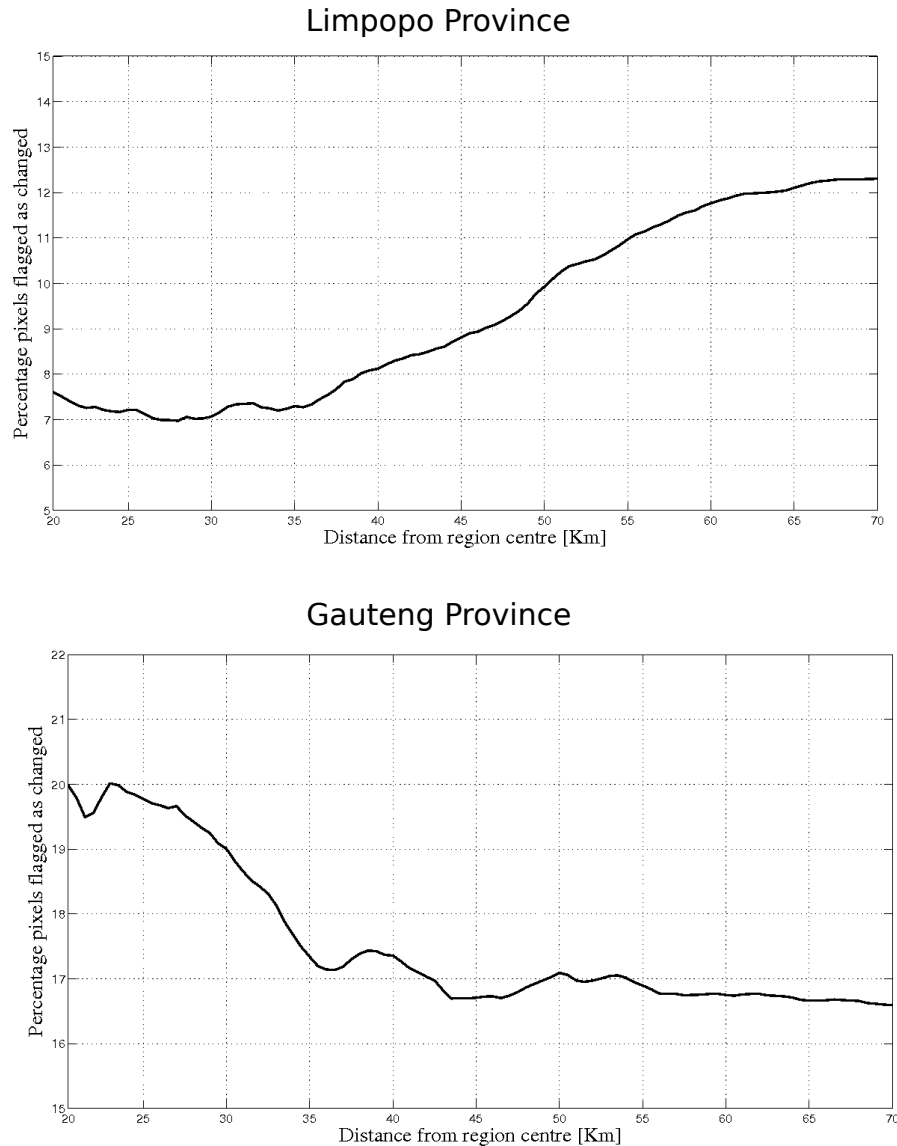
FIGURE 6.16: Percentage pixels flagged as changed using the ACF method as a function of the distance from the center of each region.

detection capability of the method to other land cover changes, for example deforestation is definitely a topic for further investigation (see section 7.2).

6.5.2 Discussion of the temporal ACF change detection method results

The ACF method performance is also acceptable, achieving more than an 80% detection accuracy with the false alarm being 15 % or lower for both provinces (Table 6.16). As opposed to the results obtained by the EKF change detection method, the performance of the temporal ACF change detection method is better for the Gauteng province than the Limpopo province. The performance of the false alarm rate of the temporal ACF change detection method in Limpopo is very similar for the

TABLE 6.17: O_A performance for different start of change dates.

Mean start of change	O_A
2001/06	70.67%
2002/06	83.57%
2003/06	85.33%
2004/06	85.43%
2005/06	84.92%
2006/06	81.74%
2007/06	76.66%

off-line optimization and operational phase being 12% and 12.25% respectively. The change detection accuracy for the corresponding areas were 78.16% and 81.20% respectively (Tables 6.7 and 6.8) which is also relatively similar. In the Gauteng province the false alarm rate for both the off-line optimization and operational phase was again very similar (14.73% and 15.35%), but the change detection accuracy was considerably different (75.17% and 92.27%). It might seem counterintuitive that the simulated change is more difficult to detect than real change examples in the Gauteng province, but this does make sense when considering the timing of the change. The mean start of change date of the real change dataset in Gauteng is 2004 with a standard deviation of two years. The simulated change date, on the other hand, was distributed uniformly over the entire date range of the time-series. Therefore, when the change occurs in the center of the time-series, the non-stationarity of the time-series will be at a maximum and will decrease as the change date moves towards the beginning or end of the time-series. The performance of the method for detecting simulated change is shown for different start years (Table 6.17). It is clear that the ACF change detection method is slightly compromised when change occurs in the first or last year with no significant decrease in the performance for the others years. Unfortunately, no change date information was available in the Limpopo province, only images at the start and end of the time-series. It is, however, very probable that the change date in Limpopo was distributed more uniformly over the study period, which resulted in the higher correlation between that simulated change and real change detection performance.

Combining multiple bands in this study did not significantly improve on the separability achieved using only band 4. This does not suggest that band 4 is the best for all types of land-cover change.

However, for our study area and land-cover change case, the ACF of the band 4 time-series showed the highest separability between the no-change and simulated change datasets. Multiple band combinations could also be used to improve the separability at the cost of increased computational complexity in cases where no single band gives adequate separability.

The stability of the false alarm rate for the ACF method was also evaluated as a function of the region size. Similar to the experiment shown in section 6.5.1, the ACF method was run blindly over a 70 km radius from the center of each study area in the Limpopo and Gauteng provinces (Figure 6.16). Although there was slightly more variation in the percentage pixels having changed compared to the EKF method, the ACF method does not vary significantly as a function of the distance from the region center, having a standard deviation of roughly 2% for both the Limpopo and Gauteng province. As with the corresponding experiment in the case of the EKF method, some interesting results where observed when considering the percentage of pixels flagged as having changed. The percentage of pixels flagged as having changed varied between 7 and 20%, which is much lower than the corresponding results obtained using the EKF method. The difference between the false alarm rate of less than 15% in both of the study regions (table 6.16) to that of the number of pixels flagged as having changed in the 'blind run' experiment is much smaller which indicates that the ACF method is potentially not so sensitive to other types of land cover changes using the parameters derived during the off-line optimization phase which made use of the simulated change and no-change datasets of natural vegetation and settlement land cover types.

6.5.3   Discussion of the NDVI differencing method

The NDVI differencing method, proposed in [17],was found not to be very successful, having a change detection accuracy of less than 70% in the false alarm region of 15% and less for both study areas (Table 6.16). A possible explanation for this is that because the NDVI differencing method assumes that the annual NDVI difference is distributed normally, the method could have difficulty in detecting land-cover change when the study area is heterogeneous and consequently compromises the normality assumption that is fundamental to this method. As expected, the method performs the poorest in the Gauteng province because of the land-cover diversity of the area (see figure 6.15). The method does perform better in the Limpopo province, but still has a change detection accuracy performance decrease of 20% when compared to the EKF change detection method at the same false alarm rate. The NDVI differencing method also reduces the eight day composited time-series over the seven-year period to an effective seven observations by only considering the total annual NDVI value for each year. This reduces the information available for change detection considerably. The threshold value

that corresponded with a false alarm rate in the region of 13% was between 1.8 and 2.1 (see figures 6.10 and 6.13) with the change detection accuracy being less than 70% in both cases. These results correspond well to those reported by Lunetta *et al.* for non-agricultural areas in the Albemarle-Pamlico estuary system (APES) located in North Carolina and Virginia in the United States. For their study, a threshold value of 2 resulted in a change detection accuracy of 68% with a false alarm rate of 15% [17].

6.6   CONCLUSION

In this chapter, the performance of three change detection methods was presented. Firstly, as a buildup to the EKF change detection framework, it was shown that that the separation between natural vegetation and settlement land-cover types can be improved over FFT separation by using an EKF (Section 6.2.2). After EKF separability between natural and settlement time-series data was determined, the method was adapted to the change detection case by formulating a change metric that is based on a comparison of the μ and α parameter sequences of a pixel to the EKF derived parameter sequences of its neighboring pixels. The EKF change detection method was used to detect new settlement developments in the Limpopo and Gauteng provinces of South Africa (section 6.3.1 and 6.4.1).

The second method that was proposed was the temporal ACF change detection method. The temporal ACF was used to exploit the non-stationarity of change pixels relative to no-change pixels by using the correlation coefficient of a pre-determined band and lag combination as a change metric. The method was also used to detect new settlement developments in both provinces (section 6.3.2 and 6.4.2). Both these methods were compared to a recently published change detection method that uses NDVI differencing to determine land-cover change. The performance of this method is also given for both provinces (section 6.3.3 and 6.4.3).

It was found that the EKF change detection method performed best in the Limpopo province. This was attributed to the fact that most of the province is covered by natural vegetation which resulted in a high correlation between the EKF derived parameter sequences of neighboring pixels in a typical 3×3 pixel grid. The neighboring pixel parameter sequences could thus be utilized when calculating the change metric. Even though the settlements are low density and have a high component of vegetation, the relative difference in the EKF parameter steams of the change pixel and its neighboring pixels was high enough to detect change. In the Gauteng province the performance of the EKF method was lower. This was attributed to the land-cover diversity that is typical to this province; the 3×3 pixel grid was not as highly correlated as in the Limpopo province, which translated into a subsequent

performance degradation. It is concluded that EKF change detection can effectively exploit the additional information provided by neighboring pixels when the area that is considered is relatively homogeneous for a typical 2.25 km^2 area and the number of contiguous pixels having changed is limited to 4 or 5.

It was found that the temporal ACF change detection method had the best performance in the Gauteng province. The non-stationarity of the change pixels relative to the no-change pixel time-series was effectively exploited. The method considered a single pixel time-series as opposed to a grid of pixels as in the EKF change detection method and was therefore not influenced by heterogeneity of the pixel grid. It was shown that the change detection accuracy of the temporal ACF method is at a maximum when the change date is at the center of the time-series and slightly compromised as the change date moves towards the beginning or end of the time-series. However, the method was able to achieve more than an 80% detection accuracy in both provinces. It is concluded that the temporal ACF change detection method is very robust as it only considers the ACF of a single pixel time-series and is not dependent on the homogeneity of the considered area. The timing of the change should, however, also be considered when most of the change is anticipated to be at the end or start of the time-series. Both the proposed methods performed well for both provinces when compared to a simple NDVI differencing method.

CHAPTER SEVEN

CONCLUSION AND FUTURE RESEARCH

7.1 CONCLUDING REMARKS

The most pervasive form of land cover change in South Africa is informal human settlement expansion. It was shown in chapter 1 that determining where and when new informal settlements occur is beneficial from both an ecological as well as a social development perspective. The problem, however, is that these settlements are infrequently mapped in South Africa and that there exists a need to determine the location of these settlements in a timely and cost-effective manner. The primary objective of this thesis was to develop and test an automated change detection framework that is able to detect the transformation of natural vegetation to human settlement which could be adapted to consider many other types of land cover change as part of an ongoing endeavor towards developing a global or regional automated land cover change detection method. Two novel change detection methods were formulated to solve the aforementioned problem. Both of these methods utilize the hyper-temporal time-series data that are available from coarse resolution imagery. The novelty of these methods is underpinned by the fact that the temporal dimension of the time-series is considered as a highly sampled (relative to the natural phenological variation) data-sequence, and change classification is done by combining standard signal processing based methods for feature extraction with machine learning methods for change classification.

Human operator-dependent change mapping was found to be very time consuming and resource intensive. It follows that for large areas to be processed, a need exists to detect new settlement developments in an automated way. It was proposed in this thesis that a remote sensing approach be used to detect the formation of new settlements. Coarse resolution remotely-sensed data were found to provide an effective manner to monitor large areas on a frequent basis as the wide swath-width of coarse resolution sensors enables the same area to be observed at a very high temporal sampling rate

(hyper-temporal) as opposed to the lower revisit frequency typically associated with high resolution imagery.

When considering current change detection methods in literature, it was found that the majority of methods are based on multi-date high resolution data (in most cases only two images are used) for change detection [14, 15]. In the case where hyper-temporal data were used, change metrics were derived, giving an indication of the change intensity [16, 17, 19, 80]. A threshold-based approach was mostly used, i.e. the change metric is compared to a pre-defined threshold to infer a change or no-change decision. It was found that the change metric that is used by most of these methods is based on the annual statistics of the underlying hyper-temporal time-series and effectively reduced the hyper-temporal time-series to only a few observations. This approach fails to exploit the valuable temporal components (e.g. phase or frequency modulation, etc.) of the signal which is driven by seasonal changes in land surface phenology. The threshold selection procedure that is usually used is based on expert *a-priori* knowledge of the area. In addition, many of these methods identify large-scale ecosystem disturbances as opposed to the relatively small spatial extent of a new settlement development (resulting in but a few contiguous MODIS pixels). It follows that a novel change detection strategy had to be formulated for detecting new settlement developments using hyper-temporal satellite time-series data. When considering the objective of this thesis, the NDVI differencing method, with its statistical threshold selection methodology [17] (Section 2.7.1) was found to be the most comparable method in current literature and was consequently used for comparison with the novel change detection methods proposed in this thesis.

One of the major challenges in formulating a novel change detection method for new settlement detection was the lack of change examples, which results from the fact that regional anthropogenic land cover change is a relatively rare event in a regional landscape and that settlements are infrequently mapped in South Africa. An intuitive solution is to opt for a fully unsupervised approach which does not require any ground truth. The problem, however, is selecting suitable thresholds. The saying: *"just because everything is different doesn't mean anything has changed – Irene Peter"*, is very relevant when considering this change detection problem. Differentiating real change from natural variations in the spectral signature using a completely unsupervised approach proved to be a very difficult task as there are still no operational MODIS land-cover change detection products available, even though more than a decade has passed since the launch of MODIS. A more practical solution is to use all ground truth, even in the absence of real change examples. This forces one to look at the specific problem from another angle. The fact that anthropogenic change is a rare event in a regional landscape

implies that no-change is a very common event in a regional landscape. It follows that obtaining no-change examples is a simple task. To address this problem, change examples were simulated by blending a time-series from a natural vegetation to a settlement state using representative time-series examples of each of these land cover types.

The objective that was set out at the beginning of this thesis was to make use of coarse resolution satellite data to infer the location of new settlement developments in an automated manner by employing machine-learning methods and subsequently two novel change detection methods were presented. The first method is based on a spatial comparison of parameter sequences derived using an EKF framework. The EKF change detection method was used to detect new settlement developments in the Limpopo and Gauteng provinces of South Africa (section 6.3.1 and 6.4.1). The second method that was proposed was the temporal ACF change detection method where the temporal ACF was used to exploit the non-stationarity of change pixels relative to no-change pixels by using the correlation coefficient of a pre-determined band and lag combination as a change metric. The method was also used to detect new settlement developments in both provinces (section 6.3.2 and 6.4.2). Both methods were compared to a recently published change detection method that uses NDVI differencing to detect land cover change. The performance of this method is also given for both provinces (section 6.3.3 and 6.4.3) where it was found that the EKF change detection method performed best in the Limpopo province (89% change detection accuracy with a false alarm rate of 13%) whereas the temporal ACF change detection method had the best performance in the Gauteng province (92% change detection accuracy with a false alarm rate of 15%). Both the proposed methods performed well when compared to the NDVI differencing method proposed in [17].

Although some MODIS change detection products do exist (such as MODIS burn-scar detection [82]), there are currently no operational MODIS products available specifically for land cover change detection, even though land cover change detection was one of the primary objectives of the MODIS mission [48]. Two previous attempts to implement an automated MODIS land cover change product as an operational system [12, 83] was not very successful, making automated land change detection using MODIS data an ongoing endeavor.

When considering the methodology for creating an automated MODIS land cover change detection framework there are a few considerations. In light of this study, it is the view of the author that unsupervised threshold based large scale land cover change detection using a completely unsupervised approach is not feasible. To illustrate this, one only has to consider the threshold values corresponding

to a similar false alarm rate for both methods in the two study areas. For example, the threshold value selected for the EKF method corresponding to a false alarm rate of 13% in Limpopo was 1.5 whereas the threshold corresponding to a similar false alarm rate in Gauteng was 1.97. Although it was shown that the threshold value produced a stable false alarm rate in a 70 km radius from the study area center, this does not imply that the threshold value will be valid over large areas spanning multiple bio-regions. The difference in the false alarm rate for the aforementioned example relates to the inherent difference in natural vegetation in both study areas which implies that blindly running the method in both regions without taking into consideration representative no-change examples is not advisable.

A better approach is to determine the most applicable land cover changes to be detected and select the appropriate system parameters to detect these specific changes. This is in line with the change detection philosophy adopted in this thesis. The two proposed methods lend themselves to operational viability by determining appropriate parameters for specific land cover change events. This is accomplished by making use of no-change examples of the two land cover types involved in the land cover change and simulating the corresponding land cover change.

When considering the operational viability of the two methods presented in this thesis a few interesting conclusions can be made. When practically implementing the EKF method, it is important that the following be taken into consideration. The EKF method utilizes a 3×3 pixel grid when determining the change metric. The advantage of this approach is that in the case of a homogeneous area and changes in the order of less than 4 contiguous MODIS pixels (see tables 6.4–6.4), the method effectively exploits the information from neighboring pixels in calculating the change metric. It was also found that, although the duration of the change does influence the method's performance (see tables 6.4–6.4), the exact change date does not. This implies that a change can be determined as soon as a significant difference in the parameter sequences of the center pixel and neighboring pixels are detected. The disadvantage of the EKF method is that when neighboring pixels are no longer correlated with the center pixel the performance of the method deteriorates, as was found to be the case in the Gauteng study area. The method should thus operate well in homogeneous areas where a simultaneous change is typically in the order of less than 4 contiguous MODIS pixels and where representative "no-change" examples of the land cover types in question are available.

In the case of practical implementation of the ACF method, the following should be taken into consideration. The advantage of the ACF method is that the method is a per pixel change detection

method and is thus not sensitive to the correlation to neighboring pixels. This implies that the homogeneity of the area will not affect the method in the same way as was found to be case for the EKF method. The ACF method utilizes all of the MODIS land bands when determining the optimal detection parameters. This makes the method more versatile than the EKF method, which only utilizes NDVI. The disadvantage of the method, however, is that the start of change date does influence the performance of the method as the change detection performance increases when the change date moves towards the center of the time-series (see table 6.17). When practically implementing the ACF method, it is advisable that the anticipated start of change date be taken into consideration when determining the time-series length of the study period. However, even when there is no *a-priori* knowledge of the start of change date and a random start of change date is assumed, the method should still perform acceptably, as was found in the simulated change experiments and real change detection performance in Limpopo.

7.2   FUTURE RESEARCH

Based on the findings of this thesis, the following areas were identified that could potentially be explored in subsequent studies.

- Currently, the distribution of the change metrics derived using the EKF and ACF change detection methods in the case of simulated change and no-change respectively is estimated by means of the Parzen-Rosenblatt window method using Gaussian kernels (see section 6.2.2). The corresponding optimal threshold is then determined by making use of these estimated distributions. An alternative approach to determining the optimal threshold could be to use a supervised classifier for example a Neural Network (NN) or Support Vector Machine (SVM) by using the change metric as input features. The use of other features as input to the aforementioned classifiers can also be investigated. For example, a selected subset of bands and lags of the ACF functions shown in section 5.3 can be used as input features to the classifier.

- The EKF change detection method currently uses a triply modulated cosine function to model the NDVI time-series and uses the non-linear EKF to track the model parameters for each time step (see section 5.2). The EKF change detection method can be adapted to use as input all seven bands. Although this would require a representative observation model to be formulated for each band, the resulting increase of tracked parameters could produce a higher change detection accuracy as the increase in usable features could produce a higher separability between change and no-change when used with a non-linear classifier, as mentioned in the previous point.

- As suggested in section 6.5.1, changes other than settlement expansion (for example deforestation) can be considered using the same methodology proposed in this thesis. Using no-change examples of representative land cover types (for example, forested and deforested regions if the aim is to determine areas affected by deforestation), the EKF change method can be adapted to detect a host of possible change events.

- An analysis could be done to determine the correlation between specific land cover types and typical false alarm rates using each of the change detection methods presented in this thesis, using this information, no-change land cover types, prone to being flagged as false alarms (for example agriculture or water), could be masked out if the algorithm is run over large areas.

- Currently, the EKF change detection method only makes use of NDVI data as input. The effect of using other vegetation indices, such as Fraction of Absorbed Photosynthetically Active Radiation (FAPAR), as input to the algorithm can also be investigated.

REFERENCES

[1] J. Foley *et al.*, "Global consequences of land use," *Science*, vol. 309, no. 5734, pp. 570–574, July 2005.

[2] R. T. Watson, *Land Use, Land-Use Change and Forestry*. Cambridge, England: Cambridge University Press, 2000.

[3] T. Karl *et al.*, "Modern global climate change," *Science*, vol. 302, no. 1719, pp. 1719–1723, Dec. 2003.

[4] (2010) State of the environment South Africa. [Online]. Available: http://soer.deat.gov.za/

[5] A. Palframan, "A syntactical analysis of settlement form an investigation of socio-spatial characteristics in low-income housing settlements in Port Elizabeth, South Africa." in *World Congress on Housing*, vol. 33, Pretoria, South Africa, Sept. 2005, pp. 3353–3355.

[6] (2010) United nations division for sustainable development - national information - South Africa. [Online]. Available: http://www.un.org/esa/agenda21/natlinfo/countr/safrica/human_settlements.pdf

[7] D. Smith, *The Apartheid City and Beyond*, 1st ed. South Africa: Witwatersrand University Press, 1992.

[8] P. Smits and A. Annoni, "Toward specification driven change detection," *IEEE Transactions on Geoscience and Remote Sensing*, vol. 38, no. 3, pp. 1484–1488, May 2000.

[9] T. R. Loveland *et al.*, "A strategy for estimating the rates of recent United States land-cover changes," *Photogrammetric Engineering and Remote Sensing*, vol. 68, no. 10, pp. 1091–1099, Oct. 2002.

[10] R. S. DeFries and J. Chan, "Multiple criteria for evaluating machine learning algorithms for land cover classification from satellite data," *Remote Sensing of Environment*, vol. 74, no. 3, pp. 503–515, Dec. 2000.

[11] T. Lillesand and R. Kiefer, *Remote Sensing and Image Interpretation*, 4th ed. New York,NY: John Wiley and Sons, 2000.

[12] X. Zhan *et al.*, "Detection of land cover changes using MODIS 250m data," *Remote Sensing of Environment*, vol. 83, no. 1-2, pp. 336–350, Nov. 2002.

[13] J. R. G. Townshend and C. Justice, "Selecting the spatial resolution of satellite sensors required for global monitoring of land transformations," *International Journal of Remote Sensing*, vol. 9, no. 2, pp. 187–236, Feb. 1988.

[14] P. Coppin *et al.*, "Digital change detection methods in ecosystem monitoring: a review," *International Journal of Remote Sensing*, vol. 24, no. 9, pp. 1565–1596, May 2004.

[15] D. Lu and Q. Weng, "A survey of image classification methods and techniques for improving classification performance," *International Journal of Remote Sensing*, vol. 28, no. 5, pp. 823–870, Jan. 2007.

[16] J. Borak, E. Lambin, and A. Strahler, "The use of temporal metrics for land cover change detection at coarse spatial scales," *International Journal of Remote Sensing*, vol. 21, no. 6, pp. 1415–1432, Apr. 2000.

[17] R. S. Lunetta, J. F. Knight, J. Ediriwickrema, J. G. Lyon, and L. D. Worthy, "Land-cover change detection using multi-temporal MODIS NDVI data," *Remote Sensing of Environment*, vol. 105, no. 2, pp. 142–154, Nov. 2006.

[18] D. J. Mildrexler, M. Zhao, and S. W. Running, "Testing a MODIS Global Disturbance Index across North America," *Remote Sensing of Environment*, vol. 113, no. 10, pp. 2103–2117, Oct. 2009.

[19] N. C. Coops, M. A. Wulder, and D. Iwanicka, "Large area monitoring with a MODIS-based Disturbance Index (DI) sensitive to annual and seasonal variations," *Remote Sensing of Environment*, vol. 113, no. 6, pp. 1250–1261, June 2009.

[20] K. de Beurs and G. Henerby, "A statistical framework for the analysis of long image time series," *International Journal of Remote Sensing*, vol. 26, no. 8, pp. 1551–1573, Apr. 2005.

[21] G. Moser, S. Serpico, and G. Vernazza, "Unsupervised change detection from multichannel SAR images," *IEEE Geoscience and Remote Sensing Letters*, vol. 4, no. 2, pp. 278–282, Apr. 2007.

[22] R. Radke, S. Andra, O. Al-Kofahi, and B. Roysam, "Image change detection algorithms: A systematic survey," *IEEE Transactions on Image Processing*, vol. 14, no. 3, pp. 294–306, Mar. 2005.

[23] F. Melgani, G. Moser, and S. B. Serpico, "Unsupervised change detection methods for remote sensing images," *Optical Engineering*, vol. 41, no. 12, pp. 3288–3297, Dec. 2002.

[24] A. Singh, "Digital change detection techniques using remotely-sensed data," *International Journal of Remote Sensing*, vol. 10, no. 6, pp. 989–1003, June 1989.

[25] L. Bruzzone and D. F. Prieto, "A minimum-cost thresholding technique for unsupervised change detection," *International Journal of Remote Sensing*, vol. 21, no. 18, pp. 3539–3544, Dec. 2000.

[26] F. Tung and E. LeDrew, "The determination of optimal threshold levels for change detection using various accuracy indexes," *Photogrammetric Engineering and Remote Sensing*, vol. 54, no. 10, pp. 1449–1454, Oct. 1988.

[27] (2010, May) MODIS products table. [Online]. Available: https://lpdaac.usgs.gov/lpdaac/products/

[28] C. Schaaf *et al.*, "First operational BRDF, albedo nadir reflectance products from MODIS," *Remote Sensing of Environment*, vol. 83, no. 1-2, pp. 135–148, Nov. 2002.

[29] J. Verbesselt, R. Hyndman, G. Newnham, and D. Culvenor, "Detecting trend and seasonal changes in satellite image time series," *Remote Sensing of Environment*, vol. 114, no. 1, pp. 106–115, Jan. 2010.

[30] P. Gibson, *Introductory Remote Sensing: Principles and Concepts*, 1st ed. New York,NY: Routledge, 2000.

[31] E. Christian, "Planning for the Global Earth Observation System of Systems (GEOSS)," *Space Policy*, vol. 21, no. 2, pp. 105–109, May 2005.

[32] D. Halliday, R. Resnick, and J. Walker, *Fundamentals of Physics*. John Wiley and Sons, 1997.

[33] E. F. Vermote and A. Vermeulen, "Atmospheric correction algorithm: Spectral reflectance (MOD09) algorithm theoretical basis document (ATBD)," *University of Maryland, Dept of Geography*, 1999.

[34] H. Ouaidrari and E. Vermote, "Operational atmospheric correction of Landsat TM data," *Remote Sensing of Environment*, vol. 70, no. 1, pp. 4–15, Oct. 1999.

[35] J. Nagol, E. Vermote, and S. Prince, "Effects of atmospheric variation on AVHRR NDVI data," *Remote Sensing of Environment*, vol. 113, no. 2, pp. 392–397, Feb. 2009.

[36] P. M. Mather, *Computer Processing of Remotely-Sensed Images: An Introduction*, 3rd ed. New York: John Wiley and Sons, 2004.

[37] (2010) File:atmospheric_electromagnetic_opacity.svg. [Online]. Available: http://en.wikipedia.org/wiki/File:Atmospheric_electromagnetic_opacity.svg

[38] E. Vermote *et al.*, "Second simulation of the satellite signal in the solar spectrum (6s), 6s user guide," in *NASA-Goddard Space Flight Center*, Greenbelt, MD,20771, USA, 2007.

[39] J. Susaki, K. Hara, K. Kajiwara, and Y. Honda, "Robust estimation of BRDF model parameters," *Remote Sensing of Environment*, vol. 89, no. 1, pp. 63–71, Jan. 2004.

[40] (2010, Oct.) Brdf explained. [Online]. Available: http://www-modis.bu.edu/brdf/brdfexpl.html

[41] E. Vermote *et al.*, "Atmospheric correction of visible to middle-infrared EOS-MODIS data over land surfaces: background, operational algorithm and validation," *Journal of Geophysical Research-Atmosphere*, vol. 102, no. D14, pp. 17 131–17 141, Dec. 1997.

[42] (2010, Oct.) Types of orbits. [Online]. Available: http://www.esa.int/esaMI/Launchers_Home/ASEHQOI4HNC_0.html

[43] F. Danson, R. Armitage, and C. Marston, "Spatial and temporal modelling for parasite transmission studies and risk assessment," *Parasite*, vol. 15, no. 1, pp. 463–468, Aug. 2008.

[44] D. Lu, P. Mausel, E. Brondizio, and E. Moran, "Change detection techniques," *International Journal of Remote Sensing*, vol. 25, no. 12, pp. 2365–2407, June 2004.

[45] R. S. Lunetta, J. Ediriwickrema, D. M. Johnson, J. Lyon, and A. Mckerrow, "Impacts of vegetation dynamics on the identification of land-cover change in a biologically complex community in North Carolina, USA," *Remote Sensing of Environment*, vol. 82, no. 2-3, pp. 258–270, Oct. 2002.

[46] R. S. Lunetta *et al.*, "NALC/Mexico land-cover mapping results: implications for assessing landscape condition," *International Journal of Remote Sensing*, vol. 23, no. 16, pp. 3129–3148, Aug. 2002.

[47] (2010) NASA: TERRA (EOS AM-1). [Online]. Available: http://terra.nasa.gov/

[48] C. Justice *et al.*, "The moderate resolution imaging spectroradiometer (MODIS): Land remote sensing for global change research," *IEEE Transactions on Geoscience and Remote Sensing*, vol. 36, no. 4, pp. 1228–1249, July 1998.

[49] (2010) MODIS website. [Online]. Available: http://modis.gsfc.nasa.gov/about/

[50] (2011, Mar.) MODIS. [Online]. Available: http://eoweb.dlr.de:8080/short_guide/D-MODIS. html

[51] E. Vermote, N. E. Saleous, and C. Justice, "Atmospheric correction of MODIS data in the visible to middle infrared: first results," *Remote Sensing of Environment*, vol. 83, no. 1-2, p. 97 111, Nov. 2002.

[52] (2010) Terra tracks earth's vital signs. [Online]. Available: http://earthobservatory.nasa.gov/ IOTD/view.php?id=42805

[53] A. Huete *et al.*, "Overview of the radiometric and biophysical performance of the MODIS vegetation indices," *Remote Sensing of Environment*, vol. 83, no. 1-2, pp. 195–213, Nov. 2002.

[54] ——, "Vegetation index greenness global data set," *NASA Whitepaper*, 2006.

[55] C. Tucker and P. Sellers, "Satellite remote sensing of primary production," *International Journal of Remote Sensing*, vol. 7, no. 11, pp. 1395–1416, Nov. 1986.

[56] S. Lhermitte *et al.*, "Hierarchical image segmentation based on similarity of NDVI time-series," *Remote Sensing of Environment*, vol. 112, no. 2, pp. 506–512, Feb. 2008.

[57] M. Jakubauskas, D. Legates, and J. Kastens, "Crop identification using harmonic analysis of the time-series AVHRR NDVI data," *Computers and Electronics in Agriculture*, vol. 37, no. 1, pp. 127–139, Dec. 2002.

[58] R. I. N. Juarez and W. T. Liu, "FFT analysis on NDVI annual cycle and climatic regionality in northeast Brasil," *International Journal of Climatology*, vol. 21, no. 14, pp. 1803–1820, Nov. 2001.

[59] F. J. Garcia-Haroa, M. A. Gilaberta, and J. Meli, "Monitoring fire-affected areas using thematic mapper data," *International Journal of Remote Sensing*, vol. 22, no. 4, pp. 533–549, Mar. 2001.

[60] Q. Zhang *et al.*, "Urban built-up land change detection with road density and spectral information from multi-temporal Landsat TM data," *International Journal of Remote Sensing*, vol. 23, no. 15, pp. 3057–3078, Aug. 2002.

[61] T. Fung and W. Siu, "Environmental quality and its changes, an analysis using NDVI," *International Journal of Remote Sensing*, vol. 21, no. 5, pp. 1011–1024, July 2000.

[62] J. Townshend, C. Justice, C. Gurney, and J. McManus, "The impact of misregistration on change detection," *IEEE Transactions on Geoscience and Remote Sensing*, vol. 30, no. 5, pp. 1054–1060, Sept. 1992.

[63] X. Dai and S. Khorram, "The effects of image misregistration on the accuracy of remotely sensed change detection," *IEEE Transactions on Geoscience and Remote Sensing*, vol. 36, no. 5, pp. 1566–1577, Sept. 1998.

[64] D. Roy, "The impact of misregistration upon composited wide field of view satellite data and implications for change detection," *IEEE Transactions on Geoscience and Remote Sensing*, vol. 38, no. 4, pp. 2017–2032, July 2000.

[65] J. Verbesselt, R. Hyndman, A. Zeileis, and D. Culvenor, "Phenological change detection while accounting for abrupt and gradual trends in satellite image time series," *Remote Sensing of Environment*, vol. 114, no. 12, pp. 2970–2980, Dec. 2010.

[66] R. Kennedy, W. Cohen, and T. Schroeder, "Trajectory-based change detection for automated characterization of forest disturbance dynamics," *Remote Sensing of Environment*, vol. 110, no. 3, pp. 370–386, Oct. 2007.

[67] F. Schoeman *et al.*, "South african national land-cover change map," Food and Agriculture Organization of the United Nations (FAO), Tech. Rep. GW/A/2010/47, June 2010.

[68] T. Celik, "A Bayesian approach to unsupervised multiscale change detection in synthetic aperture radar images," *Signal Processing*, vol. 90, no. 5, pp. 1471–1485, May 2010.

[69] T. Celik and K. Ma, "Unsupervised change detection for satellite images using Dual-tree complex wavelet transform," *IEEE Transactions on Geoscience and Remote Sensing*, vol. 48, no. 3, pp. 1199–1210, Mar. 2010.

[70] F. Bovolo and L. Bruzzone, "A Split-based approach to unsupervised change detection in large-size multitemporal images: Application to Tsunami-damage assessment," *IEEE Transactions on Geoscience and Remote Sensing*, vol. 45, no. 6, pp. 1658–1670, June 2007.

[71] J. Deng, K. Wang, Y. Hong, and J. Qi, "Spatio-temporal dynamics and evolution of land use change and landscape pattern in response to rapid urbanization," *Landscape and Urban Planning*, vol. 92, no. 3-4, pp. 187–198, Sept. 2009.

[72] C. Jha and N. Unnia, "Digital change detection of forest conversion of a dry tropical Indian forest region," *International Journal of Remote Sensing*, vol. 15, no. 13, pp. 2543–2552, Sept. 1994.

[73] R. G. Townshend and C. O. Justice, "Spatial variability of images and the monitoring of changes in the normalized difference vegetation index," *International Journal of Remote Sensing*, vol. 16, no. 12, pp. 2187–2195, Aug. 1995.

[74] E. Lambin and A. Strahler, "Change-vector analysis in multitemporal space: A tool to detect and categorize land-cover change processes using high temporal-resolution satellite datasta," *Remote Sensing of Environment*, vol. 48, no. 2, pp. 231–244, May 1994.

[75] (2011, Jan.) Engineering Statistics Handbook. NIST/SEMATECH e-handbook of statistical methods. [Online]. Available: http://www.itl.nist.gov/div898/handbook/

[76] D. Hayes and W. Cohen, "Spatial, spectral and temporal patterns of tropical forest cover change as observed with multiple scales of optical satellite data," *Remote Sensing of Environment*, vol. 106, no. 1, pp. 1 – 16, Jan. 2007.

[77] S. Mitra, *Digital Signal Processing*, W. Stephen, Ed.   New York, NY: McGraw Hill, 2002.

[78] S. Lee and M. M. Crawford, "Multitemporal classification of image series with seasonal variability using harmonic components," in *IEEE International Geoscience and Remote Sensing Symposium*, vol. 5, Toulouse, France, July 2003, pp. 3353–3355.

[79] B. P. Salmon, J. C. Olivier, K. J. Wessels, W. Kleynhans, F. van den Bergh, and K. Steenkamp, "Unsupervised land cover change detection: Meaningful sequential time series analysis," *Selected Topics in Applied Earth Observations and Remote Sensing (IEEE Early Access)*, vol. 99, Oct. 2010.

[80] D. J. Mildrexler, M. Zhao, F. Heinsch, and S. W. Running, "A new satellite-based methodology for continental-scale disturbance detection," *Ecological Applications*, vol. 17, no. 1, pp. 235–250, Jan. 2007.

[81] C. Potter *et al.*, "Major disturbance events in terrestrial ecosystems detected using global satellite data sets," *Global Change Biology*, vol. 9, no. 7, pp. 1005–1021, July 2003.

[82] C. Justice *et al.*, "The MODIS fire products," *Remote Sensing of Environment*, vol. 83, no. 1-2, pp. 244–262, Nov. 2002.

[83] A. Strahler, "MODIS land cover product algorithm theoretical basis document (ATBD)," *Boston University, Boston, MA*, 1999. [Online]. Available: {C}enterfor{R}emote{S}ensing

[84] E. Lambin and A. Strahler, "Indicators of land-cover change for change-vector analysis in multitemporal space at coarse spatial scales," *International Journal of Remote Sensing*, vol. 15, no. 10, pp. 2099–2119, July 1994.

[85] B. Ristic, S. Arulampalam, and N. Gordon, *Beyond the Kalman filter: Particle Filters for Tracking Applications*, 1st ed.   London: Artech House, 2004.

[86] R. Kalman, "A new approach to linear filtering and prediction problems," *AMSE Journal of Basic Engineering*, vol. 82, no. 1, pp. 35–45, Mar. 1960.

[87] J. R. G. Townshend, T. E. Goff, and C. J. Tucker, "Multitemporal dimensionality of images of normalized difference vegetation index at continental scales," *IEEE Transactions on Geoscience and Remote Sensing*, vol. GE-23, no. 6, pp. 888–895, Nov. 1985.

[88] K. J. Wessels *et al.*, "Mapping regional land cover with MODIS data for biological conservation: Examples from the greater Yellowstone ecosystem, USA and Para state, Brazil," *Remote Sensing of Environment*, vol. 92, no. 1, pp. 67–83, July 2004.

[89] M. C. Hansen, R. DeFries, J. R. G. Townshend, and R. Sohlberg, "Global land cover classification at 1km spatial resolution using a classification tree approach," *International Journal of Remote Sensing*, vol. 21, no. 6-7, pp. 1331–1364, Apr. 2000.

[90] M. A. Friedl *et al.*, "Global land cover mapping from MODIS: algorithms and early results," *Remote Sensing of Environment*, vol. 83, no. 1-2, pp. 287–302, Nov. 2002.

[91] M. Hall-Beyer, "Comparison of single-year and multiyear NDVI time series principal components in cold temperate biomes," *IEEE Transactions on Geoscience and Remote Sensing*, vol. 41, no. 11, pp. 2568–2574, Nov. 2003.

[92] R. Lasaponara, "Estimating interannual variations in vegetated areas of Sardinia island using SPOT/VEGETATION NDVI temporal series," *IEEE Geoscience and Remote Sensing Letters*, vol. 3, no. 4, pp. 481–483, Oct. 2006.

[93] D. Alcaraz, J. Paruelo, and J. Cabello, "Identification of current ecosystem functional types in the Iberian peninsula," *Global Ecology and Biogeography*, vol. 15, no. 2, pp. 200–212, Mar. 2006.

[94] N. Viovy, "Automatic classification of time series (ACTS): a new clustering method for remote sensing time series," *International Journal of Remote Sensing*, vol. 21, no. 6-7, pp. 1537–1560, Apr. 2000.

[95] O. Samain, J. Roujean, and B. Geiger, "Use of a Kalman filter for the retrieval of surface BRDF coefficients with a time-evolving model based on the ECOCLIMAP land cover classification," *Remote Sensing of Environment*, vol. 112, no. 4, pp. 1337–1346, Apr. 2008.

[96] M. Chen, S. Liu, L. Tieszen, and D. Hollinger, "An improved state-parameter analysis of ecosystem models using data assimilation," *Ecological Modelling*, no. 3-4, pp. 317–326, Dec. 2008.

[97] Y. Li, J. Chen, R. Lu, P. Gong, and T. Yue, "Study on land cover change detection method based on NDVI time series datasets: Change detection indexes design," in *IEEE International Geoscience and Remote Sensing Symposium*, vol. 1-8, Seoul, South Korea, July 2005, pp. 2323–2326.

[98] D. G. Brown *et al.*, "Stochastic simulation of land-cover change using geostatistics and generalized additive models," *Photogrammetric Engineering and Remote Sensing*, vol. 68, no. 10, pp. 1051–1061, Oct. 2002.

[99] W. Kleynhans, J. C. Olivier, K. J. Wessels, B. P. Salmon, F. van den Bergh, and K. Steenkamp, "Improving land cover class separation using an extended Kalman filter on MODIS NDVI time series data," *IEEE Geoscience and Remote Sensing Letters*, vol. 7, no. 2, pp. 381–385, Apr. 2010.

[100] ——, "Detecting land cover change using an extended kalman filter on MODIS NDVI time-series data," *IEEE Geoscience and Remote Sensing Letters*, vol. 8, no. 3, pp. 507–511, May 2011.

[101] H. You, J. Garrison, G. Heckler, and D. Smajlovic, "The autocorrelation of waveforms generated from ocean-scattered GPS signals," *IEEE Geoscience and Remote Sensing Letters*, vol. 3, no. 1, pp. 78–82, Jan. 2006.

[102] D. Jupp, A. Strahler, and C. Woodcock, "Autocorrelation and regularization in digital images I. basic theory," *IEEE Transactions on Geoscience and Remote Sensing*, vol. 26, no. 4, pp. 463–473, July 1988.

[103] ——, "Autocorrelation and regularization in digital images II. simple image models," *IEEE Transactions on Geoscience and Remote Sensing*, vol. 27, no. 3, pp. 247–258, May 1989.

[104] M. Clark and T. Aide, "Virtual interpretation of Earth Web-interface tool (VIEW-IT) for collecting land-use/land-cover reference data," *Remote Sensing*, vol. 3, no. 3, pp. 601–620, Mar. 2011.

[105] M. Rosenblatt, "Remarks on some nonparametric estimates of a density function," *Annals of Mathematical Statistics*, vol. 27, no. 3, pp. 832–837, Mar. 1956.

[106] E. Parzen, "On estimation of a probability density function and mode," *Annals of Mathematical Statistics*, vol. 23, no. 3, pp. 1065–1076, Mar. 1962.

[107] B. McCusker, "Land use and cover change as an indicator of transformation on recently redistributed farms in Limpopo province, South Africa," *Human Ecology*, vol. 32, no. 1, pp. 49–75, Feb. 2004.

[108] J. Olivier, K. Wessels, and S. Araya, "Detection of land cover change using an artificial neural network within a temporal sliding window on MODIS time series data," in *Geoscience and Remote Sensing Symposium, 2008. IGARSS 2008. IEEE International*, vol. 4, 7-11 2008, pp. 1422–1424.

PUBLICATIONS EMANATING FROM THIS THESIS AND RELATED WORK

A.1 PAPERS THAT APPEARED IN THOMSON INSTITUTE FOR SCIENTIFIC INFORMATION (ISI) JOURNALS

- W. Kleynhans, J. C. Olivier, K. J. Wessels, F. van den Bergh, B. P. Salmon and K. C. Steenkamp, *Improving land-cover class separation using an extended Kalman filter on MODIS NDVI time-series data*, IEEE Geoscience and Remote Sensing Letters, vol. 7, no. 2, April 2010, pp 381-385

- W. Kleynhans, J. C. Olivier, K. J. Wessels, F. van den Bergh, B. P. Salmon and K. C. Steenkamp, *Detecting Land Cover Change Using an Extended Kalman Filter on MODIS NDVI Time Series Data* , IEEE Geoscience and Remote Sensing Letters, IEEE Geoscience and Remote Sensing Letters, vol. 8, no. 3, May 2011, pp 507-511

- B. P. Salmon, J. C. Olivier, K. J. Wessels, W. Kleynhans, F. van den Bergh and K. C. Steenkamp, *Unsupervised land-cover change detection: Meaningful Sequential Time Series Analysis*, IEEE Journal of Selected Topics in Applied Earth Observations and Remote Sensing, (Available on-line @ IEEE Early Access - doi:10.1109/JSTARS.2010.2053918)

A.2 PAPERS SUBMITTED TO THOMSON ISI JOURNALS

- B. P. Salmon, J. C. Olivier, K. J. Wessels, F. van den Bergh, W. Kleynhans and K. C. Steenkamp, *Automated land-cover change detection using MODIS satellite time series data: Introducing the temporal sliding window*, Applied Earth Observation and Geoinformation (Submitted)

A.3 PAPERS PUBLISHED IN REFEREED ACCREDITED CONFERENCE PROCEEDINGS

- W. Kleynhans, J. C. Olivier, B. P. Salmon, K. J. Wessels and F. van den Bergh, *Improving NDVI time series class separation using an extended Kalman filter*, IEEE Geoscience and Remote Sensing Symposium 2009, Cape Town, South Africa 12-17 July 2009

- W. Kleynhans, J. C. Olivier, B. P. Salmon, K. J. Wessels and F. van den Bergh, *A spatio-temporal approach to detecting land-cover change using an extended Kalman filter on MODIS time series data*, IEEE Geoscience and Remote Sensing Symposium 2010, Hawaii, USA, 25-30 July 2010

- W. Kleynhans, J. C. Olivier, B. P. Salmon, K. J. Wessels and F. van den Bergh, *A comparison of feature extraction methods within a spatio-temporal land cover change detection framework*, IEEE Geoscience and Remote Sensing Symposium 2011, Vancouver, Canada, 24-29 July 2011 (Accepted)

- B. P. Salmon, J. C. Olivier, W. Kleynhans, K. J. Wessels and F. van den Bergh, *Meta-optimization of the extended Kalman filters parameters for improved feature extraction on hypertemporal images*, IEEE Geoscience and Remote Sensing Symposium 2011, Vancouver, Canada, 24-29 July 2011 (Accepted)

- B. P. Salmon, J. C. Olivier, W. Kleynhans, K. J. Wessels and F. van den Bergh, *The quest for automated land-cover change detection using satellite time series data: meaningful high temporal time series extraction*, IEEE Geoscience and Remote Sensing Symposium 2009, Cape Town, South Africa 12-17 July 2009

- B. P. Salmon, J. C. Olivier, W. Kleynhans, K. J. Wessels and F. van den Bergh, *Automated land-cover change detection: The quest for meaningful high temporal time series extraction*, IEEE Geoscience and Remote Sensing Symposium 2010, Hawaii, USA, 25-30 July 2010

A.4 INVITED CONFERENCE PAPERS IN REFEREED ACCREDITED CONFERENCE PROCEEDINGS

- W. Kleynhans, J. C. Olivier, B. P. Salmon, K. J. Wessels and F. van den Bergh, *An autocorrelation analysis approach to detecting land cover change using hyper-temporal time-series data*, IEEE Geoscience and Remote Sensing Symposium 2011, Vancouver, Canada, 24-29 July 2011 (Invited Session: Change Detection and Multitemporal Image Analysis)

LIST OF TABLES

LIST OF FIGURES